UNIVERSITY OF CALIFORNIA
RIVERSIDE

Mobile Positioning and Mapping With Range Sensor Aided Differential GPS/Inertial Navigation System

A Dissertation submitted in partial satisfaction
of the requirements for the degree of

Doctor of Philosophy

in

Electrical Engineering

by

Haiyu Zhang

December 2014

Dissertation Committee:

Dr. Matthew J. Barth, Co-Chairperson
Dr. Jay A. Farrell, Co-Chairperson
Dr. Gang Chen

The Dissertation of Haiyu Zhang is approved:

Committee Co-Chairperson

Committee Co-Chairperson

University of California, Riverside

Acknowledgements

First, I would like to express my sincere gratitude to my co-advisor Professor Matthew J. Barth for his continuous support and contribution to my study and research. His professional perspective, patience, motivation, encouragement have given me strength throughout my entire Ph.D. program. I would also like to acknowledge my co-advisor, Professor Jay A. Farrell for his academic suggestions when I was stuck by the research problems. I would also give my thanks to Professor Gang Chen whose suggestions help a lot in my research. Without all their help, I would not have been able to finish my program.

I am very grateful to many past and current members in Professor Barth's and Professor Farrell's groups: Dr. Lili Huang, Dr. Anning Chen, Dr. Anh Vu, Dr. Qichi Yang, Dr. Haitao Xia, Qiu Jin and Ji Luo. When I started my research, it was them who showed me how a Ph.D. student handled their research problems. To Anh Vu, your expertise in the research area, and coding has all been my role model. I would also never forget the moment Qichi brainstorming with me. The easy attitude towards difficult research problems always encourages me. I would like to thank the staff in the TSR group, Michael Todd and Daniel Sandez for their assistance on my experiments.

I would also like to thank all my friends in WCH 369, Dongfang Zheng, Yiming Chen, Mingyang Li and Sheng Zhao. The whole five years of time together with all of you will always be a precious memory of my life. We together have spent time discussing

difficult problems from the coursework, preparing exams, help each other with research problems and encourage each other. Without all you guys, my Ph.D. life would be boring.

I would also like to show my gratitude to all my friends at UCR, Dr. Bo Zhao, Dr. Fang Jia, Dr. Yang Li, Dr. Wenting Hou, Dr. Yuanqi Tao and Chen Yang for their encouragements, and all the happiness we shared.

Most importantly, none of this would have been possible without the love and patience of my family. I would like to express my heart-felt gratitude to my parents Yuliang Zhang and Hong Yu, and my girlfriend Jiezhen Tian for all the support they gave me.

Finally, I would like to take this opportunity to thank all persons who have ever helped me before.

To my parents and my girlfriend, for all their love.

ABSTRACT OF THE DISSERTATION

Mobile Positioning and Mapping With
Range Sensor Aided Differential GPS/Inertial Navigation System

by

Haiyu Zhang

Doctor of Philosophy, Graduate Program in Electrical Engineering
University of California, Riverside, December 2014
Dr. Matthew J. Barth, Co-Chairperson
Dr. Jay A. Farrell, Co-Chairperson

Traditional positioning solely using GPS has been shown to be inadequate for more advanced Intelligent Transportation System (ITS) applications. Accurate and reliable mapping also requires a highly accurate and reliable positioning system. Integration of GPS and an Inertial Measurement Unit (IMU) is a promising method in terms of improving accuracy. When GPS signal are unavailable to reset IMU errors, range sensors, e.g., RADAR and LiDAR which can measure distance and angle to road side landmarks by actively emitting power and measuring reflected signals, serve as a good complement to guarantee accuracy. In addition, the advancement in 3D LiDAR technology makes the mobile mapping system very handy because it does not require lane closures or time-consuming human surveying, thereby saving both time and money.

In this dissertation, a novel automotive RADAR-aided Differential GPS/INS system is presented. The RADAR measurement model is analyzed, and proper types of landmarks are investigated and verified. The residue and corresponding error models are also analyzed. Two separate mathematical models are proposed for integration with

GPS/INS in an Extended Kalman Filter (EKF) architecture. Experiments in a controlled environment are described and the results illustrate significant improvement of positioning accuracy when the RADAR detects landmarks, data association is successful, and RADAR measurements are used to update the EKF estimates.

In the second part of the dissertation, a 3D LiDAR-based Mobile Mapping system is presented. The overall system architecture on both hardware and software are demonstrated. An intersection stop bar extraction algorithm based on image processing is then described in detail with intermediate results demonstrated as images. The results of the algorithm are the accurate position of the endpoints of each stop bar in a global coordinate frame.

Contents

List Of Figures

List Of Tables

Chapter 1 Introduction

In the past decade, an increasing number of driving assistance technologies have stepped out of theoretical articles, and have become real products. With the ultimate goal of releasing human from tedious driving experiences, various intermediate driving assistance systems have been developed, and fully automated vehicles are soon becoming a reality. At the macro level, various intelligent transportation areas have been explored to optimize traffic as a whole. Within all these systems, *vehicle positioning* plays an indispensable and fundamental role.

Thanks to the first successful Global Navigation Satellite System (GNSS) -- Global Positioning System (GPS), people tossed away paper maps and are enjoying guidance from their personal GPS navigation devices. However, GPS alone provides limited accuracy (~3m level) in open sky conditions. Such accuracy is adequate to simply guide driving at a macro level (i.e., which route to take), but cannot meet the ever-increasing requirements of new advanced ITS applications. In general, there are several aspects of the positioning systems that are of vital importance:

- Accuracy
- Availability – The ability to operate in all driving conditions
- Cost

An affordable, accurate, continuously available and reliable positioning system will have significant impact on *roadway safety*, through safety related driving assistant

systems such as lane-departure warning system, early collision warning system, collision avoidance system, and curve over-speed warning system. With the help of connected vehicle technology, a better positioning system will also have positive impact on mobility, through applications such as traffic signal phase and timing (SPaT), advanced navigation systems, congestion warning systems, speed recommendation systems, etc. Lastly, energy consumption and emissions could also be improved for individual vehicles and as an overall transportation system primarily through the mobility applications.

Currently, vehicle navigation systems typically rely on GNSS alone. To achieve the required levels of availability and reliability necessary for advanced applications, the positioning solution will soon be achieved by integrating GNSS receivers with high-rate sensors such as Inertial Measurement Unit (IMU) and wheel encoders (or brake pulses). However, this method still could not solve the availability problem because when GNSS signals are unavailable, the accumulation of high rate sensor error through the numeric integration process would make accuracy unacceptable in a short period of time (minutes) [3]. This dissertation provides a survey of popular aiding sensors and signals to help solve this problem, and then focuses on one promising sensor – automotive RADAR, demonstrating a method to integrate RADAR with a GPS/IMU system. Another vital component to a positioning system is a mobile mapping system and the mathematics to support it; this is also be described in detail.

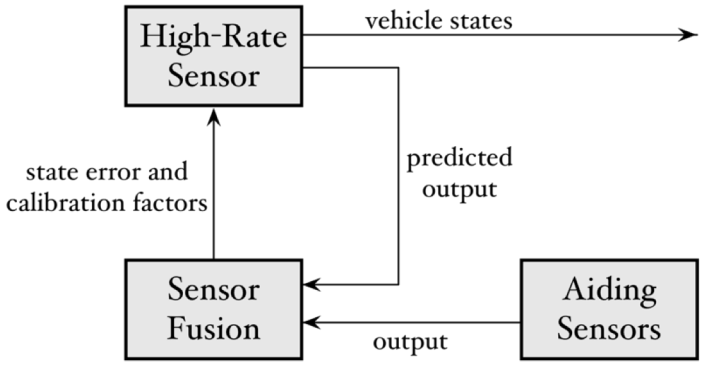

Figure 1.1 Aided navigation scheme [3]

1.1 Problem Statement

1.1.1 Vehicle Localization using RADAR-Aided GPS/INS

The major focus of this research is to design an affordable, accurate continuously available vehicle positioning method. Even though accuracy down to centimeter level can be achieved with Carrier-Phase Differential GPS [4], it is hard to guarantee this accuracy in all situations. According to [5], positioning accuracy has three levels: road level, lane level and within-lane level (or where-in-lane level). Road-level accuracy is adequate to determine which road the vehicle is on. Lane-level accuracy needs to be able to identify which lane the vehicle is on, which requires the error is smaller than 0.5m. Within-lane-level accuracy requires the positioning error be smaller than 0.1m. As such, this research focuses specifically on "where-in-lane" accuracy vehicle positioning systems.

The ability to be continuously available requires that the positioning system has some high-rate sensor that could provide continuous measurements without relying on external signals which will be intermittently available. Also, most target applications require the vehicle state estimate at a high-rate and high-bandwidth, much higher that is

achievable by an aiding sensors alone (e.g., GNSS, vision, etc.). Finally, these systems require state information (i.e., velocity, acceleration, attitude, angular rate) that could only be computed from aiding sensors by differentiation, which is a problematic numeric process. Therefore, future vehicle positioning systems will require that the measurement from a high-rate sensor be integrated through the vehicle kinematic model to generate a vehicle state prediction, while the aiding sensors that relying on external reference signals or reference objects provide low-rate measurement to correct the state prediction. The most common high-rate systems are Inertial Navigation Systems (INS) and wheel-encoder-based dead-reckoning systems [6]. GPS/GNSS represents the most common category of aiding sensors. These aiding systems rely on external electromagnetic signals to some known reference (GPS satellites in this case), and output some measurements that are related to the spatial relationship to the references. The integration of GPS with INS has been well established, as described in [6].

Unfortunately, a GPS/INS system sometimes has limited availability in some areas, such as dense urban areas (e.g., an “urban canyon”). In such areas, the high-rate sensor by itself will only keep acceptable accuracy for short periods of time. A typical MEMS IMU can maintain 20cm of accuracy for up to 10 seconds without aiding sensors [3]. Meanwhile, there are abundant existing natural and artificial landmarks and other locally available electromagnetic signals especially in dense urban areas. Many aiding sensors have been investigated such as video cameras, RADAR, LiDAR, Cellular Signal, WiFi, etc. [3]. A brief comparison of different aiding sensors/signals is listed in the following table.

Table 1-1 Comparison of popular Aiding Sensors

Aiding Sensor	Type	Infrastructure Requirements
GPS, Differential GPS, Carrier-Phase DGPS	GNSS	Satellites, Ground base station
GLONASS, Galileo, BeiDou	GNSS	Satellites, Ground base station
Computer Vision	Feature Based	Existing roadway feature
LiDAR	Feature Based	Existing roadway feature
RADAR	Feature Based	Existing roadway feature
Pseudolite	Ground based Radio Signal	Pseudolite transmitters
Cell Phone	Ground based Radio Signal	Existing cellular station
Packet Radio (WiFi, DSRC)	Ground based Radio Signal	Existing Access Points
Other Radio Carrier Signal (AM/FM Radio, TV)	Ground based Radio Signal	Existing Transmitter Infrastructure

A detailed review of different sensors and their method for aiding navigation is in Chapter 2. In this research, we focus on automotive RADAR, since the use of affordable automotive RADAR with GPS/INS has not yet been well developed. This research tries to solve the following aspects of the problems to integrate automotive RADAR with the GSP/INS system:

- **Feasibility**: Are RADAR measurement suitable for integration with GPS/INS?
- **RADAR Feature Selection**: What feature/landmarks are suitable for RADAR in the sense of cost, availability and performance?
- **Feature measurement model**: How can we integrate RADAR measurement with GPS/INS mathematically? Specifically, how can the residual be formed from available information in real-time?

- **Verification of the system performance**: In a real-world experience, does the system performance meet our expectation?

1.1.2 Roadway Feature Mapping

One essential part of making the aforementioned positioning system possible is a roadway spatial information database, or in general, a digital map. Roadway features for aiding sensors are part of this database. Examples of such roadway features include and are not restricted to stoplights, lane-markers, curbstones, light poles, building facets close to the road, etc. The database stores the spatial information of the roadway features as well as other properties according to the needs of different sensors. However, the use of the roadway spatial information database is not restricted to storing features for aiding sensors. Many ITS applications need such a database. For example, a vehicle speed recommendation system would not only need the position of the vehicle, it also need to know the roadway properties such as road grade and the shape of the current road. In short, the database provides a reference to the aided-positioning system and other ITS applications.

In a broad sense, the term mapping refers to the procedure of building up this roadway spatial information database. Traditionally, people use aerial photogrammetry or terrestrial surveying to build up maps. There are some shortcomings for these methods that render them unsuitable and time-consuming for extensive feature mapping. Aerial photogrammetry could hardly handle the surveying of 3D objects, which are a major part of the roadmap spatial information database, and are often

used as features for aiding sensors [7]. Further, it is also typically costly and time consuming. Manual terrestrial surveying could handle a variety of objects of interest, but it also takes much time and manpower so that it is not well suited for the fast-changing environments [8]. On the other hand, *automated mobile mapping* is becoming an increasingly popular method.

A mobile mapping system typically consists of a moving platform, a navigation system and mapping sensors. The moving platform could be a land vehicle, marine vessel, or an aircraft. In this document, a land vehicle is chosen as the moving platform. The navigation system is the Carrier-Phase DGPS/INS system described in Chapter 4, providing accurate position and orientation information of the vehicle during the entire surveying period. The mapping sensor in this particular research is the Velodyne 3D LiDAR, which provides 3D point clouds in an egocentric coordinate frames. This research focuses mainly on the processing of the LiDAR point cloud to extract some roadway features of interests, and result in the spatial parameters of these suitable features.

1.2 Key Contributions

There are several key contributions of this research.

- A new automotive RADAR aided DGPS/INS system has been developed. It is based on existing DGPS/INS positioning systems, with the key contribution being the integration of RADAR into the system. Specifically, 1) the preferable

mounting position with respect to GPS and IMU has been tested and determined; 2) the RADAR measurement has been analyzed on selected landmark features and the measurement model for two different feature types has been developed for integration with GPS/INS using an Extended Kalman Filter (EKF); and 3) the performance of the system has been tested to prove the correctness and effectiveness of the developed model.

- In addition, a novel roadway feature extraction algorithm has been developed. The roadway spatial data are collected using the DGPS/INS system that includes an integrated Velodyne 3D LiDAR. The algorithm processes the LiDAR point cloud data, converts all point coordinates to a uniform global coordinates, and then extracts two selected road features of interest: namely, intersection stop bars and road curbs.

1.3 Dissertation Organization

This dissertation is organized as follows.

Chapter 2 describes the background of the two major projects in this dissertation, providing a review of related work in aided navigation and mobile mapping, identifies the shortcomings of the current methods, and motivates the selection of the methods in this research.

Chapter 3 demonstrates the system setup, on both hardware and software, and introduces the two major sensors used in this dissertation – RADAR and Velodyne LiDAR.

Chapter 4 describes the proposed method to integrate RADAR and DGPS/INS system for lane-level navigation, including features selection, mathematical models and field test results and analysis.

Chapter 5 describes the methods to process point cloud data collected the 3D LiDAR based mobile mapping system, and the algorithms to reliably extract roadway features.

Chapter 6 provides a summary of the work in this dissertation, and provides directions to future work.

Chapter 2 Background and Related Work

2.1 Aided Positioning System

As described in Chapter 1, aided positioning systems are a promising way to providing affordable, accurate and continuously available vehicle position. In the system demonstration in Figure 1.1, the aided positioning system has three major components -- the high-rate sensor, the aiding sensor and the data fusion algorithm. For ground vehicle positioning systems, the most popular high-rate sensors are either wheel-encoders or IMUs. The output of either a wheel-encoder or IMU reflects the ego motion. With the integration of the high-rate sensor output through a vehicle kinematic model, the vehicle position and attitude can be estimated, but any sensor noise and bias would degrade the accuracy with time. The most widely applied aiding sensor for outdoor vehicle positioning systems is GPS and advanced GPS (DGPS and CP-DGPS). Both GPS integrated with wheel encoders and IMUs have been thoroughly investigated, and some examples can be seen in [4, 6, 9-12]. Further, a large amount of effort has been put into data fusion algorithms. The most popular and simplest to implement algorithm is the Extended Kalman Filter (EKF) and its derivatives [4, 13-15]. Other popular algorithms include Unscented Kalman Filter (UKF) [13, 15, 16] and particle filters [17, 18]. The comparison of these major algorithms can be found in [19]. It is not a major concern of this research to compare the performance of different filters, so the EKF was selected as the data fusion algorithm in the aided positioning system in Chapter 4 due to its

simplicity and good performance. Further, raw GPS measurements (pseudo-range, Doppler, and carrier-phase) are integrated with the GPS/INS directly in a tightly coupled architecture, because it has better robustness and overall accuracy over a loosely coupled architecture. The reason is that in areas where GPS reception could be marginal, the loosely coupled architecture may not receive a minimum of four satellites to solve position and velocity and thus could not be used to correct INS drifts [20].

Apart from GPS, many sensors have been investigated as aiding sensor for a GPS/INS positioning systems. The following sections present an overview of different aiding sensors that are categorized based on the physical signal and the measurement methods. What is worth noticing is that a single sensor usually falls into a single physical signal category, but may use multiple measurement methods.

2.1.1 Categorization According to Physical Signal

2.1.1.1 Global Navigation Satellite Systems

GNSS is the most mature and accurate method to determine a vehicle's position in a global coordinate frame [21]. It relies on a constellation of satellites that orbit the earth. The satellites broadcast coded radio signals to the earth, and the receiver measures the Pseudo-Random Noise Sequence from the satellite to determine the propagation time. In advanced GNSS systems (Differential GNSS and Carrier Phase GNSS), a base correction station sends correction messages to the receiver to compensate common-mode errors. With GNSS alone, the system needs at least four satellite signals to solve for the 3-dimensional receiver coordinates and the receiver clock offset. In this category, the

physical signal is the radio frequency coded signal from which various observables are extracted, and the reference stations are the orbiting satellites.

2.1.1.2 Ground-Based Radio Signal Positioning

Similar to GNSS, ground-based systems also broadcast radio frequency signals. The radio signals may be specified for positioning purposes, such as pseudolite [22]. A pseudolite emits a signal that mimics the GNSS satellite but its transceiver sits on the ground to assist positioning in areas where GNSS signals are unavailable. Radio signals that majorly serve other purposes (i.e. Signals of Opportunity) could also be utilized for positioning such as cellular signal [23, 24], digital TV [25, 26], AM/FM Radio [27-29], WiFi [30, 31] and Dedicated Short Range Communications (DSRC) [32]. The measurement methods and related work of the sensors are discussed in section 2.1.2.

2.1.1.3 Feature-Based Positioning

In contrast to radio signal based positioning, feature-based sensors rely on local natural or artificial structures (e.g. road infrastructure, roadside buildings, and other vehicles). The sensor collects the emitted or reflected spatial wavelength in the visible and/or non-visible spectrum, and measures the spatial relationship (i.e. distance, angle) to the source object. Active feature-based sensors emit electromagnetic signals, and collect the reflected signal to take measurements. RADAR, LiDAR, Sonar and some active cameras are good representatives. Passive feature-based sensors do not emit power actively, but collect either reflected spectrum on the structure coming from other sources, or the spectrum emitted from the signal. The light signal that a normal camera can receive

comes from either the sunlight, or other illumination sources (e.g. road lights, vehicle head lights). Infrared camera could generate images based on the emitted infrared from objects.

The feature-based sensors are naturally good complements to GPS/INS positioning systems. These egocentric sensors do not rely on external reference stations thus require minimum infrastructure cost, and the features they rely on are mainly local features which do not suffer from signal blockage. In GNSS occluded areas, feature-based sensors could play an important role to guarantee positioning accuracy. In these positioning systems, the feature positions need to be known a priori. The sensor data are grouped, filtered, and features are extracted based on corresponding models, and then associated with the known features, and the residual is then integrated with the INS.

The most popular feature-based sensors are cameras, RADAR and LiDAR.

Cameras provide ample information about the feature it detects such as shape, angle, color, texture, etc. Many computer vision algorithms are available to extract features from single or a series of images. Further, the cost of a camera system is considerably lower in comparison to RADAR and LiDAR. As a result, camera-based positioning/localization systems have gained a lot of attention not only in the vehicular positioning area, but also in robotics [33]. Due to the ample information cameras could provide, it is possible to use the changes between consecutive camera images to estimate the position and orientation change of a robot [34] which is called visual odometry. In such cases, the camera does not focus on a single specific features, but processes clusters of different features together. Similarly, the Visual Inertial Odometry (VIO) combines

camera streams with inertial sensors to estimate motion in unknown environment [35]. For vehicle positioning, the existing natural or artificial features that are significant to extract from the images are most suitable, for example, LED lights [36] and stop lights [37].

LiDAR measures the distance by illuminating the targets with laser light and then analyze the reflected signal. LiDAR has a very small beamwidth thanks to the characteristics of lasers, and thus provide a good distance measurement accuracy and angle discrimination. Before automotive industry, LiDAR was popularly used as a sensor to build high accuracy maps. Further, LiDAR is also widely used in Robotics for absolute positioning or Simultaneous Localization and Mapping (SLAM). The features commonly used in a positioning system by a 2D LiDAR are created by the intersection of LiDAR scanning plane with common shapes, such as points (e.g. corners), arcs (e.g. cylinder trees or poles), lines (e.g. plain walls or side of buildings). Popular 2D LiDARs use a rotating mirror to accomplish the scanning, and the angular resolution could reach 0.2º (e.g., the Sick LMS500 LiDAR [38]) thus preserving accurate shape information of the targets. As an example, a straight line from the intersection of LiDAR plane with building face could be used as a feature to aid positioning in [39]. Aside from the modeled features, the raw detections in each cycle as a group of point clouds could form patterns and be matched with known 3D map of the world to calculate absolute position or integrate with INS [40]. This method is especially useful for 3D LiDAR because each scan forms a 3D cloud point with plenty of information to carry out map matching.

The details of the RADAR sensor and related work are discussed in Section 2.2.

2.1.2 Categorization According to Measurement Method

2.1.2.1 Proximity Based

Among all measurement methods, the proximity based approach is the simplest yet coarsest. It is mostly applied with ground based radio signal positioning. The signal transmitted from the service station could only serve limited range, so when the receiver obtains signals from the stations, its location is registered as the closest station location, and the error could be as large as the station's serving radius. The accuracy could be

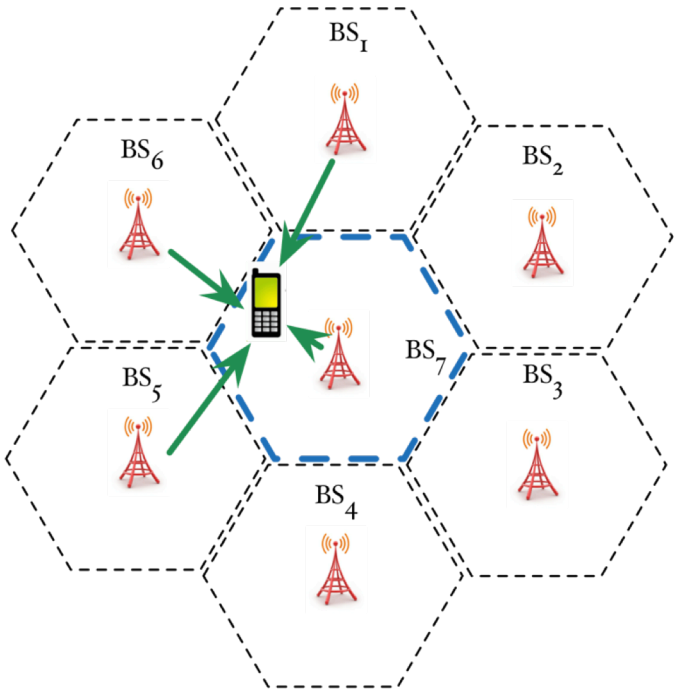

Figure 2.1 Cell-ID based positioning method. For the simplest method, the cell phone will use the coordinate of Base Station 7 (BS_7) as its coordinates, and its error radius is the radius of BS_7's cell (the center cell in blue color). The position of the cell phone could also be the centroid of BS_1 BS_5 BS_6 BS_7.

improved when signals from multiple stations are received, in which case the receiver position could be estimated as the centroid of the transmitting stations [41].

In a grid of transmitters, the accuracy is bound by the corresponding grid size. Increasing the spatial density of the transmitter grid could improve the accuracy. However the cost of the transmitter and of deployment will increase dramatically. In certain scenarios where the single transmitter is inexpensive such as a RFID transponder, and the working area is limited (e.g. in limited road areas), this method could be a simple feasible way [42]. Another example of the proximity based measurements is the coarse positioning using Cell-ID in cellular networks [43].

2.1.2.2 Signal Travel Time Based

The idea behind travel time based approaches is simple. The distance between the positioning device and the reference station can be calculated by multiplying propagation time t_{tr} with carrier signal velocity v_c in the propagation medium.

$$d_{tr} = t_{tr} v_c$$

The resolution and accuracy of the propagation time measurement decides the ranging accuracy, and then decide the final positioning accuracy. Essentially, both LiDAR and RADAR use the round-trip travel time to calculate distances. In the tightly-coupled aided positioning architecture, the raw distance measurements to reference stations (either transmitter antenna or signal reflector) are used. In a loosely-coupled architecture, the position is solved by the sensor alone. To solve for receiver position, multiple direct or indirect distance measurements could be used. The corresponding

positioning algorithms are Time of Arrival (ToA) and Time Difference of Arrival (TDoA).

Time Of Arrival (TOA) algorithm utilizes direct distance measurement between the signal transmitter and positioning device. It requires that the transmitter and receiver have synchronized clocks so the signal travel time can be simply calculated as the time difference between transmission and receiving. GPS pseudo-range measurement is essentially a TOA measurement. To solve 3D position with TOA measurements alone or in a loosely-coupled architecture, at least three TOA measurements from different reference transmitters are required given all transmitters and receivers have synchronized clocks. Each measurement defines a sphere centered at the transmitter location and whose radius is the measured distance. In an ideal condition, three spheres would intersect on a

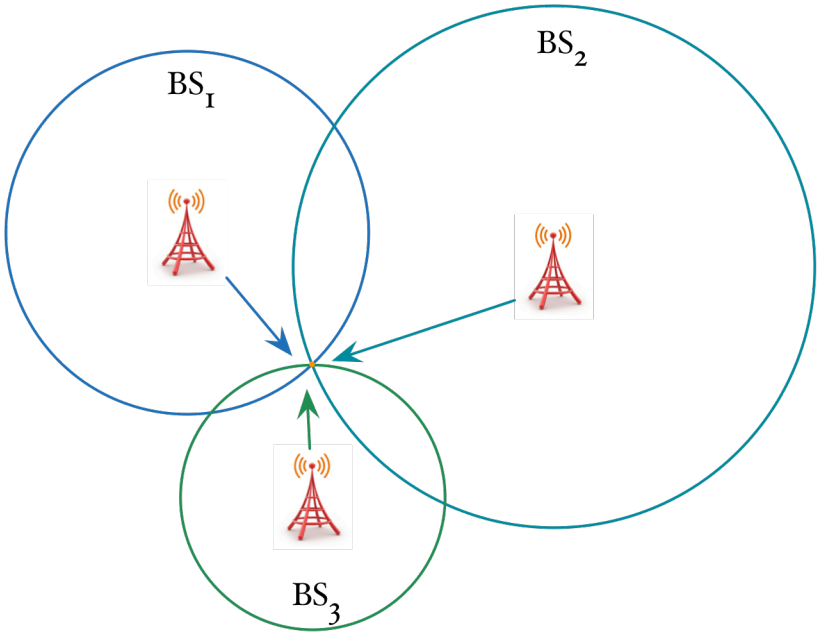

Figure 2.2 TOA based positioning (Triangulation) method. Each TOA measurement forms a sphere (as the circle in the figure), and the intersection is the solution.

single point, and that is the receiver location (Figure 2.2). GPS, WiFi based positioning [44] and custom radio positioning devices (Cricket [45], Active Bat [46], Locata [47]) are examples that use TOA method.

Time Difference Of Arrival (TDOA) approach calculates the propagation time difference between the positioning device and two reference stations or between two reference stations and the device. This method requires synchronized clocks in all reference stations but not necessarily in the positioning device. The time difference measurement could be carried out at the base station side or at the positioning device side. The time difference can be converted to travel distance differences, so each TDOA measurements define a hyperboloid in 3D space, and position could be solved as the

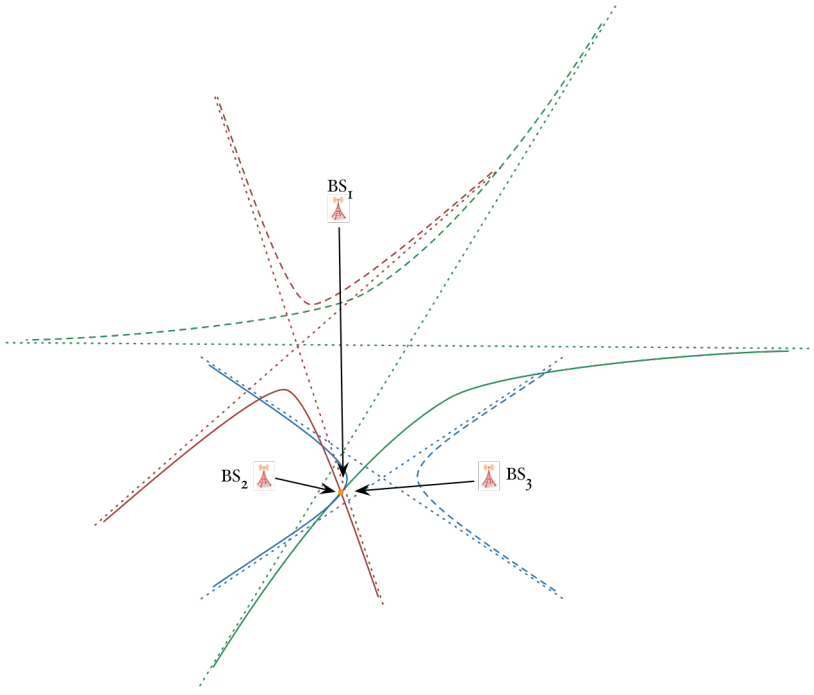

Figure 2.3 TDOA method. Each TDOA measurement forms a hyperboloid (as a hyperbola in the figure) and the intersection is the solution.

intersection of a triple set of TDOA measurement hyperboloids (Figure 2.3). Again, for a tightly-coupled architecture, the raw TDOA measurement is integrated separately. Examples of this technology could be WiFi-based positioning [48], cellular networks [49], signal of opportunity [50], AM Radio [51], and Digital TV [52].

2.1.2.3 Angle Based

The angle-based approach measures the direction of the signal with respect to some egocentric coordinate frame. For example, some RADAR sensors (e.g. Delphi ESR RADAR) uses an antenna array to measure the direction of the reflected RADAR wave. Directional antenna could also take similar Angle Of Arrival (AOA) measurements. A typical camera can be used to take two separate (horizontal and vertical) angle measurements on every object that is captured on its optical sensor. LiDAR and RADAR also provide angle measurements besides distance measurements. The position of the device can be calculated with at least two AOA measurements. Radio signal based AOA positioning does not require complicated clock synchronizations, but its positioning accuracy is limited by the angle measurement accuracy, and at far distance, even small angle measurement error could cause significant positioning error. In addition, multipath propagation of the radio signal also largely affects angle measurement accuracy. In practice, hybrid systems are more feasible, and AOA measurements are usually used as an assisted measurement to TOA or TDOA systems [53-55].

2.1.2.4 Signal Strength Based Methods

During propagation in the air, radio signals strength is affect by several factors, including propagation distance, atmosphere conditions, signal frequency, terrain etc. With known emitting power and measured received signal strength, the propagation distance can be estimated with a signal attenuation model. However, the model is complicated due to large number of factors and inaccurate due to the variation of those factors, which result in inaccurate distance estimate based on the model. Another major positioning method using signal strength is *fingerprinting*. It is an empirical approach, which does not rely on distance measurement from signal attenuation model, but instead depend on a *signal strength map*. In an environment with abundant signal sources, the signal strength of the signal from different sources varies with locations. So the first stage of fingerprinting based positioning is calibration, which means building up the connection between received signal strengths and locations. The fingerprinting approach is especially attractive for indoor positioning, because the environment is limited in size, and there are usually abundant signal sources (e.g. WiFi, cellular, radio). Another major advantage is that fingerprinting does not need any modification to the infrastructure, which is very important for WiFi based system in which TOA/TDOA measurements need significant hardware changes. The positioning accuracy using fingerprinting is greatly improved compared to signal strength – distance based positioning [56].

Table 2-1 Comparison of Aiding Sensor Measurement Methods

Aiding Sensor	Measurement Method
GNSS	TOA
Pseudolite	TOA
Camera	AOA
Stereo Camera/TOF camera	TOA
RADAR	TOA, AOA
LiDAR	TOA, AOA
Cellular	TOA, TDOA, AOA, Fingerprinting
WiFi	TOA, Fingerprinting, RSSI
DSRC	TOA
Radio, DTV	TOA, TDOA, Fingerprinting

2.2 Review on RADAR Related Work

RADAR as a detection and ranging sensor has been under development ever since its emergence in early 20th century [57]. Various types of RADAR have been developed. Target tracking is the RADAR's basic objective, in which the knowledge of targets' distance, bearing, speed etc. is provided. For example, in military applications, RADARs have been widely used to detect and track targets such as missiles, airplane sand vessels. In addition, RADAR is also used to locate precipitation when observing RADAR echos of clouds. Another branch of RADAR – Synthetic Aperture RADAR (SAR) could provide detailed terrain images when mounted on aircraft that fly above the terrain, and thus is widely used for remote sensing and mapping of the surface of both the earth and other planets [58].

In addition to object tracking, RADAR could also be used to aid navigation. For example, RADAR altimeters are widely equipped in airplanes for take-off/landing navigation support [59]. RADARs have also been customized to different application scenarios. For example, Synthetic Aperture RADAR (SAR) images could be matched with known terrain map to aid inertial measurement based aircraft navigation [60, 61]. RADAR's measurements to known landmarks makes it a good complement to inertial navigation solutions in various applications, such as mining machine navigation [62], train positioning [63], and indoor navigation [64, 65].

In the past few decades, advances in digital electronics and antenna design have made compact yet capable automotive RADAR possible. Such compact automotive RADAR is still capable to take range, range rate and angle measurement up to a hundred meters which is necessary for many advanced driver assistant and safety applications. Nowadays, automotive RADAR sensors have been equipped in a large number of vehicles ranging from mid-class to luxury cars. The most popular application for existing automotive RADAR application is Adaptive Cruise Control (ACC) [66], in which, relative position/velocity information measured by RADAR is used to keep a safety distance. Further, low cost RADAR units are also installed around vehicles to provide information about the surrounding environment, so that drivers could receive warnings on potential accidents. More specifically, examples on automotive RADAR applications include Adaptive Cruise Control, Pre-Crash Control, Blind Spot Detection, Lane Departure Warning, Stop and Go Control, and parallel parking. [67].

In comparison with other popular aiding sensors like cameras and LiDAR, RADAR has several advantages due to its special radio frequency. Passive sensors such as cameras rely highly on the illumination condition of the environment, which makes it unable to work under direct sunlight, or at night. The characteristics of laser make it possible to work regardless of environmental illumination, but still suffer from obstacles like dust, rain, snow or fog that often happen in outdoor environments [68]. In comparison, the performance of RADAR sensor is significantly less affected by these conditions, which makes it very important complement for outdoor positioning applications [69]. Further, compared with LiDAR, the power consumption of RADAR is also smaller. In addition, due to mass production and application of automotive RADAR, the price is more affordable for civilian uses.

Since the beginning of World War II, navigation systems containing RADAR have been extensively used. There are mainly two categories of RADAR sensors involved in positioning and navigation systems depending on the form of output. And each has a set of methods to aid navigation.

2.2.1 Imaging RADAR

Imaging RADAR outputs images of the detection area, which is similar to a camera. There are two major branches of imaging RADAR, SAR RADAR and Frequency Modulation Continuous Wave (FMCW) Imaging RADAR. The theory behind SAR RADAR is beyond the scope of this document and could be found in textbooks (e.g. [70]). SAR RADAR is usually mounted on an airborne platform and high-resolution terrain images can be generated while the carrier flies over. Another class of imaging

RADAR is FMCW imaging RADAR. This type of RADAR is mostly seen in maritime applications.

In essence, the imaging RADAR outputs are very similar to camera images, such that camera based localization algorithms in the Robotics field can be used for reference. Based on how RADAR images are processed to aid localization, the positioning systems can be categorized as follows.

- **Ego-motion based integration**: Sensor position and attitude change based methods use RADAR image to estimate the change of sensor position and attitude by computing changes in consecutive RADAR images. Landmarks or other significant RADAR features are detected, associated among consecutive RADAR images, and then the amount of changes in image coordinates is converted to sensor pose changes. If sensor position is purely estimated based on this method, it is called RADAR Odometry since it comes from Visual Odometry [71]. RADAR image distortion from rotating RADAR sensor on a high-speed carrier platform can also be used to estimate platform velocity and movement. The result could also be used as RADAR Odometry [72]. Fourier-Mellin transform is used in [73] to estimate ego-motion between images without selecting features. Besides, the sensor movement between consecutive images could also be used as an external sensor observation in an aided positioning architecture. For example, in [74], InSAR system calculates the consecutive SAR images on the ground, analyze the land topography, and estimate air-vehicle motion during consecutive images, and the motion estimation is integrated with INS.

- **Absolute position based integration**: Another way of utilizing RADAR Image is by extracting landmarks from image and associate with known surveyed landmarks or simply matching the RADAR Image with known ground map, and the position and attitude residues are used to determine sensor position. In SAR images, the features could be prominent objects univocally marks the land, or simply a small part of the SAR images [60]. This method requires a database or a map that is built a priori. This type of SAR sensor output can be integrated with INS [61], or INS/GPS [75] using the integration algorithms mentioned in section 2.1 to achieve better positioning accuracy. The existing such systems focus mainly on airborne SAR RADAR because the RADAR image view-point is mainly single birds-eye view and is easy for comparing with database image maps. The complicated ground vehicle environment poses bigger challenges for this approach.

2.2.2 Feature Positioning RADAR

Besides imaging RADAR, another type of RADAR output the relative position measurement to the targets with detectable RADAR cross-section (effective reflective area). The measurements usually include the range, range rate, angle, reflectivity etc. These measurements are the combination of TOA, AOA, and signal strength measurements. The measurement and corresponding errors are modeled and integrated with other encoder or IMU as a positioning system. Similar RADAR measurements are also used in SLAM [76, 77]. Both natural features [78] and artificial features (RADAR reflectors [15, 79], indoor structures) are common reference targets. In the existing

proposed systems, 2D vehicle kinematic model with EKF are common to integrate with wheel encoder, steering angle and/or gyro. The 2D world assumption is adequate where the operation environment is limited and the surface is flat. However in practice, the fact that outdoor vehicles usually operate on large areas that invalidates the 2D assumption. In Chapter 4, a low cost ACC RADAR aided GPS/INS positioning in 3D is proposed to overcome the problems.

2.3 Review on Road Feature Surveying with Mobile Mapping Systems

2.3.1 Mobile Mapping Systems

Road Feature Surveying used to be carried out by remote sensing images, such as camera or SAR images from satellites or aircraft, or by human surveying. With the advances in GNSS based positioning systems, mobile mapping systems (MMSs) have emerged and gained a lot of attention. One of the first mobile mapping systems by Ohio State University consists of a code GPS receiver integrated wheel encoder and gyro as navigation component, and stereo camera as mapping sensor [80]. Back then, the mapping accuracy is restricted by both a geo-referencing component and the mapping sensor accuracy. In the past decade, both have had significant improvements. The use of Carrier-Phase Differential GPS and a high-precision IMU results in centimeter-level accuracy and is common in many contemporary mobile mapping systems [7]. Meanwhile, mapping sensors have also gained significant advancement. Video cameras with much higher resolution have become popular and affordable, and LiDAR has become compact and cost effective enough to be widely applied in MMSs.

According to the imaging unit in use, MMSs can be characterized as camera based systems (e.g. GPSVision[81], VISAT™[82], KiSS™[83] and GI-EYE™[84]) and LiDAR based systems. The MMS using LiDAR as the main mapping sensor is the most recent development. The characteristic of laser used in LiDAR as range measurement carrier results in LiDAR capability of providing more data points with exceptional accuracy over traditional data capture methods [7]. Commercial systems have emerged since 2005, such as SITECO Road Scanner [85], TOPCON IP-S2 [86], TRIMBLE Mx8 [87], etc. Contemporary MMSs usually utilizes expensive dual-frequency CP-DGPS, and fiber optic gyro based IMU to guarantee centimeter of positioning accuracy. Both 2D and 3D LiDARs and various kinds of cameras are integrated to provide accurate and ample measurements.

Typically in systems using 2D LiDAR, multiple LiDARs are mounted at different angles and/or around the vehicle perimeter to capture more of the surroundings (e.g. Figure 2.4). As described in Section 2.2, each LiDAR scanning plane intersects with the 3D environment, and the measurement is the distance to the intersection at each angle on the scanning plane. When the vehicle carrying the MMS moves, the road environment is intersected along several lines, which finally results in a 3D point cloud around the vehicle route (Figure 2.4). In 3D LiDAR based systems, the mounting of LiDAR is more flexible because 3D LiDAR (such as Velodyne HDL-64E) has multiple vertical beams that scans in parallel so that a single spin could build up 360° panoramic 3D point clouds.

In this document, a VELODYNE 3D LiDAR and Ladybug panoramic camera based MMS is described in Chapter 5. In our solution, the vehicle trajectory accuracy is

guaranteed by offline smoothing of all carrier-phase and code GPS and IMU measurements, which relieves the requirement of high precision IMU but still guarantees centimeter accuracy.

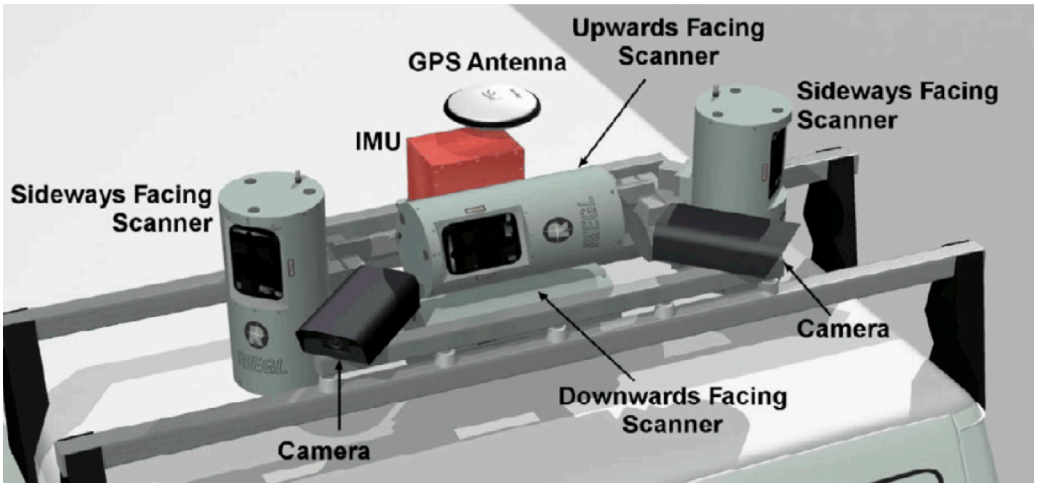

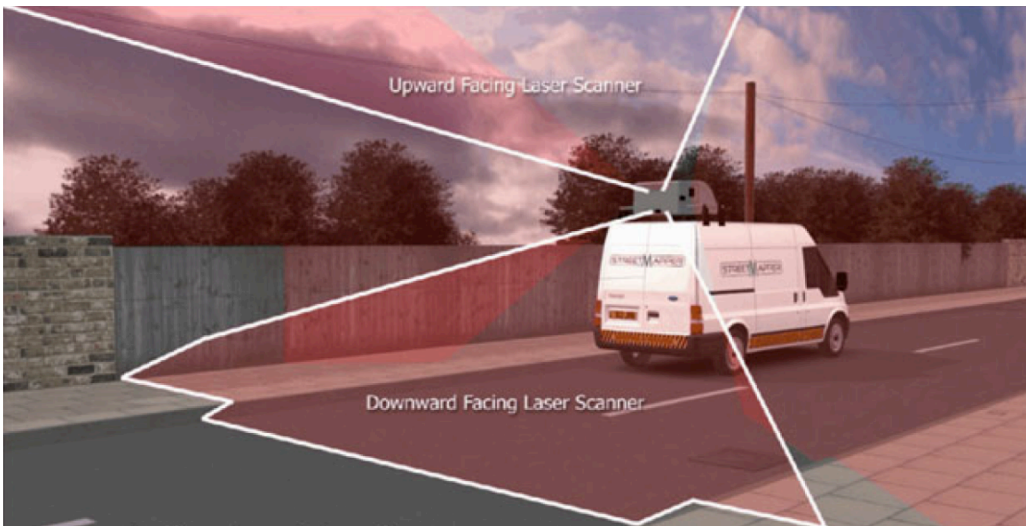

Figure 2.4 StreetMapper™ mobile mapping system [2]. 2D LiDARs are mounted at different angles to capture different parts of the environment. The LiDAR scanning plane intersects with the environment to generate a set of points, and multiple scans could create a 3D point cloud.

2.3.2 Road Feature Extraction Algorithms

Land vehicles equipped with MMS are very suitable for road feature extraction. While vehicle drives around targeted road areas, LiDAR could collect dense and accurate data points of the road environment. The LiDAR detections are time-tagged, so that in post-processing, LiDAR data points in egocentric coordinate frames could be converted to global coordinate frames by referring to the vehicle trajectory at the time tag. This procedure is also called LiDAR point registration. In this way, both 2D and 3D LiDAR could generate a dense 3D point cloud. The accuracy of the resulting 3D point cloud is determined by both LiDAR measurement accuracy and the positioning component accuracy.

After data collection and data registration, road features with specific shapes and laser reflectivity could be extracted. Such features include but not limited to road boundaries, various road markers (e.g. lane markers, turn signs, speed limits, pedestrian crossings), roadside infrastructure (e.g. trees, light poles, traffic signs), railroad crosswalks, manholes, and curb stones. Based on characteristics of the targeted road features, various algorithms are developed. In general, there are three major categories of processing methods.

The first category of algorithms usually applies to road surface feature extraction, such as lane markers, pedestrian crossings, intersection stop-bars, etc. The 3D point cloud is filtered by certain criterion such as height or vertical connectivity to remove non-surface points, and a birds-eye view of the point cloud around road surface is generated. The aforementioned features usually have significantly larger laser reflectivity than

surrounding surfaces, so that in intensity birds-eye image, such features often stand out from background. Image processing algorithms could be applied to the projected 2D image to extract the features. The flattened 2D images could be generated using laser reflectivity, height, and other calculated properties. Examples can be found in [88-90].

In the second category, the 3D point cloud is processed directly. Points in the point cloud are clustered, segmented, and identified based on the properties of the targeted feature. 3D pattern matching is also applicable in this category, such as in [91], the pole along the road is extracted by matching the point cloud to a kernel which consists of a center region where laser points exist, and a rejection region where laser point should not exist. Sometimes, vertical slices of the point cloud are generated and used to identify features with significant height properties [92, 93]. For example, road curbs usually have a vertical height change of 15-40cm from the near-flat road surface.

In the third category, features could be roughly extracted in single LiDAR scans, and then results could be converted to global frame and aggregated for further processing. Because each 3D LiDAR scan already forms a 3D point cloud, some features could be extracted locally in the single scan in LiDAR coordinate frames, then converted to global coordinate frames and do further processing. One example is road curb extraction using this method. Curb candidates could be extracted in each single scans first, and all candidates are aggregated in global coordinate frame, filtered and connected to create the curb line [94]. In [95] and [96], 2D LiDAR single scan on the road are used to detect obstacles or road edges, and then global curb models are used to connect and filter the candidates.

Chapter 5 focuses on one specific road surface feature – intersection stop-bars. The methods to extract other road surface features such as arrows, lane markers could be applied, but the different characteristics of the stop-bars require additional processing to reliably extract them.

2.4 Coordinate Systems

There are several Cartesian coordinate systems used to represent objects' spatial coordinates and attitudes in this document that are shared by both positioning system and mapping system as follows.

- Earth-Centered Earth-Fixed Frame {E}, is used as the global coordinate frame on the Earth. It is centered at the center of mass of the Earth. Its x-axis points to the prime meridian and z axis points to the north. It is fixed with the earth surface, and thus could be used to represent the unique location on Earth surface.
- Local Tangent Frame {G}, is represented as the green rectangle in Figure 2.6. It is determined by fitting a tangent plane to the geodetic reference ellipse at a point of interest [6]. The origin of {G} is fixed to a point on the Earth surface such that it could be used as a global reference frame.
- Body Frame {B}, is defined as the coordinate frame attached to the vehicle. In this document, the axes of the body frame coincide with the IMU's coordinate frame. According to the mounting of IMU with respect to the vehicle, the x axis of the body frame points roughly to the vehicle's heading direction, the z axis points down, the y axis is defined according to right hand rule of the Cartesian coordinates.

- Sensor Frame, is the coordinate frame to represent all sensor detections and is fixed with the sensor itself. In Figure 2.5, {R} is the sensor frame for RADAR.

The transformation relationship among coordinate frame {A} and {B} is represented by translation vector ${}^{A}\mathbf{T}_{AB}$ which is the vector from origin of {A} to the origin of {B} described in {A}, and the rotation matrix ${}^{B}_{A}\mathbf{R}$ which is the rotation matrix from {A} to {B}. Special relationships or details will be described when used.

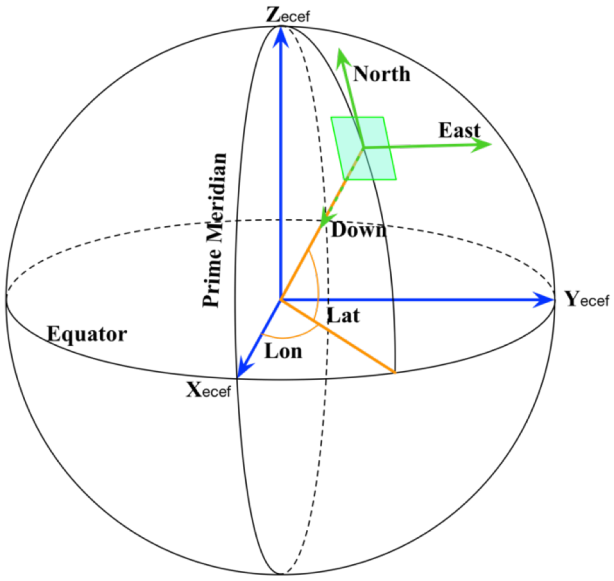

Figure 2.6 LLA, ECEF and Local Tangent (NED) Frames

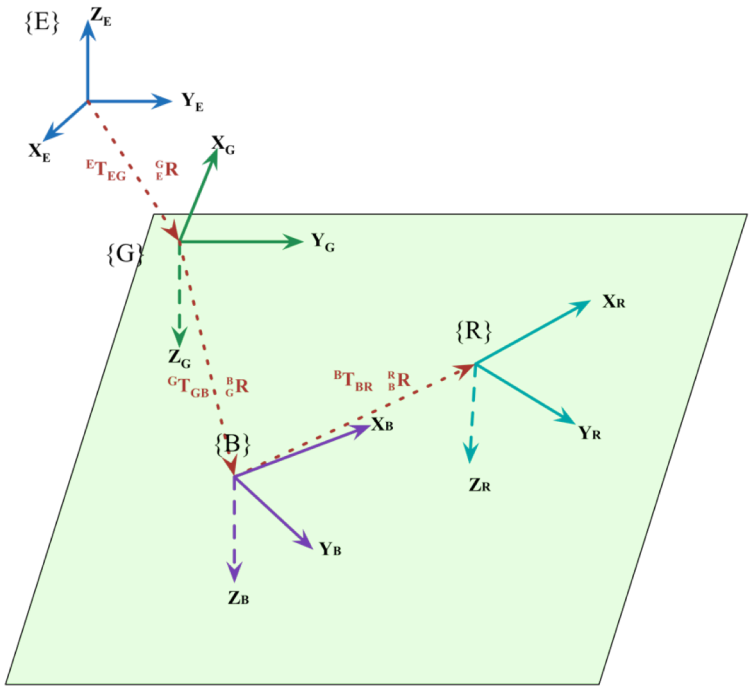

Figure 2.5 Spatial relationship among ECEF frame {E}, Local Tangent Frame {G}, body frame {B} and Sensor frame (Radar as an example) {R}

Chapter 3 Hardware Setup

3.1 Overview

The hardware part of the positioning and mapping system used in this research has four components. The carrier vehicle is a Nissan Altima sedan. The sensors are mounted on a steel plate which is then mounted on the roof of the vehicle. The data collection and real-time positioning computer is a low-profile PC located in the trunk running the Ubuntu 12.04 operating system. The GPS antenna is mounted closely on the IMU box to reduce the level-arm effect. The power system is comprised of two 12-volt batteries which provides 12v DC power to sensors and 110v AC power to the computer through inverter. The vehicle alternator charges the batteries when the engine is running.

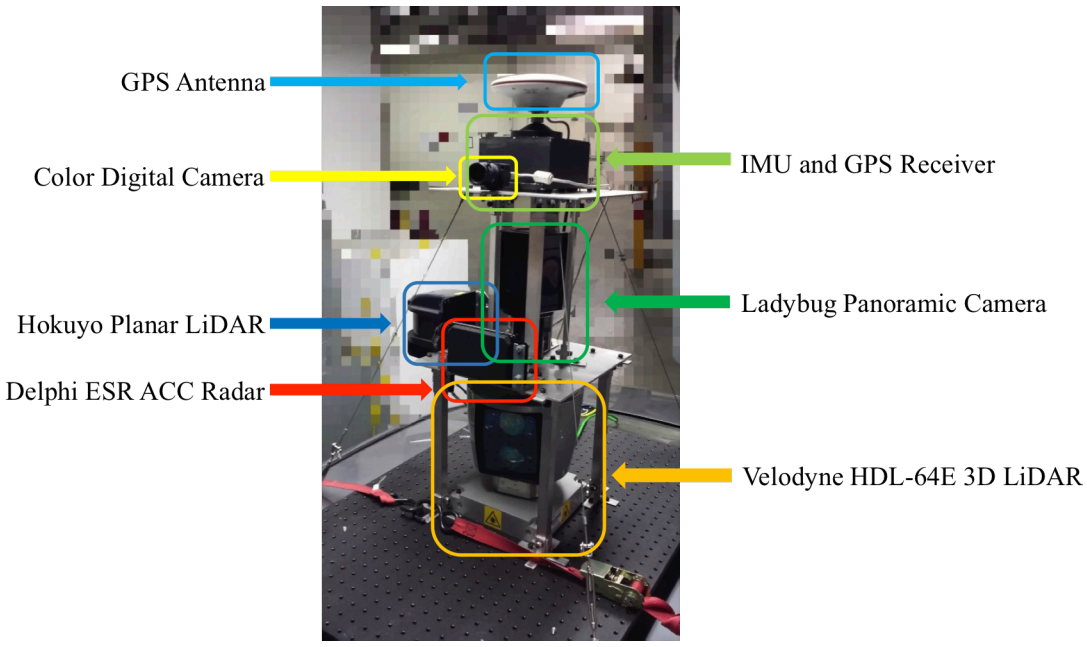

Figure 3.1 Sensor platform.

The sensor platform is illustrated in Figure 3.1. On the top of the platform is the IMU and GPS receiver, which is in the black box. Some of the sensors on this platform are not used in this document, but has been used in other research articles [37, 39]. In Chapter 4, the Delphi RADAR, GPS and IMU is used. In Chapter 5, the whole mapping system includes the Velodyne LiDAR, Ladybug Panoramic Camera, GPS and IMU, however the Ladybug camera is not used in this document.

3.2 Automotive RADAR Sensor

The RADAR sensor used in this dissertation is Delphi Electronically Scanning RADAR (ESR), which is widely applied in the Adaptive Cruise Control (ACC) module in many passenger vehicles (e.g. Volvo s60). Due to mass production and advanced digital electronics design, it is available at low cost (around $1000). This RADAR operates on 77GHz frequency, which is within the regulated frequency band by the Federal Communications Commission. Due to the fact that the wavelength of 77GHz RADAR is 3.89 millimeters, this type of RADAR is also called millimeter-wave

Figure 3.2 Delphi ESR Radar

RADAR. The millimeter wave has superior penetrability through fog, smoke and dust and it can also provide good spatial resolution and high accuracy. The angle measurement is carried out by converting the phase difference of received signals on its antenna array. This prevents the unreliability of mechanically scanning RADAR.

The Delphi's multimode ESR combines simultaneous long-range and short-range modes. The long-range mode could reach up to 174 meters with at horizontal azimuth angle of 20°, while the mid-range mode covers up to 90° of Field Of View (FOV) at a maximum of 60 meters. The stated range measurement noise is smaller than +/- 0.25m and the angular measurement noise is within +/- 1.0°.

The RADAR is connected to a3. local CAN bus, and with the computer through a CAN-USB converter. Each RADAR cycle consists of 64 detections, and all detections are

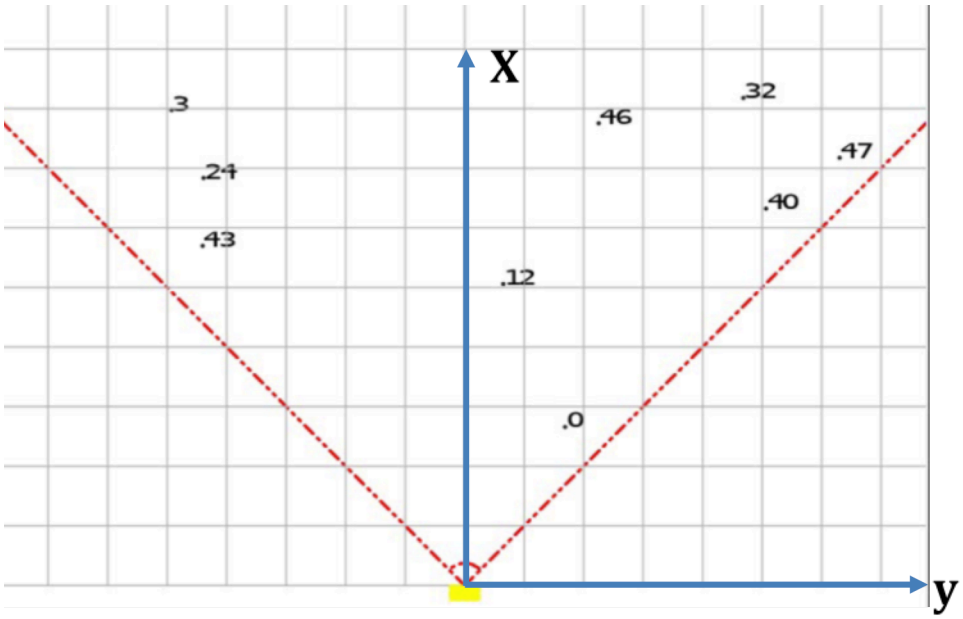

Figure 3.3 Radar detections are converted to 2D coordinates, and plotted on a birds-eye view. The yellow rectangle represents the Radar sensor. The red dashed lines represent the horizontal FOV. Each Radar detection is reported with an ID. In the original ACC Radar firmware, if an object appears in multiple cycles, it would be tracked and its ID will stay the same.

sent as serialized CAN messages. The RADAR is operating at 20Hz, and the detection of each cycle is collected, processed and sent at the next cycle, so that the typical delay is 50ms.

The RADAR measurements consists of ID of object, range, range rate and angle. The RADAR coordinate frame is defined on its detection plane, on which the x-axis points to the front and y-axis to the right (Figure 3.3). In this dissertation, only range and angle are used, and the i-th measurement can be converted to RADAR coordinates with the following equation.

$$\begin{bmatrix} x^i \\ y^i \end{bmatrix} = \begin{bmatrix} d^i \cos\beta^i \\ d^i \sin\beta^i \end{bmatrix},$$

where d^i, β^i are the distance and angle of the i-th measurement.

3.3 Velodyne LiDAR

The 3D LiDAR used in this dissertation is the Velodyne HDL-64E LiDAR. It is mounted under the GPS antenna to prevent the intervention of GPS signals. The LiDAR has 4 groups of 16 laser emitters and 2 groups of 32 laser receivers (Figure 3.4). A single shot of measurements consists of 64 vertically aligned laser range measurements distributed on a 26.8º of vertical FOV. Each of the 64 single LiDAR measurements comprises distance and intensity, while the angle of the detection is calculated according to the current rotation angle of the housing and the fixed angle of the laser.

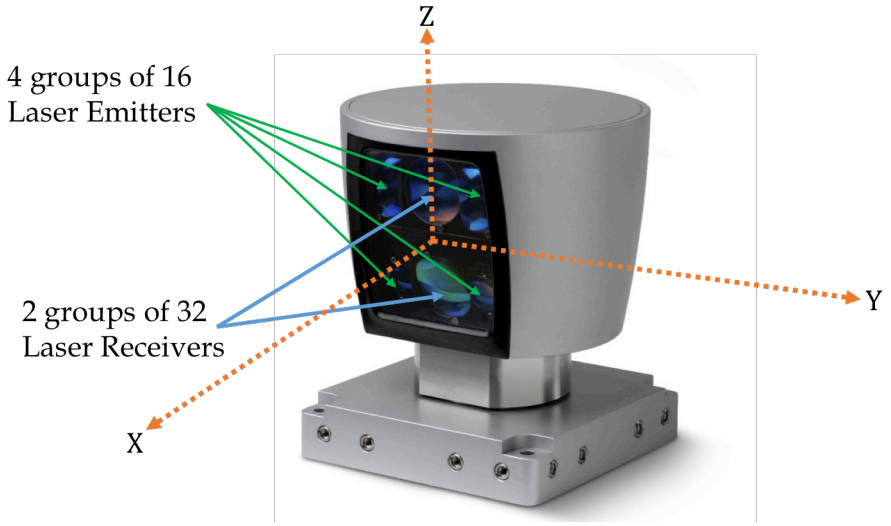

Figure 3.4 Velodyne HDL-64E [1]

The LiDAR coordinate frame is illustrated in Figure 3.4. Z-axis is the spinning axis of the LiDAR housing, while the X-axis is fixed to point to the front. In an ideal case where laser emitters and receivers are aligned perfectly, the measurement of a single laser could be converted to Cartesian coordinates within the coordinate frame illustrated in Figure 3.4 using the following equations:

$$\begin{bmatrix} x_i \\ y_i \\ z_i \end{bmatrix} = \begin{bmatrix} s_i R_i \cos\delta_i \sin\varepsilon \\ s_i R_i \cos\delta_i \cos\varepsilon \\ s_i R_i \sin\delta_i \end{bmatrix}, \quad (1)$$

where:

s_i is the distance scale factor for laser i;

R_i is the raw distance measurement from laser i to the reflected object;

δ_i is the angle of laser i's direction with respect to the x-y plane;

ε is the rotation angle of the housing with respect to the x-z plane.

In practice, several offset and calibration parameters are involved in the conversion. This conversion was carried out based on the offsets, the calibration parameters and equations are provided by the manufacturer. This calibration procedure is not described here.

The Velodyne LiDAR spins at 10 cycles per second. All LiDAR data is transferred to the computer via Ethernet connection, and time-tagged with the received GPS time for data registration. A typical LiDAR cycle of 360º of 3D measurements is illustrated in Figure 3.5. The level of brightness represents the intensity of reflected signal returned by the LiDAR. The advantage of the 3D LiDAR is that it not only preserves the spatial structure of the environment, but also discriminates highly reflective objects. In this dissertation, the bright stop-bars are of interest.

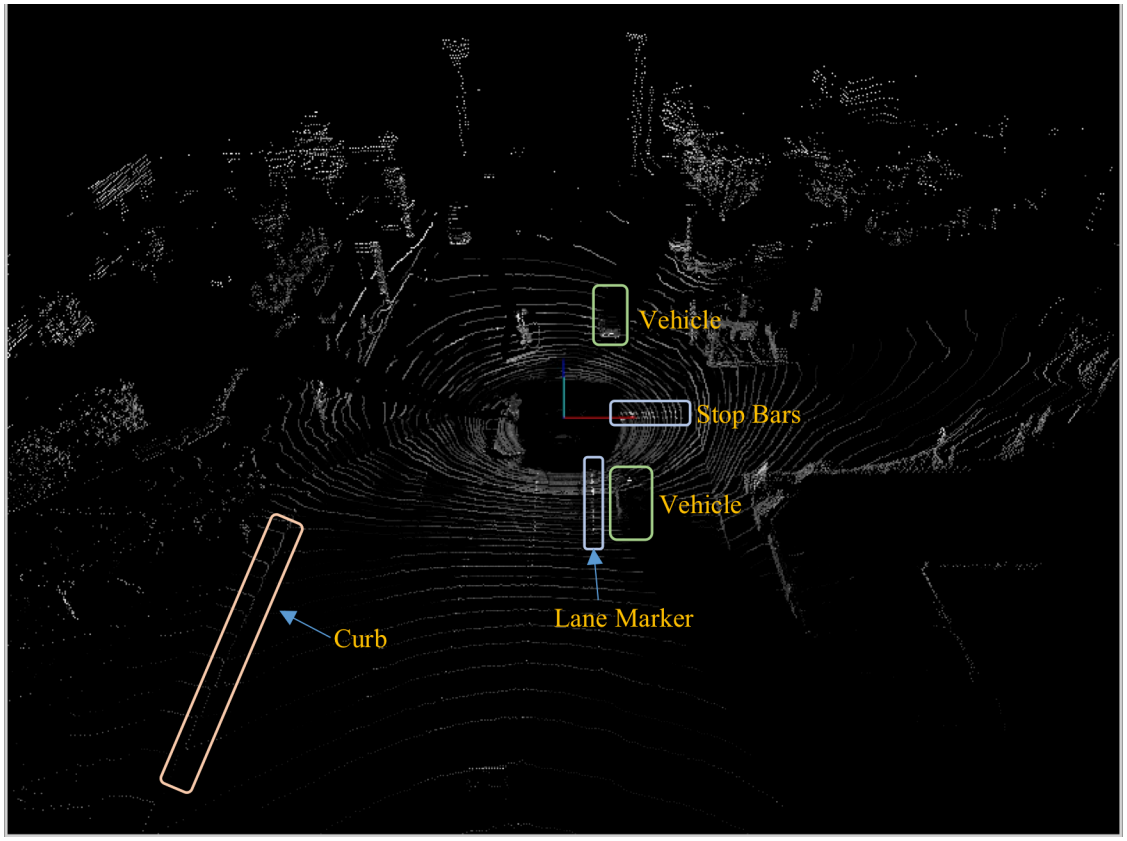

Figure 3.5 Point cloud intensity image of one 360º cycle. The center of the image is the LiDAR sensor on the test vehicle. Shapes like road curbs, trees, vehicles and building facets can be easily identified by the human eye in such images. Highly reflective objects are also identifiable such as lane markers and stop-bars.

Chapter 4 RADAR/DGPS-aided INS

4.1 Introduction

In this chapter, a real-time automotive RADAR aided DGPS/INS positioning system is proposed, where both GPS and RADAR sensor are tightly coupled with an IMU. A standard Extended Kalman Filter (EKF) is implemented to integrate sensors to provide continuous vehicle pose estimation. In this case, the high-rate IMU provides six degree-of-freedom (DOF) inputs to the vehicle kinematic model, while pseudo-range

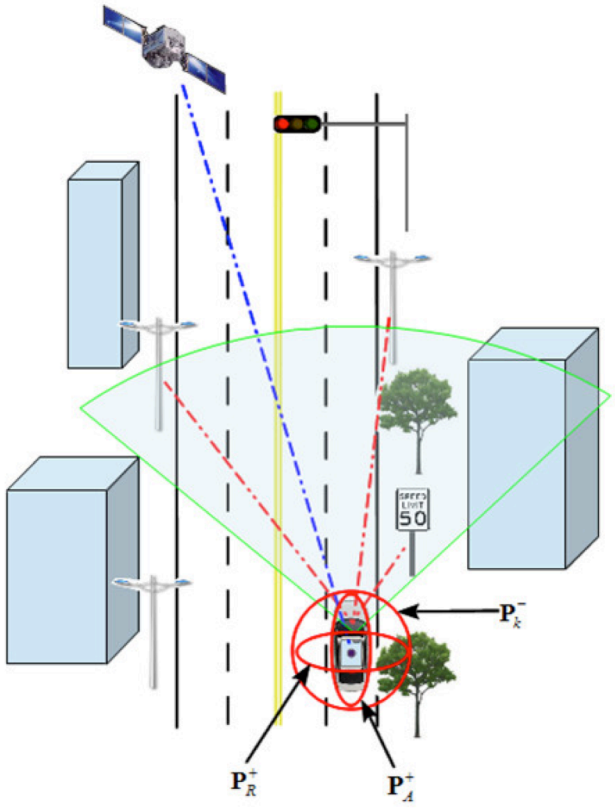

Figure 4.1 A bird's-eye view of the overall positioning scenario in urban canyon. Tall buildings along the roads could block GPS signals, leaving only satellites in the front or in the behind as receivable. Radar will measure relative position of roadside landmarks, and update the vehicle position estimate.

measurements from GPS and RADAR measurements are then integrated to update vehicle state estimates. An illustrative scenario is shown in Figure 4.1. In such roadway scenario, the RADAR sensor could use relative position of point features (e.g. traffic signs) and pole features (e.g. light poles) to assist position estimation. In section 4.2, the vehicle kinematic model, GPS measurement model, and RADAR measurement model, and error analysis model will be presented. In section 4.3, experiments that simulates general roadway scenario are then presented, with analysis to prove the effectiveness of automotive RADAR as complement to GNSS.

4.2 Methodology

4.2.1 Sensors Arrangements

On the sensor platform, the IMU/GPS is mounted on the top of upper panel to prevent blockage of GPS signals, while the IMU coordinate frame is used as the vehicle's body coordinate frame. The RADAR sensor is mounted on the lower panel, facing forward, so that the x-axis of the RADAR coordinate frame roughly coincides with the x-axis of the IMU. The mounting position, attitude and sensor FOV are illustrated in Figure 4.2. In this study, the IMU provides 6 Degree Of Freedom (DOF) measurements. Its measurement model is described in Section 4.2.2.1. The GPS receiver provides measurements of pseudo-range, Doppler and carrier-phase. The carrier-phase measurement aided INS can attain centimeter-level accuracy, and thus is used as a ground-truth to demonstrate the performance of the proposed system.

In this study, the origin of the local tangent frame {G} is chosen as the antenna position of our own GPS base station. The experiments are taken in the vicinity of the

GPS base station. The state of the vehicle includes the position, velocity and attitude of the body frame {B} with respect to {G}.

4.2.2 DGPS/INS System

4.2.2.1 Inertial Measurement Unit

The six Degree of Freedom Inertial Measurement Unit (IMU) measures the three-dimensional specific force ${}^{B}\tilde{\boldsymbol{a}}$ by accelerometer and rotational rate ${}^{B}\tilde{\boldsymbol{\omega}}$ by gyroscope. They are modeled as:

$$\begin{aligned} {}^{B}\tilde{\boldsymbol{a}} &= {}^{B}\boldsymbol{a}_{iB} - {}^{B}\boldsymbol{g} + {}^{B}\mathbf{b}_{a} + {}^{B}\mathbf{n}_{a} \\ {}^{B}\tilde{\boldsymbol{\omega}} &= {}^{B}\boldsymbol{\omega}_{iB} + {}^{B}\mathbf{b}_{g} + {}^{B}\mathbf{n}_{g}, \end{aligned} \tag{2}$$

where ${}^{B}\boldsymbol{a}_{iB}$ and ${}^{B}\boldsymbol{\omega}_{iB}$ are defined as the acceleration and angular rate vectors of the body frame $\{B\}$ with respect to the inertial frame $\{i\}$ described in $\{B\}$, and they are used in the following kinematic equations. The vector $\mathbf{u}(t) = \left[{}^{B}\boldsymbol{a}_{iB}(t)^{T} \quad {}^{B}\boldsymbol{\omega}_{iB}(t)^{T} \right]^{T}$ is the input to the vehicle kinematic models. The IMU biases are modeled as random walk processes

$${}^{B}\dot{\mathbf{b}}_{a} = {}^{B}\mathbf{n}_{ba}, \; {}^{B}\dot{\mathbf{b}}_{g} = {}^{B}\mathbf{n}_{bg}, \tag{3}$$

where the power spectral densities of ${}^{B}\mathbf{n}_{ba}$ and ${}^{B}\mathbf{n}_{bg}$ are positive definite matrices $\mathbf{Q}_{ba}$ and $\mathbf{Q}_{bg}$, respectively.

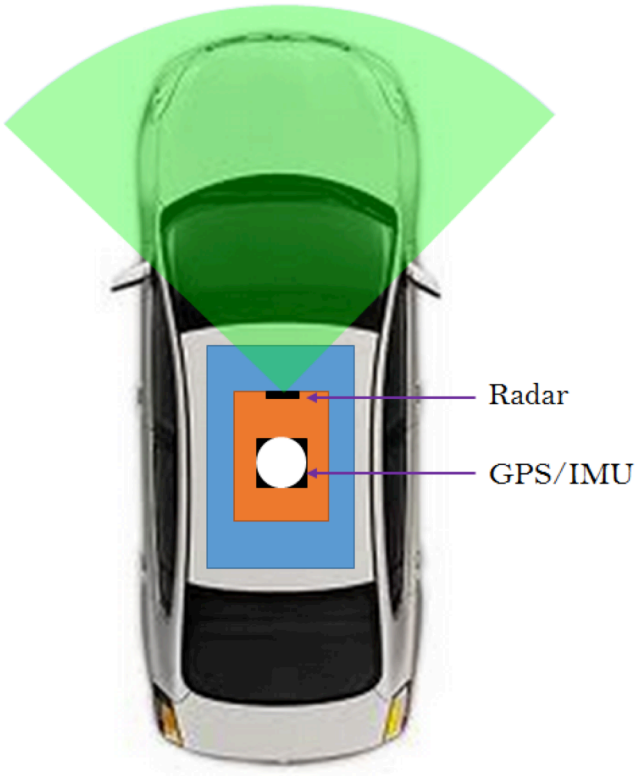

Figure 4.2. Sensor Arrangement.

4.2.2.2 Vehicle Kinematic Model – What the nature does

The state of the vehicle ${}^{G}\mathbf{x}_{B}$ is the state of the IMU frame (i.e. $\{B\}$) with respect to the global frame $\{G\}$. The states abide by a set of differential equations known as the kinematic model,

$$ {}^{G}\dot{\mathbf{x}}_{B}(t) = f\big({}^{G}\mathbf{x}_{B}(t), \mathbf{u}(t)\big). \tag{4} $$

Specifically, the set of equations is

$$ \begin{aligned} {}^{G}\dot{\mathbf{p}}_{B} &= {}^{G}\mathbf{v}_{B} \\ {}^{G}\dot{\mathbf{v}}_{B} &= {}^{R}_{B}\mathbf{R}\,{}^{B}\boldsymbol{a}_{iB} - 2\,{}^{G}\boldsymbol{\Omega}_{iE}\,{}^{G}\mathbf{v}_{B} \\ {}^{G}_{B}\dot{\mathbf{R}} &= {}^{G}_{B}\mathbf{R}\big({}^{B}\boldsymbol{\Omega}_{iB} - {}^{B}\boldsymbol{\Omega}_{iE}\big), \end{aligned} \tag{5} $$

where the state vector of the vehicle is ${}^{G}\mathbf{x}_B = \begin{bmatrix} {}^{G}\mathbf{p}_B^T & {}^{G}\mathbf{v}_B^T & {}^{G}\boldsymbol{\theta}_B^T \end{bmatrix}^T$, including position ${}^{G}\mathbf{p}_B$, velocity ${}^{G}\mathbf{v}_B$ and an equivalent representation of the rotation matrix ${}^{B}_{G}\mathbf{R}$, either in Euler angles or quaternions form which is represented as ${}^{G}\boldsymbol{\theta}_B$. The skew symmetric matrix $\boldsymbol{\Omega}$ spanned from vector $\boldsymbol{\omega} = [\omega_1 \quad \omega_2 \quad \omega_3]^T$ is defined as

$$\boldsymbol{\Omega} = \lfloor \boldsymbol{\omega} \times \rfloor = \begin{bmatrix} 0 & -\omega_3 & \omega_2 \\ \omega_3 & 0 & -\omega_1 \\ -\omega_2 & \omega_1 & 0 \end{bmatrix}. \tag{6}$$

In Equation (5), the vector ${}^{B}\boldsymbol{\omega}_{iE}$ that spans ${}^{B}\boldsymbol{\Omega}_{iE}$ is the angular rate of the ECEF frame with respect to an inertial frame described in $\{B\}$, and similarly ${}^{B}\boldsymbol{\omega}_{iB}$ which spans ${}^{B}\boldsymbol{\Omega}_{iB}$ is the true angular rate vector of $\{B\}$ with respect to some inertial frame. The acceleration and angular rate vectors are described with respect to the inertial frame. Because the ECEF is not a strict inertial frame, its autorotation rate ${}^{B}\boldsymbol{\omega}_{iE}$ is modeled in the kinematic equations.

External sensors such as GPS, LiDAR, RADAR, camera provide measurements to the observables of the system. The measurement model is a function of the system states ${}^{G}\mathbf{x}_B(t)$ and additive measurement noise.

$$\tilde{\mathbf{z}} = h\big({}^{G}\mathbf{x}_B(t)\big) + \mathbf{n}_z, \tag{7}$$

where $\mathbf{n}_z$ is the measurement noise vector and its covariance is the positive definite matrix $\mathbf{R}$.

4.2.2.3 Mechanization Model – What the navigation system does

The navigation system maintains the estimated state vector of the vehicle and the estimate of IMU biases. The augmented state vector is

$$\hat{\mathbf{x}}_B = \left[{}^{G}\hat{\mathbf{p}}_B^T \quad {}^{G}\hat{\mathbf{v}}_B^T \quad {}^{G}\hat{\boldsymbol{\theta}}_B^T \quad {}^{B}\hat{\mathbf{b}}_a^T \quad {}^{B}\hat{\mathbf{b}}_g^T \right]^T, \tag{8}$$

where $\hat{\mathbf{x}}_B$ is vehicle states reported by the navigation system. The state vector is continuously estimated by numerically integrating the following equations as the mechanization equations $\dot{\hat{\mathbf{x}}}_B(t) = f\left(\hat{\mathbf{x}}_B(t), \hat{\mathbf{u}}(t)\right)$:

$$\begin{aligned}
{}^{G}\dot{\hat{\mathbf{p}}}_B &= {}^{G}\hat{\mathbf{v}}_B \\
{}^{G}\dot{\hat{\mathbf{v}}}_B &= {}^{G}_{B}\hat{\mathbf{R}}\, {}^{B}\hat{\boldsymbol{a}}_{iB} - 2\, {}^{G}\hat{\boldsymbol{\Omega}}_{iE}\, {}^{G}\hat{\mathbf{v}}_B \\
{}^{G}_{B}\dot{\hat{\mathbf{R}}} &= {}^{G}_{B}\hat{\mathbf{R}}\left({}^{B}\hat{\boldsymbol{\Omega}}_{iB} - {}^{B}\hat{\boldsymbol{\Omega}}_{iE} \right) \\
{}^{B}\dot{\hat{\mathbf{b}}}_a &= \mathbf{0}_{3\times 1} \\
{}^{B}\dot{\hat{\mathbf{b}}}_g &= \mathbf{0}_{3\times 1}.
\end{aligned} \tag{9}$$

The system input $\hat{\mathbf{u}}(t)$ is the estimated acceleration and angular rate vectors calculated from the IMU raw measurements with the following equations

$$\hat{\mathbf{u}}(t) = \begin{bmatrix} {}^{B}\hat{\boldsymbol{a}}_{iB} \\ {}^{B}\hat{\boldsymbol{\omega}}_{iB} \end{bmatrix} = \begin{bmatrix} {}^{B}\tilde{\boldsymbol{a}} + {}^{B}_{G}\hat{\mathbf{R}}\, {}^{G}\hat{\boldsymbol{g}} - {}^{B}\hat{\mathbf{b}}_a \\ {}^{B}\tilde{\boldsymbol{\omega}} - {}^{B}\hat{\mathbf{b}}_g \end{bmatrix}. \tag{10}$$

Similarly, the navigation system also predicts the external sensor measurements using the same measurement model (7), but replacing the true system state with the estimated state. The measurement prediction equations are

$$\hat{\mathbf{z}} = h\left(\hat{\mathbf{x}}_B(t)\right), \tag{11}$$

where the measurement noise term is assumed

4.2.2.4 Error Analysis

In EKF framework, besides state estimation, the probabilistic distribution of the estimated states is also estimated. This is directly related to the error analysis. Error states are defined as $\delta\mathbf{x} = \mathbf{x} - \hat{\mathbf{x}}$, which in detail is, $\delta\mathbf{x} = [\delta\mathbf{p} \quad \delta\mathbf{v} \quad \boldsymbol{\rho} \quad \delta\mathbf{b}_a \quad \delta\mathbf{b}_g]^T$. The

symbol $\boldsymbol{\rho}$ a 3×1 vector representing the attitude error in local tangent frame. The time propagation of the error states is

$$\delta\dot{\mathbf{x}} = f\left({}^{G}\mathbf{x}_B(t), \mathbf{u}(t)\right) - f\left({}^{G}\hat{\mathbf{x}}_B(t), \hat{\mathbf{u}}(t)\right), \tag{12}$$

The error state propagation model linearized around ${}^{G}\hat{\mathbf{x}}_B(t)$ and $\hat{\mathbf{u}}(t)$

$$\dot{\delta\mathbf{x}} = \mathbf{F}\delta\mathbf{x} + \mathbf{G}\mathbf{n}, \tag{13}$$

where $\mathbf{F} = \frac{\partial f}{\partial \mathbf{x}}\Big|_{\mathbf{x}=\hat{\mathbf{x}},\mathbf{u}=\hat{\mathbf{u}}}$, $\mathbf{G} = \frac{\partial f}{\partial \mathbf{n}}\Big|_{\mathbf{x}=\hat{\mathbf{x}},\mathbf{u}=\hat{\mathbf{u}}}$ and the noise vector $\mathbf{n} = \begin{bmatrix}\mathbf{n}_a^T & \mathbf{n}_g^T & \mathbf{n}_{ba}^T & \mathbf{n}_{bg}^T\end{bmatrix}^T$.

The detailed derivation of matrix $\mathbf{F}$ and $\mathbf{G}$ can be found in Section 11.6 of [6], $\mathbf{n}_a$, $\mathbf{n}_g$represent measurement noise processes of the accelerometer and gyro respectively and $\mathbf{n}_{ba}$, $\mathbf{n}_{bg}$ are already described in Section 4.2.2. The IMU noise vectors are modeled as Gaussian white noise processes, and their power spectral densities are positive definite matrices $\mathbf{Q}_a$ and $\mathbf{Q}_g$.

A discrete form of the propagation equations needs to be used in practical implementations. The IMU measurements are sampled at $1/T$ frequency, the states are also propagated at the same frequency. The discrete time transition matrix is $\boldsymbol{\Phi} = e^{FT}$. Detailed derivation can be found on Section 3.5.5 of [6]. The propagated covariance is

$$\mathbf{P}_k^- = \boldsymbol{\Phi}\mathbf{P}_{k-1}^{-1}\boldsymbol{\Phi}^{-1} + \mathbf{Q}_d. \tag{14}$$

Similar to state estimation error, the measurement residue is defined as $\delta\mathbf{z} = \tilde{\mathbf{z}} - \hat{\mathbf{z}}$. The linearized residue model is computed as

$$\delta\mathbf{z} = \mathbf{H}\delta\mathbf{x} + \mathbf{n}_z, \tag{15}$$

where $\mathbf{H} = \frac{\partial h}{\partial \mathbf{x}}\Big|_{\mathbf{x}=\hat{\mathbf{x}}_k^-}$ is also computed at every time instant t_k.

The residue covariance s is computed as

$$\mathbf{S}_k = \mathbf{H}_k \mathbf{P}_k^- \mathbf{H}_k^T + \mathbf{R}, \tag{16}$$

where $\mathbf{P}_k^-$ is the propagated state covariance, $\mathbf{R}_k$ is the measurement covariance matrix. The Kalman gain and state update equations are

$$\begin{aligned} \mathbf{K}_k &= \mathbf{P}_k^- \mathbf{H}_k^T \mathbf{S}_k^{-1} \\ \mathbf{x}_k^+ &= \hat{\mathbf{x}}_k^- + \mathbf{K}_k \delta \mathbf{z}_k \\ \mathbf{P}_k^+ &= (\mathbf{I} - \mathbf{K}_k \mathbf{H}_k) \mathbf{P}_k^-. \end{aligned} \tag{17}$$

4.2.2.5 GPS Measurement Model

The use of GPS measurements with IMU in a tightly-coupled architecture is summarized in this section. Detailed analysis and derivation of GPS measurement models and error sources are presented in Chapter 8 and 11 of [6]. In this section, only the key equations are described.

Typically, low-cost single frequency (L1) GPS provides three types of observables (pseudo-range, Doppler, and carrier-phase signals) where direct line-of-sight exists between GPS receiver antenna and the satellite vehicle. The pseudorange between the GPS receiver antenna $\mathbf{p}$ and the i[th] satellite vehicle $\hat{\mathbf{p}}_{sv}^i$ comprises both actual distance $\left\|\mathbf{p} - \hat{\mathbf{p}}_{sv}^i\right\|_2$ and the receiver clock offset term Δt_r, and is described as

$$\rho\left(\mathbf{p}, \hat{\mathbf{p}}_{sv}^i\right) = \left\|\mathbf{p} - \hat{\mathbf{p}}_{sv}^i\right\|_2 + c\Delta t_r, \tag{18}$$

where c is the speed of light in vacuum.

The pseudorange and Doppler measurement models are

$$\begin{aligned} \tilde{\rho}^i &= \rho\left(\mathbf{p}, \hat{\mathbf{p}}_{sv}^i\right) + c\Delta t^i + \frac{f_2}{f_2} I_r^i + T_r^i + E^i + M_\rho^i + n_\rho^i \\ \lambda D_r^i &= \vec{\mathbf{U}}_{ir}^T \left(\mathbf{v}_r - \mathbf{v}_{sv}^i\right) + c\Delta \dot{t}_r - c\Delta \dot{t}^i + n_D^i. \end{aligned} \tag{19}$$

The pseudorange measurement equation contains several error sources, in which Δt^i is the satellite clock error; I_r^i and T_r^i are atmospheric errors; E^i is the ephemeris error; M_ρ^i is the multipath error; n_ρ^i is the pseudorange measurement noise. The Doppler measurement is treated as the instantaneous relative velocity between satellite vehicle and receiver antenna. In the Doppler measurement equation, λ is the carrier wavelength; the vector $\vec{\mathbf{U}}_{ir} = (\mathbf{p} - \hat{\mathbf{p}}_{sv}^i)/\left\|\mathbf{p} - \hat{\mathbf{p}}_{sv}^i\right\|$ is the unit vector pointing from the satellite vehicle to the receiver antenna; $\mathbf{v}_r$ and $\mathbf{v}_{sv}^i$ are velocity of the receiver and ith satellite vehicle respectively; n_D^i is the Doppler measurement noise. Differential GPS methods could eliminate common mode errors $\Delta t^i, I_r^i, T_r^i$ and E^i. The receiver clock error Δt_r could be eliminated using double differencing methods. Linearized measurement equations of pseudo-range and Doppler measurements using the double differencing method are

$$\mathbf{H}_k = \begin{bmatrix} {}^N\vec{\mathbf{U}}_{0r}^T - {}^N\vec{\mathbf{U}}_{ir}^T & \mathbf{0} & \mathbf{0} & \mathbf{0} & \mathbf{0} \\ \mathbf{0} & {}^N\vec{\mathbf{U}}_{0r}^T - {}^N\vec{\mathbf{U}}_{ir}^T & \mathbf{0} & \mathbf{0} & \mathbf{0} \end{bmatrix}, \tag{20}$$

where subscript 0 represents the satellite index at the highest elevation.

Satellite signals will only reach the receiver directly when the line-of-sight between the receiver and satellite is unobstructed. Consequently, when the GPS receiver antenna is in an urban areas -- especially where buildings, trees and other obstacles block signals from lateral directions -- only signals from satellites along the road will be received. In such situations, GPS can maintain accuracy of the position vector along, but not perpendicular to the roadway.

4.2.3 RADAR Processing

As is demonstrated in Section 3.2, the Delphi ESR RADAR provides three separate measurements, range, range rate and angle. In our system, the range d and angle β are integrated. The measurement model of the i[th] RADAR detection $\tilde{\mathbf{z}}^i = \begin{bmatrix} {}^R\tilde{d}^i & {}^R\tilde{\beta}^i \end{bmatrix}^T$ is

$$\begin{aligned} {}^R\tilde{d}^i &= \left\| {}^R\mathbf{p}_L^i \right\| + n_d = \sqrt{({}^Rx^i)^2 + ({}^Ry^i)^2} + n_d \\ {}^R\tilde{\beta}^i &= \operatorname{atan2}\left({}^Ry^i, {}^Rx^i\right) + n_\beta, \end{aligned} \tag{21}$$

where $[n_d, n_\beta]$ is the vector measurement noise process which is modeled as independent Gaussian white noise whose covariance is the diagonal matrix

$$\mathbf{R} = \begin{bmatrix} \sigma_d^2 & 0 \\ 0 & \sigma_\beta^2 \end{bmatrix} \tag{22}$$

The vector ${}^R\mathbf{p}_L^i = \begin{bmatrix} {}^Rx^i, {}^Ry^i \end{bmatrix}^T$ is the sensor frame egocentric 2D coordinate of the intersection of the object with the RADAR FOV plane. The RADAR detection is based on the total reflective intensity, so for large objects, the RADAR detections are hardly dense enough to show the boundaries, and sometimes when the objects are far away, the sparse RADAR detection results on the objects could hardly identify the shape of the objects. Based on RADAR's specific characteristics, two types of landmarks that could be identified and measured comparatively more accurate are selected and modeled. The point and pole feature measurement models are described below.

4.2.3.1 Point Feature Model

The position of the i[th] point landmark ${}^{G}\mathbf{p}_L^i \in \mathbb{R}^3$ describes the north, east and down coordinate of the point feature in local tangent frame. Due to beam forming width of RADAR pulse, its FOV plane is not an ideal plane but has a 4º vertical field-of-view. The point feature will be detected if it is within the vertical field-of-view.

The landmark position in $\{R\}$ is obtained by transforming its global position using RADAR's extrinsic calibration parameters ${}^{B}\mathbf{T}_{RB}$, ${}_{B}^{R}\mathbf{R}$ and vehicle's true states ${}^{G}\mathbf{p}_B$, ${}_{G}^{B}\mathbf{R}$

$$ {}^{R}\mathbf{p}_L^i = {}_{B}^{R}\mathbf{R}\left({}_{G}^{B}\mathbf{R}\left({}^{G}\mathbf{p}_L^i - {}^{G}\mathbf{p}_B\right) + {}^{B}\mathbf{T}_{RB}\right). \tag{23} $$

The predicted measurements in the EKF update stage come from the predicted landmark position ${}^{R}\hat{\mathbf{p}}_L^i$ which is calculated using the equation

$$ {}^{R}\hat{\mathbf{p}}_L^i = {}_{B}^{R}\mathbf{R}\left({}_{G}^{B}\hat{\mathbf{R}}\left({}^{G}\hat{\mathbf{p}}_L^i - {}^{G}\hat{\mathbf{p}}_B\right) + {}^{B}\mathbf{T}_{RB}\right), \tag{24} $$

where ${}^{G}\hat{\mathbf{p}}_L^i$ is known a priori.

Although the RADAR FOV has a vertical extent, it does not measure the actual angle in the vertical direction, so when the point feature is within the RADAR's detection plane, we consider the third dimension of the landmark position in $\{R\}$ as 0.

The predicted measurements $\tilde{\mathbf{z}}^i$ are calculated by

$$ \begin{aligned} {}^{R}\hat{d}^i &= \left\| {}^{R}\hat{\mathbf{p}}_L^i \right\|_2 = \sqrt{{}^{R}\hat{x}^{i\,2} + {}^{R}\hat{y}^{i\,2}} \\ {}^{R}\hat{\beta}^i &= \operatorname{atan2}\left({}^{R}\hat{y}^i, {}^{R}\hat{x}^i\right). \end{aligned} \tag{25} $$

where ${}^{R}\hat{x}^{i}$ and ${}^{R}\hat{y}^{i}$ are the first two dimensions of ${}^{R}\hat{\mathbf{p}}^{i}$The linearized measurement matrix **H** for Equation (15) is

$$\mathbf{H} = \mathbf{A}\,{}^{R}_{B}\mathbf{R}\,{}^{B}_{G}\widehat{\mathbf{R}}\left[-\mathbf{I} \quad \mathbf{0} \quad \left\lfloor {}^{G}\widehat{\mathbf{T}}_{Bi}\times\right\rfloor \quad \mathbf{0} \quad \mathbf{0}\right] \tag{26}$$

$$\mathbf{A} = \begin{bmatrix} \frac{{}^{R}\mathbf{e}_1 \cdot {}^{R}\hat{\mathbf{p}}_L^i}{\|{}^{R}\hat{\mathbf{p}}_L^i\|} & \frac{{}^{R}\mathbf{e}_2 \cdot {}^{R}\hat{\mathbf{p}}_L^i}{\|{}^{R}\hat{\mathbf{p}}_L^i\|} & 0 \\ \frac{-{}^{R}\mathbf{e}_2 \cdot {}^{R}\hat{\mathbf{p}}_L^i}{\|{}^{R}\hat{\mathbf{p}}_L^i\|^2} & \frac{{}^{R}\mathbf{e}_1 \cdot {}^{R}\hat{\mathbf{p}}_L^i}{\|{}^{R}\hat{\mathbf{p}}_L^i\|^2} & 0 \end{bmatrix}, \tag{27}$$

where the vector ${}^{G}\widehat{\mathbf{T}}_{Bi}$ is the vector from the origin of $\{B\}$ to ${}^{G}\mathbf{p}_L^i$ described in $\{G\}$:

$${}^{G}\widehat{\mathbf{T}}_{Bi} = {}^{G}\mathbf{p}_L^i - {}^{G}\widehat{\mathbf{p}}_B. \tag{28}$$

and ${}^{R}\mathbf{e}_1 = [1 \quad 0 \quad 0]^T$, ${}^{R}\mathbf{e}_2 = [0 \quad 1 \quad 0]^T$.

4.2.3.2 Vertical Line Feature Model

A vertical line feature represents a straight pole-shaped landmark which is fixed to the ground. The vertical line feature can be described by a fixed point on the line ${}^{G}\mathbf{p}_{Li}$ and a vector along the line ${}^{G}\mathbf{v}_{Li}$ that represents the direction. The description of the line in $\{R\}$ relates to that in $\{G\}$ with the following equation

$$\begin{aligned} {}^{R}\mathbf{p}_L^i &= {}^{R}_{B}\mathbf{R}\left({}^{B}_{G}\mathbf{R}\left({}^{G}\mathbf{p}_L^i - {}^{G}\mathbf{p}_B\right) + {}^{B}\mathbf{T}_{RB}\right) \\ {}^{R}\mathbf{v}_L^i &= {}^{R}_{B}\mathbf{R}\,{}^{B}_{G}\mathbf{R}\,{}^{G}\mathbf{v}_L^i. \end{aligned} \tag{29}$$

To predict the measurements, the predicted line description in $\{R\}$ is obtained by replacing ${}^{G}\mathbf{p}_B$ and ${}^{B}_{G}\mathbf{R}$ in the equation above with the estimated vehicle states ${}^{G}\hat{\mathbf{p}}_B$ and ${}^{B}_{G}\widehat{\mathbf{R}}$. The detection point ${}^{R}\mathbf{p}_d$ is the intersection of this (geodetic frame vertical) line and the RADAR FOV plane, which can be written as

$$\begin{aligned} {}^{R}\mathbf{p}_d &= {}^{R}\mathbf{p}_L^i + s\,{}^{R}\mathbf{v}_L^i \\ 0 &= {}^{R}\boldsymbol{\pi} \cdot {}^{R}\mathbf{p}_d, \end{aligned} \tag{30}$$

where $\boldsymbol{s} \in \mathbb{R}$ is the (unknown) distance between ${}^{R}\mathbf{p}_d$ and ${}^{R}\mathbf{p}_L^i$, the vector ${}^{R}\boldsymbol{\pi} = [0 \quad 0 \quad 1]^T$ is the normal vector to the RADAR FOV plane in $\{R\}$. Equation (30) describes the constraint that ${}^{R}\mathbf{p}_d$ is on the line and the constraint that ${}^{R}\mathbf{p}_d$ is also on the RADAR detection plane. Eliminating the unknown variable *s* in (30), we calculate ${}^{R}\mathbf{p}_d$ as

$$ {}^{R}\mathbf{p}_d = {}^{R}\mathbf{p}_L^i - {}^{R}\mathbf{v}_L^i \frac{{}^{R}\boldsymbol{\pi} \cdot {}^{R}\mathbf{p}_L^i}{{}^{R}\boldsymbol{\pi} \cdot {}^{R}\mathbf{v}_L^i}. \tag{31} $$

The predicted intersection point can be calculated using estimated terms ${}^{R}\hat{\mathbf{p}}_L^i$ and ${}^{R}\hat{\mathbf{v}}_L^i$ in (31)

$$ {}^{R}\hat{\mathbf{p}}_d = {}^{R}\hat{\mathbf{p}}_L^i - {}^{R}\hat{\mathbf{v}}_L^i \frac{{}^{R}\boldsymbol{\pi} \cdot {}^{R}\hat{\mathbf{p}}_L^i}{{}^{R}\boldsymbol{\pi} \cdot {}^{R}\hat{\mathbf{v}}_L^i}. \tag{32} $$

According to (30), ${}^{R}\hat{\mathbf{p}}_d$ has the form of $\begin{bmatrix} {}^{R}x_d & {}^{R}y_d & 0 \end{bmatrix}^T$. The measurement prediction is calculated by replacing ${}^{R}\hat{\mathbf{p}}_L^i$ with ${}^{R}\hat{\mathbf{p}}_d$ in Equation (25).

The measurement matrix for the i[th] landmark is

$$ \mathbf{H} = \mathbf{F}_{2\times3}\mathbf{D}_{3\times6}\mathbf{C}_{6\times15} \tag{33} $$

$$
\begin{aligned}
\mathbf{F}_{2\times 3} &= \left.\frac{\partial \mathbf{z}^i}{\partial\, {}^R\mathbf{p}_d}\right|_{{}^R\mathbf{p}_d = {}^R\hat{\mathbf{p}}_d} = \begin{bmatrix} \dfrac{{}^R\mathbf{e}_1 \cdot {}^R\hat{\mathbf{p}}_d}{\left\| {}^R\mathbf{p}_d \right\|_2} & \dfrac{{}^R\mathbf{e}_2 \cdot {}^R\hat{\mathbf{p}}_d}{\left\| {}^R\mathbf{p}_d \right\|_2} & 0 \\ \dfrac{-{}^R\mathbf{e}_2 \cdot {}^R\hat{\mathbf{p}}_d}{\left\| {}^R\mathbf{p}_d \right\|_2^2} & \dfrac{{}^R\mathbf{e}_1 \cdot {}^R\hat{\mathbf{p}}_d}{\left\| {}^R\mathbf{p}_d \right\|_2^2} & 0 \end{bmatrix} \\
\mathbf{D}_{3\times 6} &= \left.\begin{bmatrix} \dfrac{\partial\, {}^R\mathbf{p}_d}{\partial\, {}^R\mathbf{p}_L^i} & \dfrac{\partial\, {}^R\mathbf{p}_d}{\partial\, {}^R\mathbf{v}_L^i} \end{bmatrix}\right|_{{}^R\mathbf{p}_L^i = {}^R\hat{\mathbf{p}}_L^i,\, {}^R\mathbf{v}_L^i = {}^R\hat{\mathbf{v}}_L^i} \\
&= \left(\mathbf{I} - \frac{{}^R\hat{\mathbf{v}}_L^i \;\; {}^R\boldsymbol{\pi}^T}{{}^R\boldsymbol{\pi}^T \, {}^R\hat{\mathbf{v}}_L^i}\right)\begin{bmatrix} \mathbf{I} & -\mathbf{I}\dfrac{{}^R\boldsymbol{\pi} \cdot {}^R\hat{\mathbf{p}}_L^i}{{}^R\boldsymbol{\pi} \cdot {}^R\hat{\mathbf{v}}_L^i} \end{bmatrix} \\
\mathbf{C}_{6\times 15} &= \left.\begin{bmatrix} \dfrac{\partial\, {}^R\mathbf{p}_L^i}{\partial \mathbf{x}} \\ \dfrac{\partial\, {}^R\mathbf{v}_L^i}{\partial \mathbf{x}} \end{bmatrix}\right|_{\mathbf{x}=\hat{\mathbf{x}}} = \begin{bmatrix} -{}^R_G\hat{\mathbf{R}} & \mathbf{0} & {}^R_G\hat{\mathbf{R}}\left\lfloor {}^G\hat{\mathbf{T}}_{Bi}\times \right\rfloor & \mathbf{0} & \mathbf{0} \\ \mathbf{0} & \mathbf{0} & {}^R_G\hat{\mathbf{R}}\left\lfloor {}^G\mathbf{v}_L^i\times \right\rfloor & \mathbf{0} & \mathbf{0} \end{bmatrix},
\end{aligned}
$$

where **I** and **0** matrices in $\mathrm{C}_{6\times 15}$ are 3×3 identity matrix and zero matrix; the vector ${}^G\hat{\mathbf{T}}_{Bi}$ is defined in the same way as in point feature models, and it is also calculated via (28). The detailed derivation of Equation (26) and (33) can be found in Appendix A.

4.2.3.3 Feature Detection

Unlike LiDAR, which needs only a small effective reflective area, the automotive RADAR used in our experiments requires a minimum RADAR Cross Section (RCS) of $0.1\mathrm{m}^2$ at a short distance (≤50m). The RADAR RCS is affected by the RADAR wavelength, object geometry and material composition and angular orientation of the object [97]. Accordingly, RADAR could detect pedestrians within 50 meters. Consequently, there are an abundance of existing objects on real roads that could be detected by the RADAR and be used to aid positioning.

In Figure 4.4, a camera is installed next to the RADAR, which is fixed on a metal plate on roof of the carrier vehicle. Both the camera and RADAR point forward along the

moving direction of the carrier vehicle. Figure 4.4(a) shows the result where road signs, tree trunks, and light poles are clearly detected in the RADAR GUI. The detected objects are very common along real roads. However, when the objects of interest (landmarks) are surrounded by other reflective objects, the RADAR could not reliably determine the exact position of those landmarks. For example, when the light pole is surrounded by tree crowns, the RADAR will return a cloud of points around the pole as in Figure 4.4(b). Further, RADAR does not return detailed characteristics of the target, which also increases the difficulty of target identification and data association. As a result, we found that roadside landmarks need to be of proper size, neither too large that would generate many RADAR detections nor too small that could not be reliably detected by RADAR. Road signs (points) and light poles (lines) are two good landmark examples because they usually have high reflectivity, and are seldom surrounded by clusters of objects. Road signs could be considered as point like features, and light posts could be considered as line features, and more specifically, lines that are perpendicular to the ground plane.

In the experiment, an omnidirectional RADAR reflector is used as a point feature. The reflector is Davis Instruments Echomaster™ RADAR reflector [98]. It is composed of three orthogonal round aluminum planes whose diameter is 11.5 inch. The planes form a total of 8 corner reflectors. The orthogonal planes could reflect RADAR beams from all directions back on the exactly opposite direction.

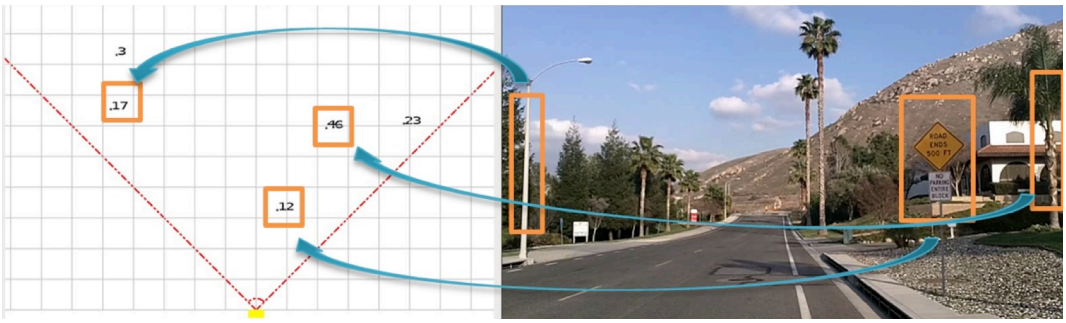

(a)

(b)

Figure 4.4 (a) shows what Radar detects on a cluster of objects. The tree crowns return too many objects that are close to each other, which makes the identification of single object very difficult. (b) shows some existing objects on real roads that are good as landmarks, including road signs, tree trunks and light poles.

Figure 4.3 Davis Instruments Echomaster™ Radar reflector. Three perpendicular aluminum plane forms 8 corner reflectors.

4.2.3.4 Feature Association

The purpose of feature association is to build up the optimal correspondence between RADAR measurement and the features with known position. For many sensors that could provide additional information about the feature besides position, data association problem could be relatively simple. For example, in camera images, feature shape, color, texture, etc. could be used to identify objects [37]; in LED based navigation, the ID of the LED could be transmitted to the receiver by blinking at certain coding [36]. However, the RADAR feature association problem is more difficult, because the automotive RADAR detection provides no additional information than relative sensor frame position to distinguish and identify its detections. For example, in Figure 4.4, all RADAR detections are identically perceived as a point disregarding the size, shape or reflectivity.

Known mapped feature positions and direction vectors are stored in a database (for the simple experiment in this dissertation, they are stored in a list), which are projected onto RADAR coordinate frame using Equation (24) and (32). Those features that are out-of-sight of RADAR FOV and detectable range are filtered out. This estimation could reduce unnecessary computational cost.

After the initial filtering, the landmark features that are potentially detectable by the RADAR are matched with detections using the Mahalanobis Distance gating algorithm [99]. Intuitively, the detection that is closest to the projected feature position should be associated with it. However, the Euclidean distance ignores the special probability distribution of measurements. When features are projected into RADAR

coordinate frame, their position covariance is also estimated. According to the EKF algorithm, the position is assumed to be a Gaussian distribution whose mean is the projected position, and the covariance **S** is calculated from Equation (16).

At any time instant t_k, the i[th] predicted landmark position in RADAR frame is denoted as $\hat{\mathbf{z}}_k^{Li}$, and the corresponding covariance matrix is denoted as $\mathbf{S_{ki}}$. The j[th] detection reported from RADAR is denoted as $\tilde{\mathbf{z}}_k^{Mj}$. The Mahalanobis distance is defined as

$$d_m^{ij} = \left\| \tilde{\mathbf{z}}_k^{Mj} - \hat{\mathbf{z}}_k^{Li} \right\|_m = \sqrt{\delta \mathbf{z}_k^{ij^T} \mathbf{S}_{ki}^{-1} \delta \mathbf{z}_k^{ij}} \tag{34}$$

where $\delta \mathbf{z}_k^{ij}$ is the residue between $\tilde{\mathbf{z}}_k^{Mj}$ and $\hat{\mathbf{z}}_k^{Li}$ and is calculated using $\delta \mathbf{z}_k^{ij} = \tilde{\mathbf{z}}_k^{Mj} - \hat{\mathbf{z}}_k^{Li}$. The Mahalanobis distance of each potential match $\left(L_i, M_j\right)$ is calculated. Two criterions are defined to validate the match.

1. The squared Mahalanobis distance is smaller than a threshold γ.
2. For each landmark, only one RADAR detection satisfies the first criterion.

The threshold γ defines a gating area $\{\mathbf{z}: d^2 \leq \gamma\}$. Based on the Gaussian distribution assumption, the squared Mahalanobis distance follows χ^2-distribution with 2 degree of freedom [100]. The threshold is chosen using inverse cumulative χ^2-distribution such that the probability that the feature detection falls into the gating area is 0.99. There is one problem with this simple gating method. When multiple detections fall into the gating area, the correct match may not necessarily be the one with smallest Mahalanobis distance. This is especially true when detections are dense in small areas. If a false match was considered to be the correct one, the false residue would be introduced into the EKF

system, and due to the Bayesian estimation characteristic, the error will affect all the state estimation accuracy after it is introduced. So in this dissertation, we reject those features for witch multiple detections exist in the gating areas. Besides, we choose features that are isolated from other RADAR detectable objects to reduce this problem.

More sophisticated methods that take into account the joint probability of multiple features at once can be found in [101]. This is useful when multiple features could be detected at once. The relative position of multiple features could be considered a constraint to eliminate some false association. By using these methods, it may not be necessary to use the second criterion described above, and thus features could be utilized more efficiently. On the other hands, all these methods require additional computer resources. It would be a good future area to explore to determine the best data association method for automotive RADAR measurements.

4.3 Experiments

This section presents the experiments that are designed to validate the concepts and algorithms presented above. The platform in Figure 3.1 is mounted rigidly on top of the test vehicle. The IMU sensor used on that platform is a MEM's device that provides measurements at 200Hz. The Delphi RADAR has its internal filtering and tracking programs disabled to provide raw range and angle measurements. The RADAR has 90º horizontal Field-Of-View (FOV), and 4º vertical FOV. The RADAR could report at most 64 detections at 20Hz, but we use the measurement to update EKF estimates at 1Hz.

The claimed accuracy is 0.1m of range measurement and 0.3º, but according to our test, we set the standard deviation of range measurement noise as 0.2m and angle measurement noise as 0.6º based on the statistics from field tests. The GPS receiver in the experiments could provide both pseudorange, Doppler and carrier-phase measurements. The carrier-phase aided INS system calculates the vehicle's trajectory with an accuracy better than 10 centimeters [102], so its position estimates are used as ground truth to verify the proposed system positioning accuracy. In our system, the carrier-phase measurements could be disabled leaving only Doppler and pseudorange measurements to aid INS to mimic the typical DGPS/INS positioning system. Such a system is used for comparison to prove the accuracy improvement with RADAR aiding. The positioning algorithm is implemented on a computer with an Intel Core 2 Duo P8600 using POSIX multithreading architecture, such that the calculation of any single sensor data would not cause delay to other sensors and IMU integrations. In the experiment, all raw sensor measurements including IMU, GPS and RADAR are logged with the corresponding time-tags, such that the raw data can be reprocessed off-line by different estimation algorithms. In this way, the performance of aiding algorithms could be compared.

In the following sections, two parking lot experiments are presented to validate the point feature and pole feature aided DGPS/INS system respectively. In a typical roadway environment, the features are along the roadside. So in the experiments, the vehicle will drive towards the landmarks and pass it to mimic the real world scenario.

4.3.1 Point Feature

In this experiment, the omnidirectional RADAR reflector demonstrated in Figure 4.3 is mounted on a very thin tripod, and placed in an empty parking lot as a point feature. The center of the reflector is surveyed via Trimble 5700 differential GPS with an accuracy of less than 3cm. The surveyed position is

$$^{G}\mathbf{p}_{L}^{0} = [2826.302 \quad -994.854 \quad 60.245]^{T}.$$

At startup when the vehicle is stationary, the position and velocity of the vehicle

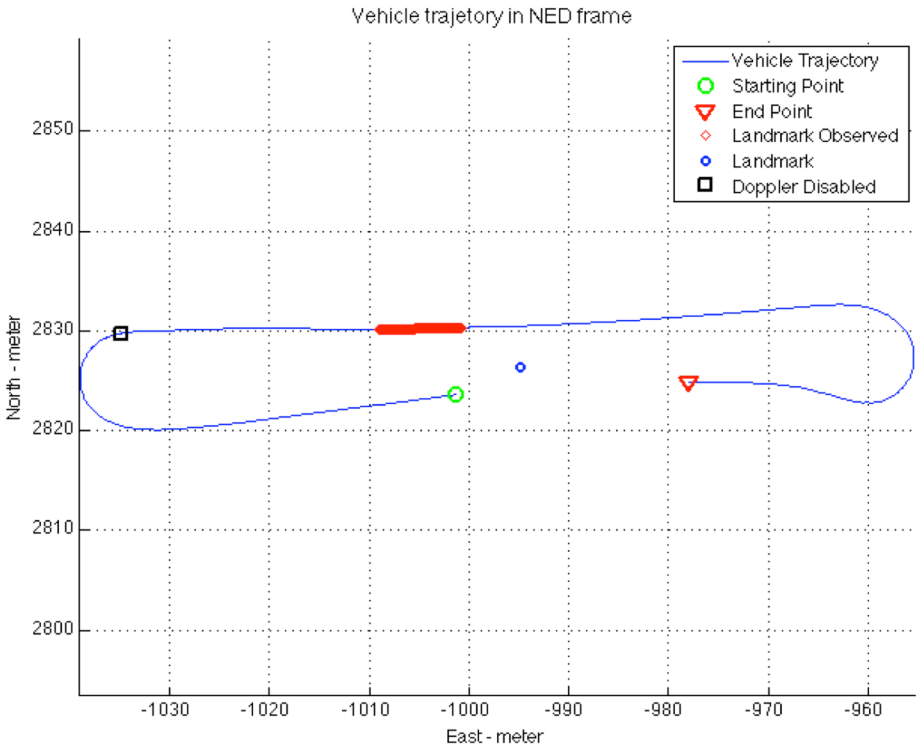

Figure 4.5 Vehicle trajectory in NED frame is estimated with CPGPS/INS system.

is directly observable via GPS measurements. The yaw angle is unobservable while stationary, but will become observable and be initialized when the vehicle starts moving.

The roll and pitch are initialized using average IMU measurements and the direction of the gravity vector according to Section 10.3 in [6]. When the vehicle starts maneuvering, the attitude and IMU bias errors become observable and calibrated by EKF.

The north and east coordinates of the vehicles trajectory in local tangent frame is demonstrated in Figure 4.5. When the vehicle starts up heading west, the pseudorange, Doppler and RADAR aiding are all enabled. When the yaw is estimated to subdegree level, the Doppler aiding is turned off at about 30s. The vehicle then drives towards the reflector. The RADAR aiding is involved while the data association is successful from 113.8s to 126.5s, which is the red portion in Figure 4.5. The reflector is on the right side of the vehicle trajectory to mimic the typical position of a roadside landmark.

The RADAR measurement residues are demonstrated in Figure 4.6. The residue is only available when data association is carried out, so that the plots show the residues from 113.8s to 126.5s. In the residue plots without RADAR aiding, the residue standard deviation decreases at integer seconds, because GPS measurements updates happened at 1Hz that corrects accumulated IMU error within the second. In the residue plots with RADAR aiding, the standard deviation change happens when RADAR measurement updates the EKF estimate. As is mentioned above, the RADAR measurement occurs at 20Hz, but only update the state vector at 1Hz, and in the program, the RADAR measurement update is chosen to happen at 0.7s after each GPS 1pps signal. What is worth noticing is that, the RADAR measurement is much more accurate than GPS aiding measurements, so that the GPS pseudorange measurements have little improvement on the standard deviation. The state error increases within each second due to integrated

effects of IMU noises and biases For the DGPS/INS system, this error decreases at integer second when GPS updates the system, while in RADAR aided DGPS/INS system, the state error decrease mostly happen when RADAR measurement updates the states.

In the position error comparison, it can be seen that both North coordinate and East coordinate errors drastically decreases when RADAR aiding is available, while Down coordinate receiver no improvement. This is because the RADAR FOV plane is approximately parallel to the North-East plane, and the RADAR measures the 2D relative position of landmark and RADAR itself. This fact makes the North and East position observable when RADAR measurements are integrated, and thus reduces the North and East positioning error. The Down position is unobservable, such that it receives no improvements. The standard deviation comparison also shows the same effect. Both North and East position standard deviation are bounded to be smaller than 0.3m, while the Down position standard deviations in both systems are almost the same. Luckily, the lane-level accuracy requirements does not pose strict accuracy requirements for down coordinates, so the results proves that the proposed system could satisfy the lane-level accuracy requirement.

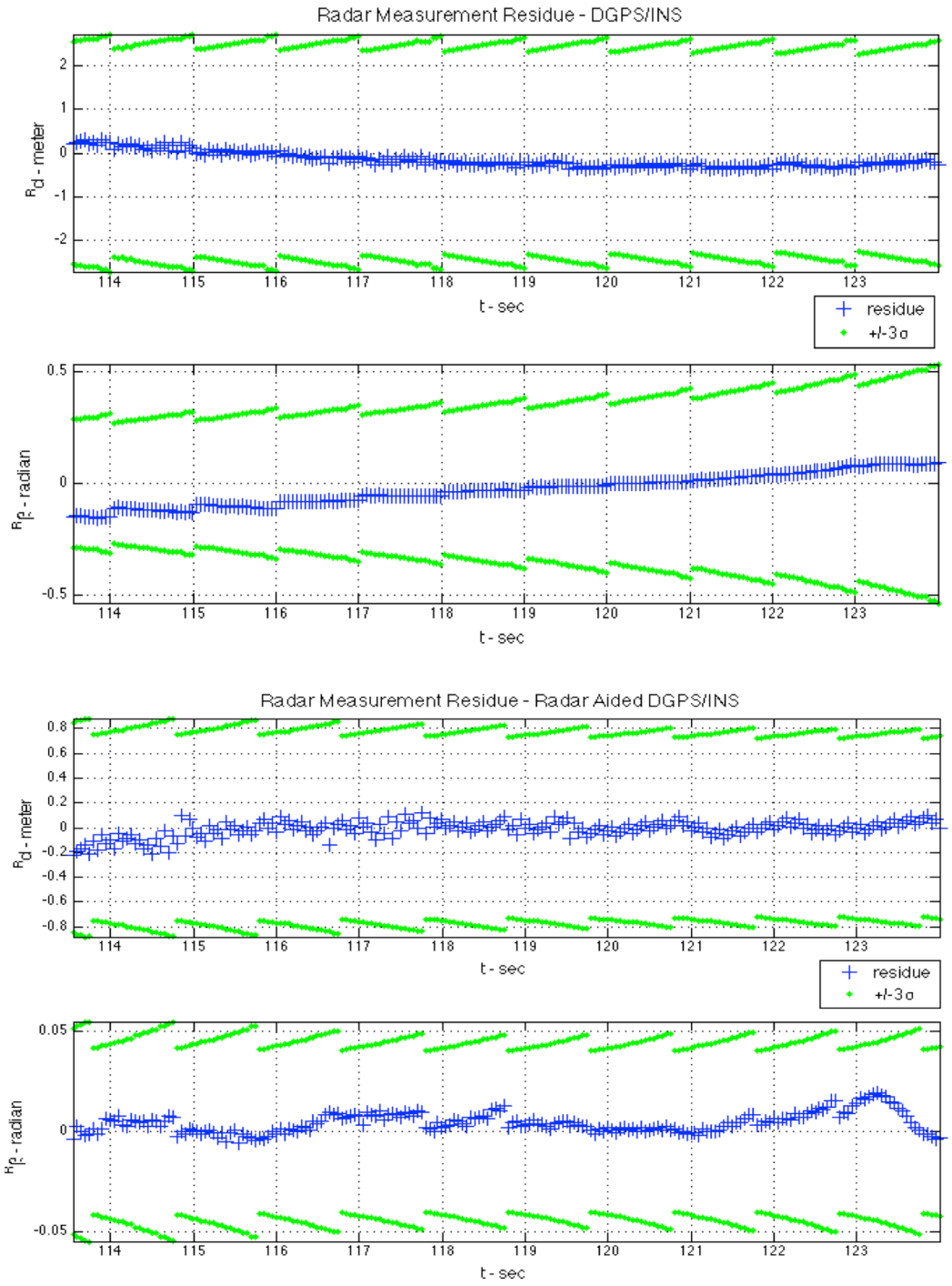

Figure 4.6 The comparison of Radar measurement residues without and with Radar aiding shows significant decrease of residue amount, and decrease of predicted residue standard deviation.

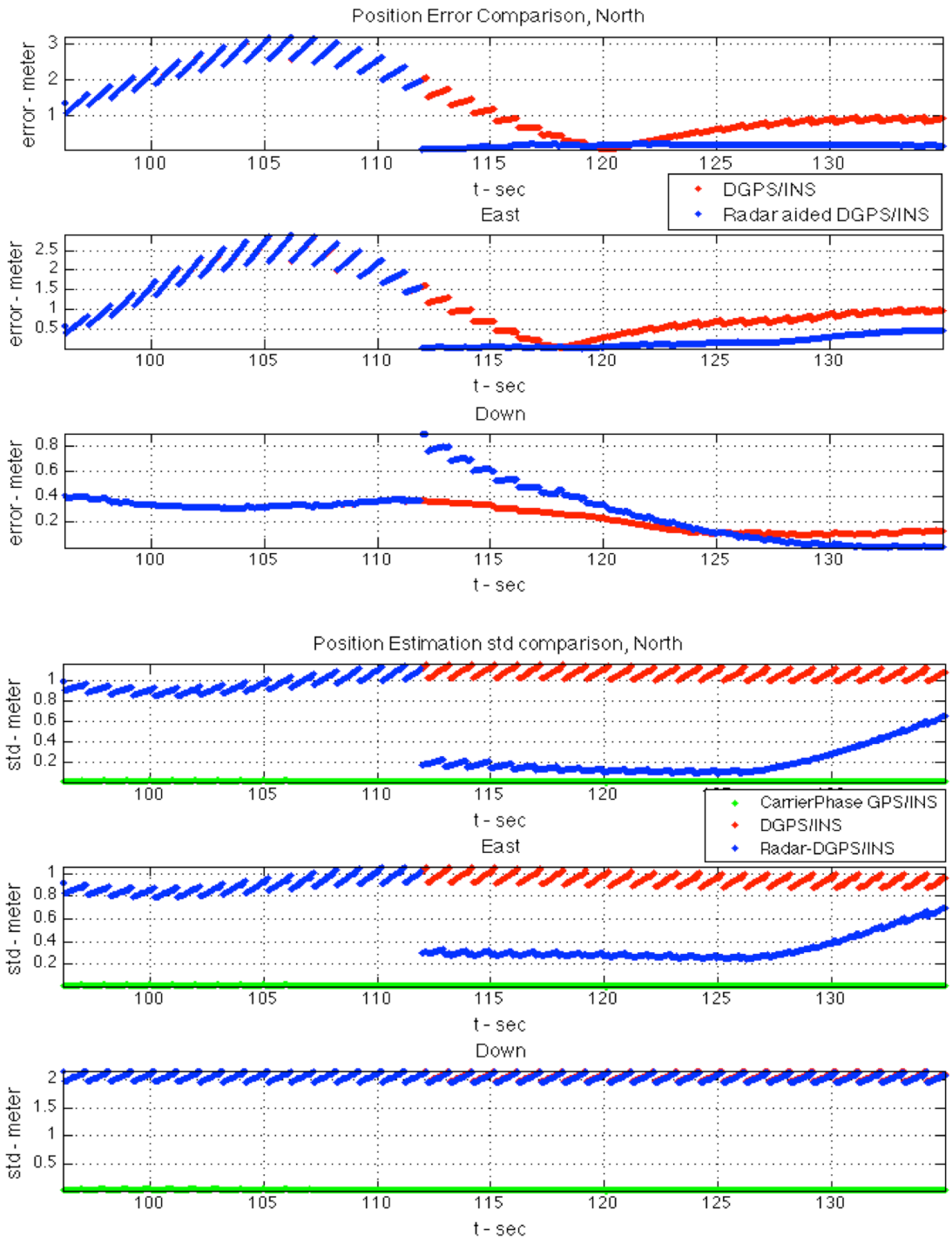

Figure 4.7 The use of Radar aiding effectively reduces the position error in North and East direction, and also improves the confidence level of the accuracy of the positioning estimation in North and East direction.

4.3.2 Vertical Line Feature

The experiment using vertical line feature is also carried out on the same parking lot. A metal light pole is surveyed and used as the vertical line feature. The point on the line feature and the direction vector are

$$
\begin{aligned}
{}^{G}\mathbf{p}_{L}^{i} &= [2802.922 \quad -994.965 \quad 60.245]^{T} \\
{}^{G}\mathbf{v}_{L}^{i} &= [0 \quad 0 \quad 1]^{T}
\end{aligned}
$$

In this experiment, the vehicle starts by driving north, then make a left turn. When the yaw is estimated to subdegree level, the Doppler measurement is disabled at the black square in Figure 4.8. The RADAR aiding is always enabled, but only effective when the

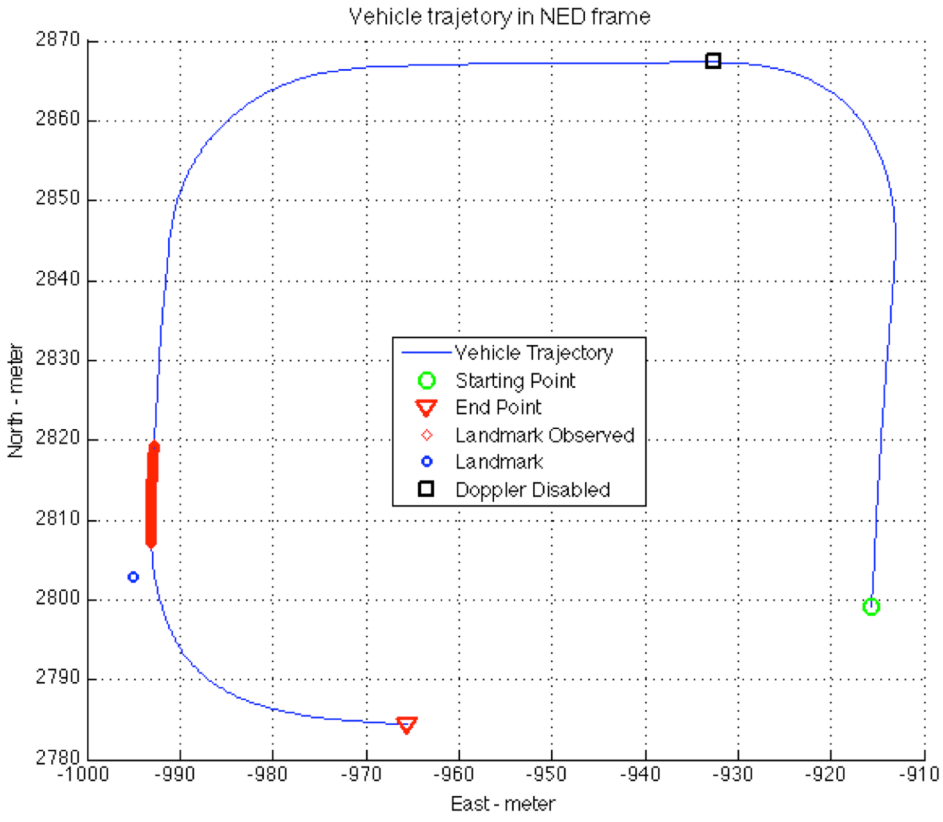

Figure 4.8 Vehicle trajectory in NED frame is estimated with CPGPS/INS system.

pole feature is detectable and data association is successful. The effective region is also colored in red from around 51s to 65s.

The residue plot shows similar results as those in point feature aided positioning. When the RADAR aiding is disabled, GPS pseudorange alone causes significant positioning error. From 60.3s to 65s, the range measurement residues failed the Mahalanobis test, so that no more residues can be plotted. In comparison, when RADAR aiding is enabled, accurate estimate can be maintained, so that the data association test are successful all the time. In the position error comparison plot, the results also shows error decrease in both North and East direction, so are the standard deviations. Though the down coordinate error is reduced, but the standard deviation remains roughly the same, which also results from the fact that Down position is unobservable with the 2D RADAR measurements. The standard deviations for both North and East positions are less than 0.3m, which also satisfies the lane-level accuracy.

4.4 Summary

This Chapter presents the tightly-coupled automotive RADAR aided DGPS/INS system. Two types of RADAR features are selected and modeled separately. The EKF update models are created, and tested through experiments. With properly surveyed RADAR features, the RADAR aided DGPS/INS system could reach lane-level accuracy.

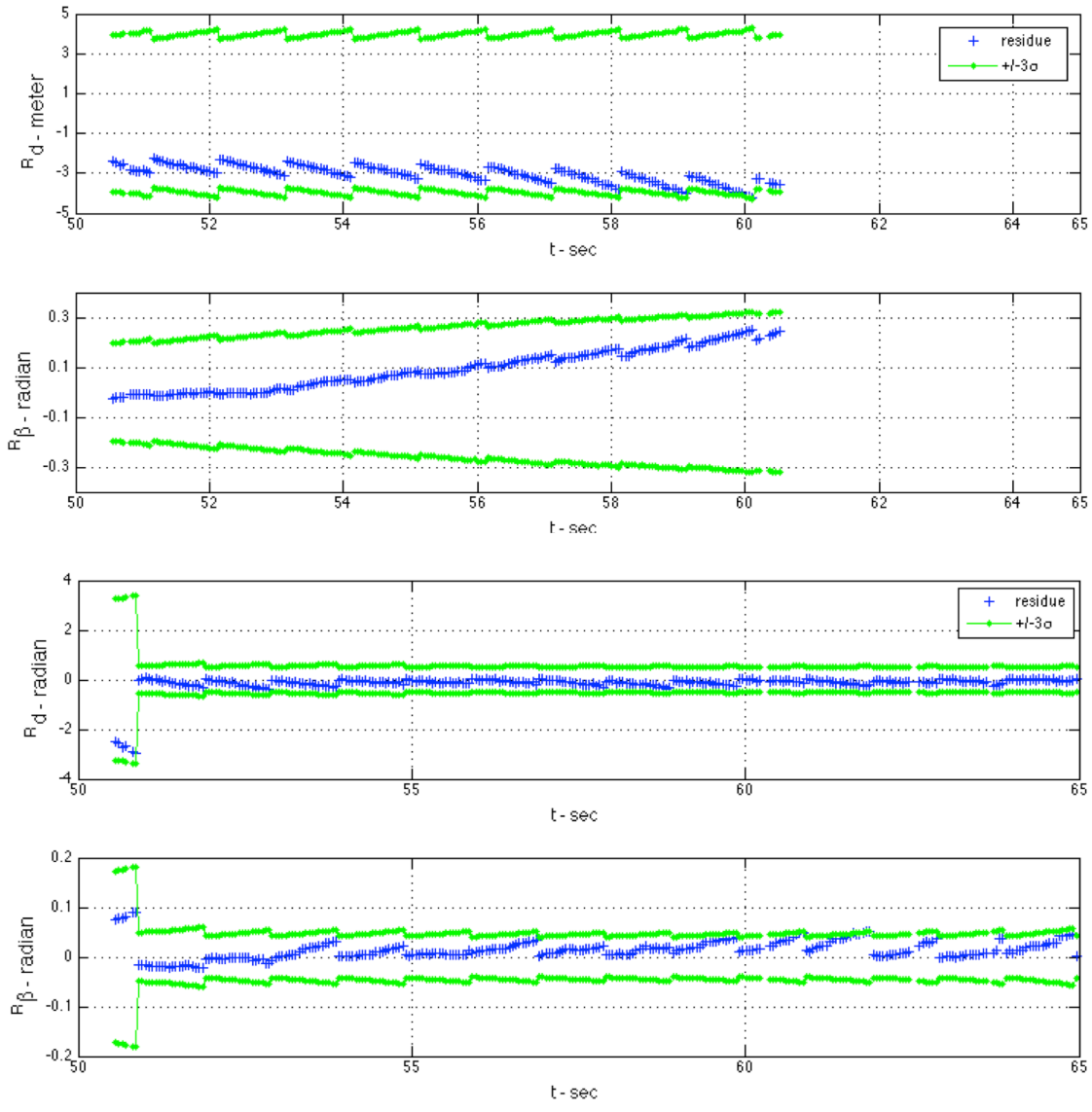

Figure 4.9 Range and angle measurement residues of DGPS/INS system are compared with those of Radar aided DGPS/INS system.

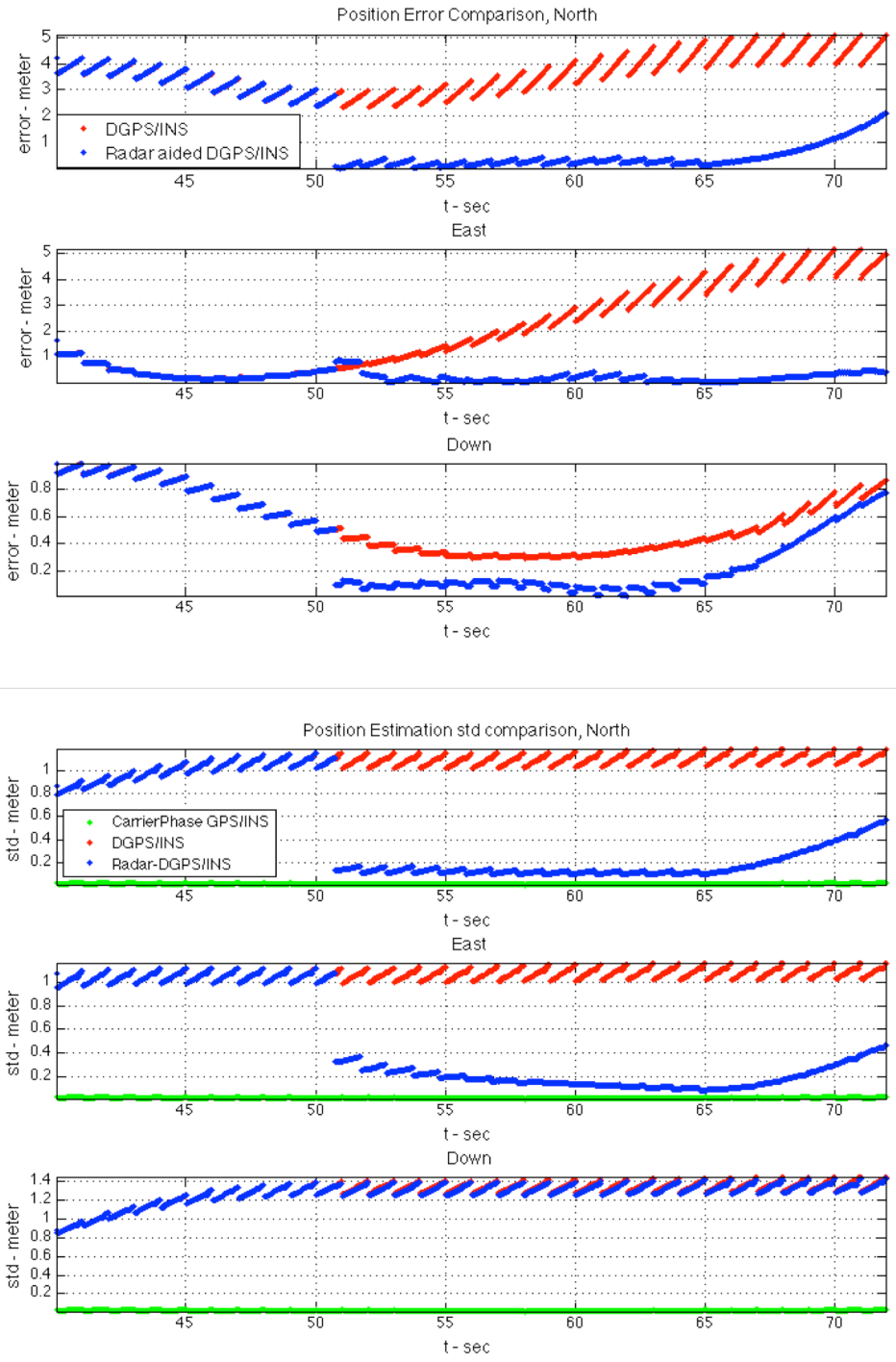

Figure 4.10 The position error and standard deviation comparison with and without Radar aiding. The results proves the effectiveness of vertical line feature measurement model.

Chapter 5 Road Feature Mapping with Mobile Mapping Platform

5.1 Introduction

Currently, popular digital maps have limited accuracy and inadequate road features which are the prerequisites for Advanced Driver Assistance Systems (ADAS), Vehicle Assist and Automation (VAA) systems, and many more ITS applications that have emerged in the past few years. The vehicle needs to estimate its accurate position, and find itself on an accurate map, before it could determine its location in lane as in lane departure warning systems. Accurate location of intersection road features are required to estimate the precise arrival time to intersections which is the fundamental information in Intelligent Intersection Control systems and Eco-Speed Recommendation Systems [103].

This chapter presents a general framework of Mobile Mapping System, including the data collection and storage, accurate vehicle trajectory estimation, local point cloud generation and feature extraction. The offline trajectory optimization based on *smoothing* is briefly described. After the general description, we will focus on the extraction on intersection stop-bars. A robust extraction and estimation algorithm based on image processing is presented later. Intermediate results are also presented in each section.

In the following sections, the results are based on a dataset surveyed on El Camino Real from (37.380535N, 122.073444W) to (37.429970N, -122.151744W) near Mountain View and Palo Alto in California. It is a 5.6 miles road section, which contains more than 30 well-structured intersections. We drove the Altima with the terrestrial

mobile mapping system described in Chapter 3 on the test field once on each direction. The data collection was carried out in the mid-night to prevent the traffic, which could seriously block LiDAR beams. Pseudorange, Doppler and carrier-phase measurements and the 1 pulse per second (1PPS) time from the dual frequency GPS receiver, Velodyne LiDAR data as well as 200Hz IMU measurements were logged using a uniform time reference. The differential GPS correction messages came from the nearby RTCM Ntrip station and were also logged using the same time reference.

5.2 Offline Processing System Overview

The logged raw data are processed using three major blocks as shown in Figure 5.1.Raw GPS, IMU, LiDAR and/or Camera measurements are input to the offline processing system. The data preparation block is the common step for all road feature extraction algorithms. In this block, the vehicle trajectory is estimated by smoothing the whole log of GPS and IMU measurements. Then the raw LiDAR data are calibrated with the factory parameters, filtered by distance, converted to global coordinate frame using the optimized vehicle trajectory and extrinsic parameters with respect to IMU. Finally, the time-series of LiDAR point clouds are stored into 151m by 151m blocks based on the North and East coordinates. The second block generates the bird's eye view intensity image of selected intersection regions and then enhances the intensity image using Morphological operations. In the third block, image processing algorithms are utilized on the intensity image to extract the stop bars as straight lines and then find the ends of each stop bar.

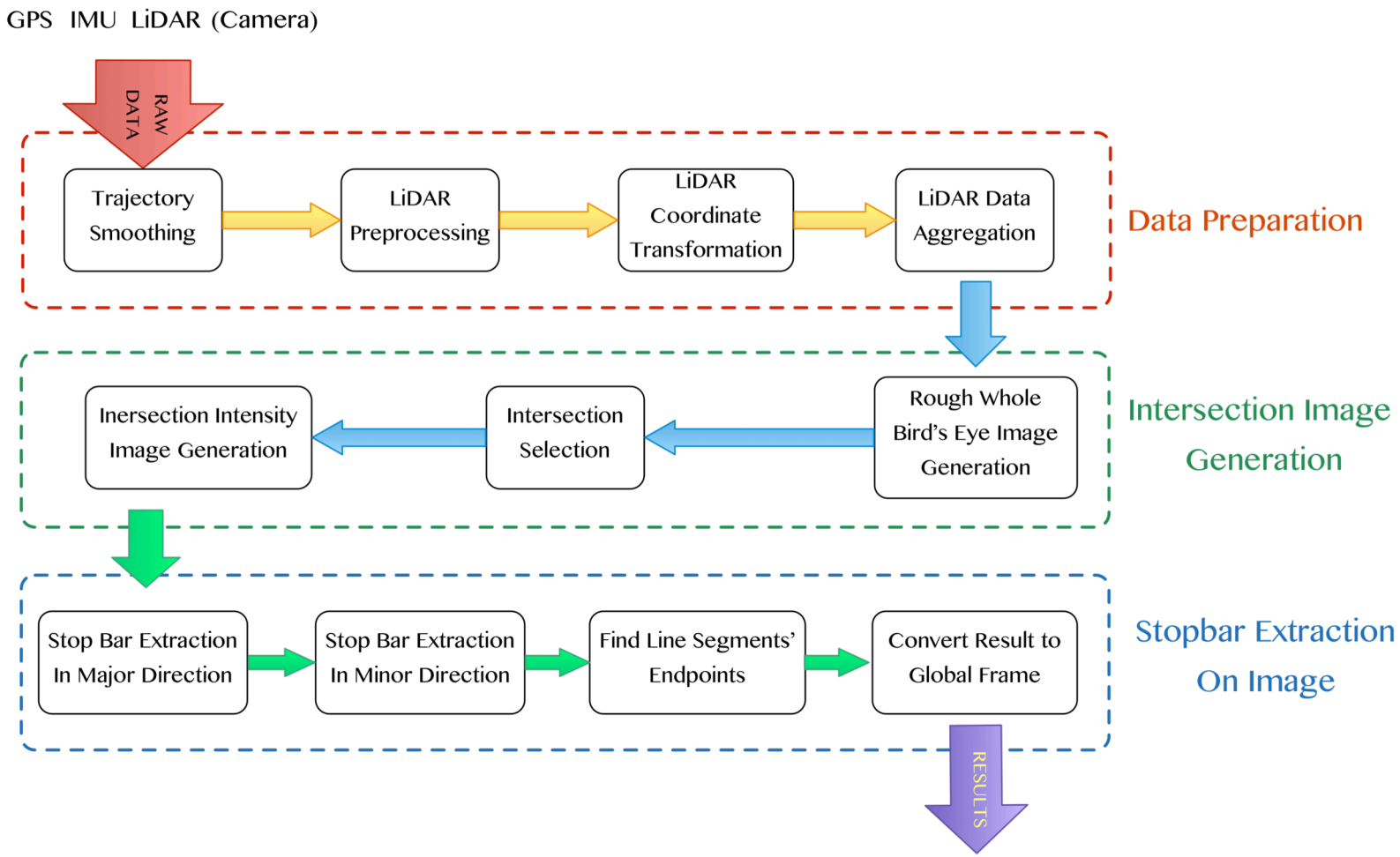

Figure 5.1 Data processing flow chart of our LiDAR based Mobile Mapping System.

5.3 Data Preparation

5.3.1 Vehicle Trajectory Smoothing

The first fundamental step for all mobile mapping systems is the acquisition of an accurate mobile platform trajectory. Most commercial systems rely on a real time positioning solution by integrating GPS with IMU or Dead Reckoning using EKF, similar to the system described in Chapter 4. Post processing kinematic solutions (PPK) of GPS post processing could provide most accurate positioning accuracy in the popular MMS systems. Besides, commercial systems also utilize expensive IMUs for most accurate positioning.

The nature of the mapping problem does not require real time positioning solutions, such that offline post processing which may take more computation time is also viable. *Smoothing* is a non-causal operation on the data using past, present and future measurements to estimate the platform pose at each time. Compared to *Filtering* which only uses past and present measurement to estimate the present pose, Smoothing in nature has lower levels of uncertainty and greater accuracy. In this Chapter, a Smoothing And Mapping (SAM) algorithm from [104] is briefly described. It is an extension to the Square Root Smoothing and Mapping [105].

In this algorithm, the raw dual-frequency GPS measurements that includes pseudorange, Doppler and carrier phase and raw 6-DOF IMU measurements are used as input. The mathematical model of GPS and IMU measurements are the same as those described in Section 4.2.3.1 and 4.2.2.5. The system kinematic model and error model are also described in Section 4.2.2. The state of the system at each time step is defined in

Equation (8). The smoothing algorithm optimizes the trajectory over the entire driving period. The states, IMU measurements (as input) and GPS measurements (as observation) of the entire period is

$$\mathbf{x}_{1:M} = [\mathbf{x}_1^T \quad \mathbf{x}_2^T \quad \cdots \quad \mathbf{x}_M^T]$$

$$\mathbf{u}_{1:M} = [\mathbf{u}_1^T \quad \mathbf{u}_2^T \quad \cdots \quad \mathbf{u}_M^T]$$

$$\mathbf{z}_{1:M} = [\mathbf{z}_1^T \quad \mathbf{z}_2^T \quad \cdots \quad \mathbf{z}_M^T].$$

The joint probability of $\mathbf{x}_{1:M}$ and $\mathbf{z}_{1:M}$ can be defined based on total probability rule as

$$P(\mathbf{x}_{1:M}, \mathbf{z}_{1:M}) = P(\mathbf{x}_0) \prod_{i=1}^{M} P(\mathbf{x}_\mathrm{i} | \mathbf{x}_{\mathrm{i}-1}, \mathbf{u}_{\mathrm{i}-1}) \prod_{i=1}^{M} P(\mathbf{z}_\mathrm{i} | \mathbf{x}_\mathrm{i}),$$

where $P(\mathbf{x}_0)$ is a priori on the initial state, $P(\mathbf{x}_\mathrm{i} | \mathbf{x}_{\mathrm{i}-1}, \mathbf{u}_{\mathrm{i}-1})$ is the vehicle kinematic and mechanization model in probability form, and $P(\mathbf{z}_\mathrm{i} | \mathbf{x}_\mathrm{i})$ is the GPS measurement model in probability form. According to Bayes' rule,

$$P(\mathbf{x}_{1:M} | \mathbf{z}_{1:M}) = \frac{P(\mathbf{x}_{1:M}, \mathbf{z}_{1:M})}{P(\mathbf{z}_{1:M})}.$$

The denominator is irrelevant to $\mathbf{x}_{1:M}$, such that the maximum likelihood estimate is

$$\hat{\mathbf{x}}_{1:M} = \arg\max_{\mathbf{x}} \prod_{i=1}^{M} P(\mathbf{x}_\mathrm{i} | \mathbf{x}_{\mathrm{i}-1}, \mathbf{u}_{\mathrm{i}-1}) \prod_{i=1}^{M} P(\mathbf{z}_\mathrm{i} | \mathbf{x}_\mathrm{i}).$$

Given the assumption that state and observation noises follow Gaussian process, and working with log-likelihood, the maximum likelihood estimate can be transformed to

$$\hat{\mathbf{x}}_{1:M} = \arg\min_{\mathbf{x}} \sum_{i=1}^{M} \left(\|\mathbf{x}_\mathrm{i} - \boldsymbol{\Phi}(\mathbf{x}_{\mathrm{i}-1}, \mathbf{u}_{\mathrm{i}-1})\|_{\boldsymbol{Q}_d}^2 + \|\tilde{\mathbf{z}}_\mathrm{i} - \mathbf{h}(\mathbf{x}_\mathrm{i})\|_{\boldsymbol{R}_k}^2 \right).$$

It becomes a nonlinear least square problem and could be solved with numerical method. The detailed solution to this problem, and the solution of integer ambiguity to GPS carrier phase measurements can be found in [104].

5.3.2 LiDAR Preprocessing

The raw LiDAR measurement of the ith of the 64 lasers is $[R_i \quad \delta_i \quad \varepsilon \quad int]^T$, which represents the raw distance, the angle of the ith laser with respect to LiDAR's x-y plane, the rotation angle of the whole LiDAR housing and finally the intensity. The ideal transformation of the raw LiDAR measurement to the 3D coordinate in LiDAR coordinate frame is defined as Equation (1). In practice, the 64 laser emitter and receivers are not aligned in a vertical line, so that several calibration parameters are involved in the actual transformation.

1. Horizontal rotation correction is the offset of the actual rotation angle of the ith laser from the whole LiDAR housing's rotation angle.
2. Vertical rotation correction is the offset of the actual vertical angle of the ith laser from the nominal vertical angle δ_i.
3. Horizontal offset is the offset of laser measurement origin from z-axis in the x-y plane.
4. Vertical offset is the offset of laser measurement origin from x-y plane in z direction.
5. Distance offset is the bias of the ith laser's raw distance measurement.

In the LiDAR preprocessing block, the raw LiDAR measurements are converted to 3D Cartesian coordinates with the calibration parameters and methods provided by the

manufacturer. Before the transformation, a simple distance filter is applied to remove detections that are closer than 1m or farther than 75m from the LiDAR. The 3D coordinates are then passed into the next block to be transformed to global coordinate frames.

5.3.3 LiDAR Coordinate Transformation

The LiDAR points in LiDAR coordinate frame are stored as a list with the time reference when the laser point detection took place. To convert the LiDAR measurement to global coordinate frame, we need to find the corresponding vehicle pose of the specific laser detection. The pose is obtained by interpolation of the two states in the smoothed trajectory whose times are closest to the given LiDAR time step. The extrinsic calibration parameters between LiDAR and body frame are denoted as the translation vector ${}^{\boldsymbol{B}}\mathbf{T}_{LB}$ and rotation matrix ${}^{\boldsymbol{B}}_{\boldsymbol{L}}\mathbf{R}$. The transformation equation is

$$ {}^{G}\mathbf{p}_L^k = {}^{L}_{B}\mathbf{R}\left({}^{B}_{G}\mathbf{R}^{i_k}\left({}^{L}\mathbf{p}_L^k - {}^{G}\mathbf{p}_B^{i_k}\right) + {}^{B}\mathbf{T}_{LB}\right), \tag{35} $$

where ${}^{L}\mathbf{p}_L^k$ is the position of kth LiDAR detection in LiDAR frame, ${}^{G}\mathbf{p}_B^{i_k}$ is the position of the body frame at the time step of the kth LiDAR detection and ${}^{B}_{G}\mathbf{R}^{i_k}$ is the rotation matrix that represents body frame's attitude.

The preprocessed data of the entire run is around 4 gigabytes, which hardly fits the computer memory. It is partitioned to pieces of 40 megabytes which contains 1000 cycles. Each partition is converted to global frame separately, and then passed into the next block.

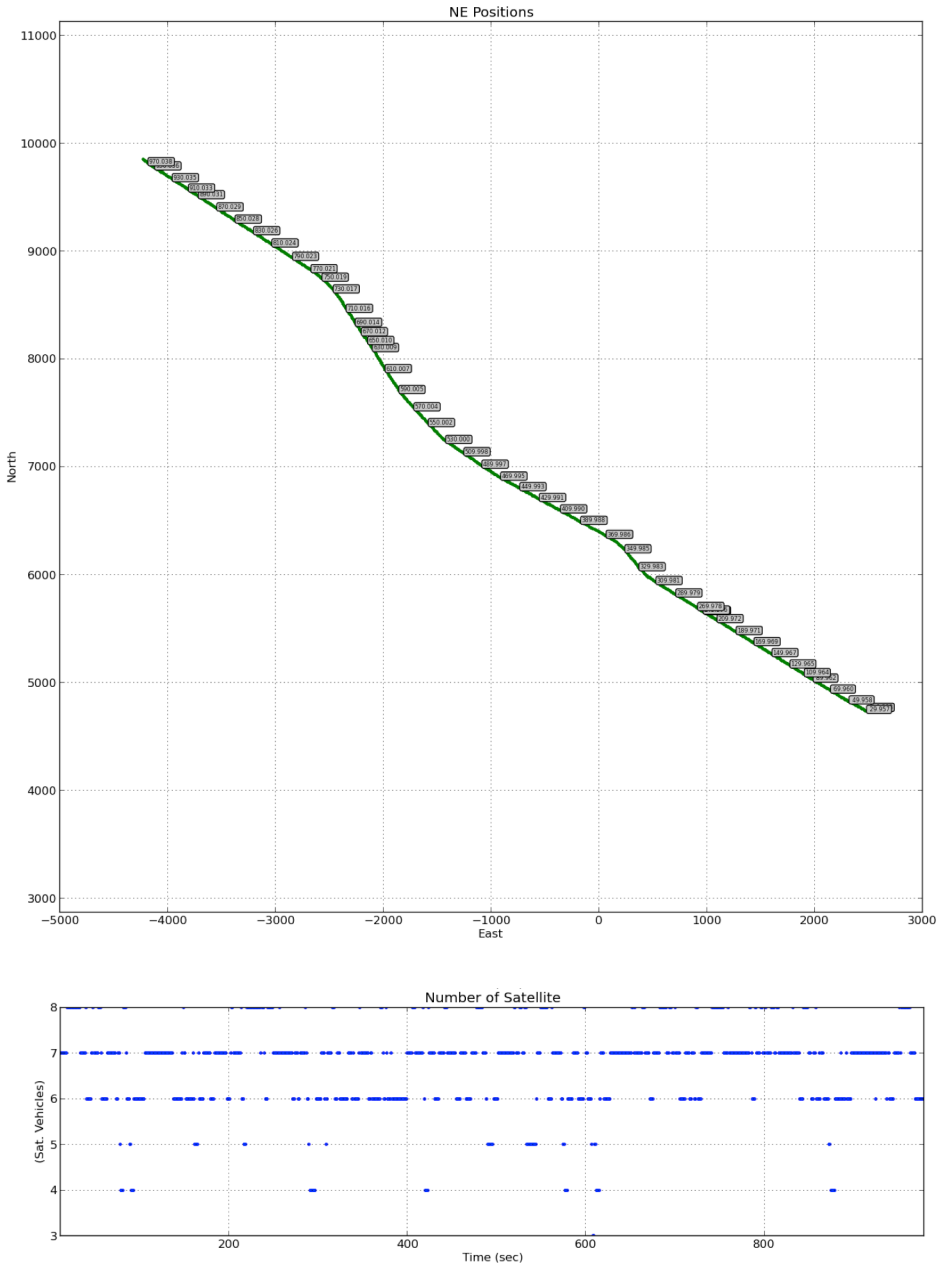

Figure 5.2 The first plot (a) is the plot of the estimated north and east coordinates of the trajectory. The second plot (b) is the number of satellites above predefined elevation.

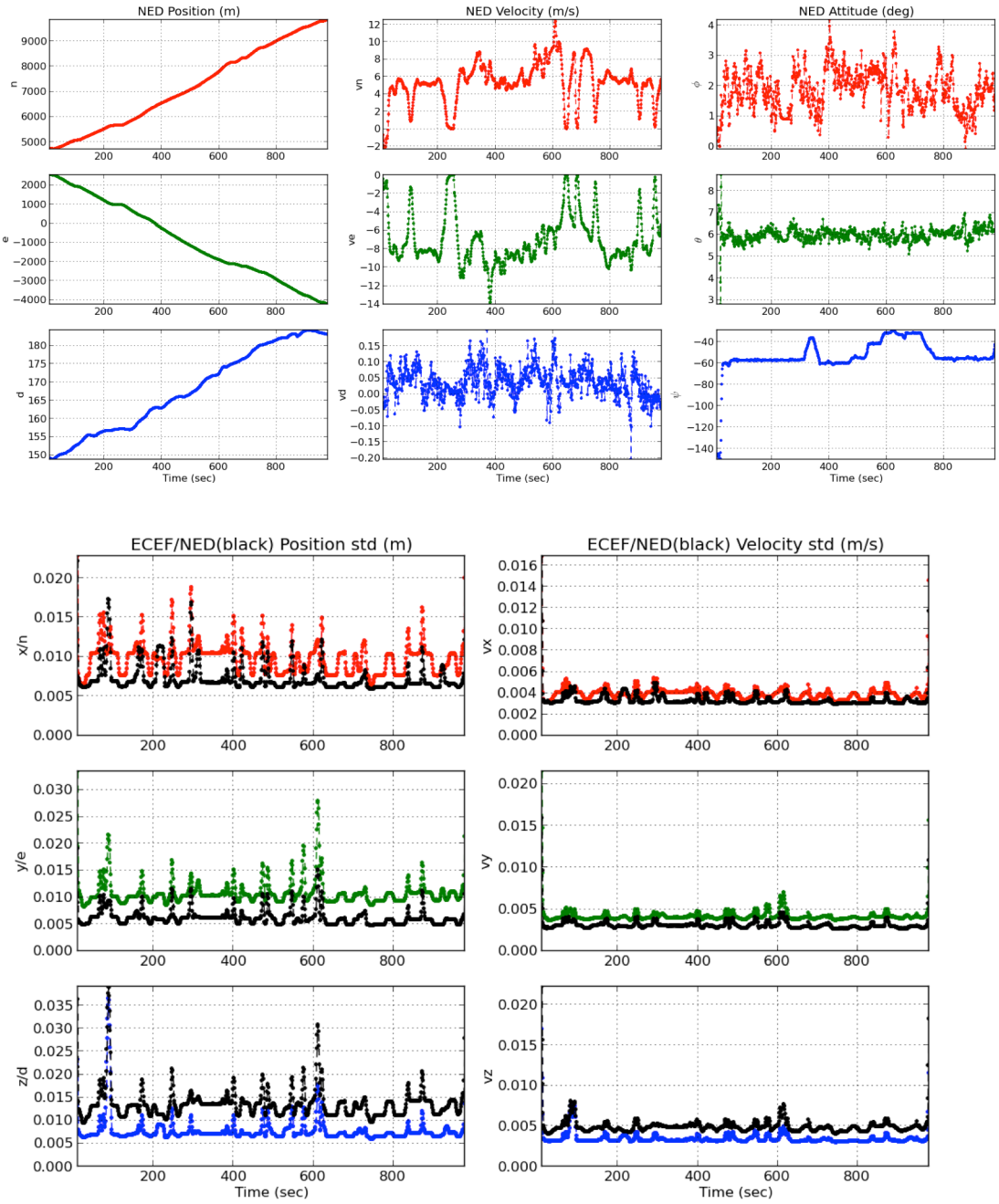

Figure 5.3 The first three rows are the smoothing results of the position, velocity and attitude in NED frame. The bottom three rows show the standard deviations of the position and velocity estimates. In general, the overall positioning standard deviation is below 2cm. If we refer to Figure 5.2(b), it can be seen that the large position standard deviation happens when the number usable satellites are low.

5.3.4 LiDAR Data Aggregation

The LiDAR data in global frame from the previous block need to be stored into database or simply data files on hard drive, because different applications could implement different algorithms on these preprocessed data. Instead of using the whole trajectory of LiDAR data, the feature extraction algorithms usually process only small sections of data to fit the limited memory. The simple way of storing all LiDAR data into a single file has several disadvantages. Firstly, the file would be too large in size due to the large amount of LiDAR data, so that it could not easily be loaded into memory, and it also takes too long. Secondly, obtaining specific LiDAR point requires traversing the whole file, which requires unnecessary time cost. So a distributed storage architecture is designed and implemented in our system.

To support the following procedures which extract the intersection region, the LiDAR data is stored into several non-overlapping blocks of data files. Each block contains all the LiDAR points that falls into the north and east boundaries of the block. In our system, each block is a box with infinite length along down-axis. The box covers 151m by 151m region in North-East plane. The size of the box is selected such that the LiDAR points from each LiDAR scan cycle (full 360°) would fall into at most four such blocks in the worst scenario to make reduce the memory usage. The index of each block is the coordinate of its North and East corner.

The LiDAR points in the block can be simply stored as plane list. If the processing algorithms are based on 3D point cloud algorithms, the unstructured list is enough. In our algorithm, the next step requires the creation of a 2D bird's eye view of

intersection, so a matrix like structure is selected. The 151m by 151m block is partitioned into 10cm by 10cm cells in North-East plane. Each cell stores a list of LiDAR points within the NE region.

5.4 Intersection Image Generation

5.4.1 Full Bird's Eye View Image

In this study, the intersection area is selected by clicking mouse on the full image. So this section describes the method to create the full bird's eye image.

After LiDAR data aggregation and storage, a 2D intensity image in bird's eye view of the complete trajectory is built. In the previous step, the NED coordinate of each LiDAR point is stored in the block file. According to the definition of a local tangent frame, the origin of the local tangent frame is close to the test field. In this case, the North-East plane could be a rough approximation of the actual earth surface.

The full image is created by merging images of each block file. The single image of each block file contains 1510 by 1510 pixels. In this step, the intensity of each pixel is the average intensity of all LiDAR points that falls into the corresponding 10cm by 10cm cells. The intensity of LiDAR detection is in the range from 0 to 255, which could be directly used as grayscale value in the image. The result of a single run along the test route is shown in Figure 5.4.

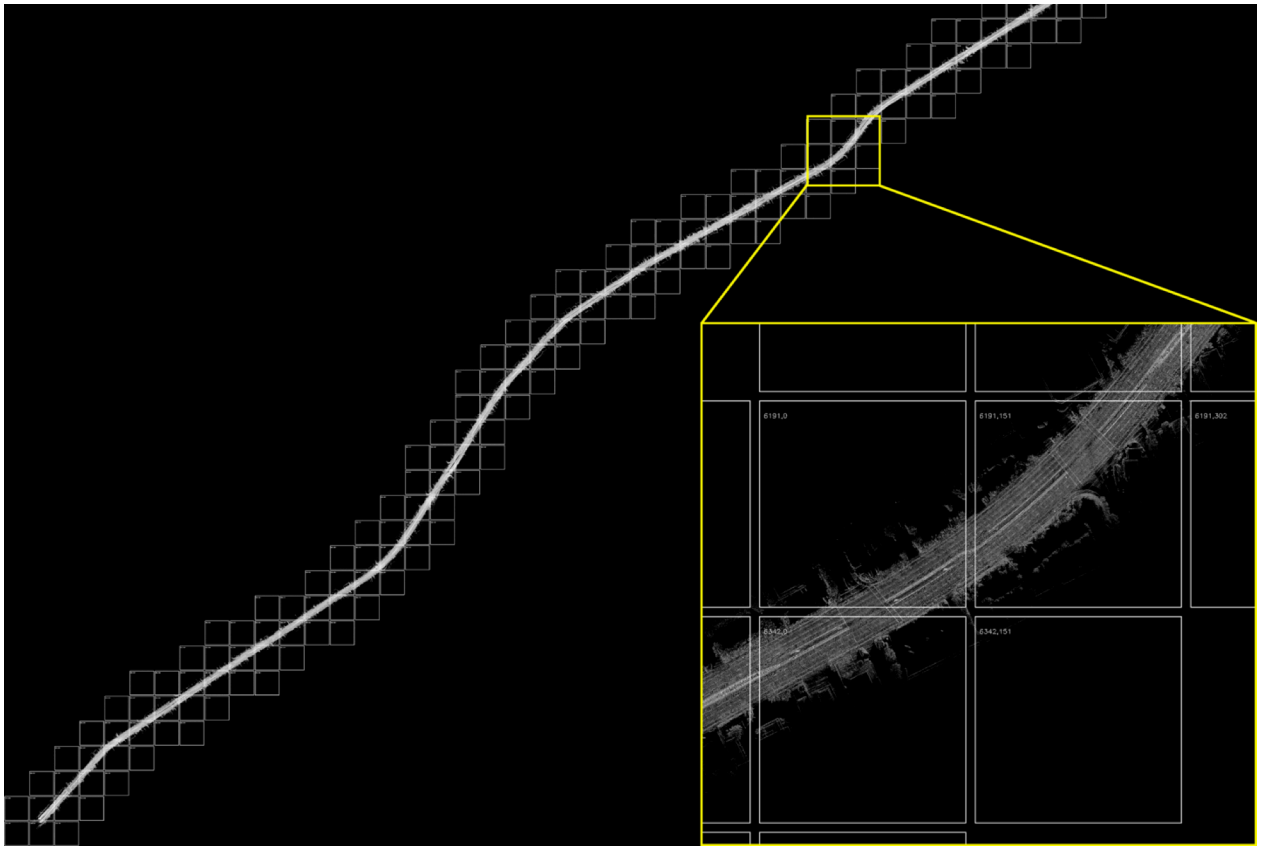

Figure 5.4 The bird's eye view intensity image of the whole trajectory is demonstrated. The north direction is pointing down, and the east direction is pointing right. Each small square represents the region of a block file.

5.4.2 Intersection Region Image Generation

The intersection region that needs to be processed is selected by detecting the mouse click position on the full image. The results of the selection are the lower and upper boundary in both North and East positions. Though the intensity image is already generated in the previous step, the focus for the intersection intensity image is on the road surface. The intensity image using average cell intensity did not filter out the above-road-surface objects like trees and other vehicle and would introduce noises to the image. The method used here utilizes the fact that the accumulated LiDAR point cloud on the road surface should occupy the lowest dense layer of points in each cell.

Before the operation, the LiDAR point cloud from different runs (in our experiment, two runs on both directions) are preprocessed and put into the same block files. In this way, the stored point cloud would have better coverage on both directions of the road surface. In the intensity image generation algorithm, the LiDAR points in each cell is sorted by their down coordinates. Then we traverse from the bottom point up to connect consecutive points with height difference smaller than a threshold. The threshold is chosen to be 5cm. Each connected cluster is defined as a layer, and the bottom layer has high probability to be the road surface layer. The intensity of the cell is represented by the median of the intensity of the bottom layer. The result is shown as Figure 5.5 (a).

5.5 Stop Bar Extraction on Image

This section describes the image processing algorithms to reliably extract stop bars on the intensity image generated from previous steps. The algorithm also uses the vehicle trajectory as an indicator of road area. In the following description, we define the

major direction as the direction of the vehicle trajectory, and minor direction as the direction perpendicular to the major direction.

5.5.1 Stop Bar Extraction in Major Direction

5.5.1.1 Image Masking using Trajectories

The essence of the stop bar extraction is to detect straight lines with high intensity using the specific characteristics of the stop bars. One key characteristic of the stop bars in the major direction is that they are mostly perpendicular to the driving direction. However, the lane markers on the minor direction have very similar property. So the intensity image is firstly masked using the vehicle trajectory on both sides to remove the lane markers on the minor directions. The driving route of the mapping platform always crosses the stop bars in the major direction, so the intersection image is masked with the inflated trajectories in both directions. The masked image is shown as Figure 5.5 (b).

5.5.1.2 Image Enhancing

Unlike camera images which covers every pixel in the FOV, the LiDAR image created from Section 5.4.2 does not guarantee that every cell which is represented as pixels in the intensity image has LiDAR detection in it. The LiDAR scans in nature is sparse. This results in lots of wholes and jagged edges in the intensity image. Image enhancement is thus necessary.

Image morphological operations and smoothing are common techniques for image enhancement. At this stage, Gaussian smoothing is applied to the intensity image. The resulting image is Figure 5.5 (c).

5.5.1.3 Rough extraction using Probabilistic Hough Transform

It is difficult to extract edges of stop bars directly on the whole intersection image, because there are many other straight lines that has similar properties. So the idea is to roughly extract the stop bars first, and then fit straight lines in the affinity of the stop bars. Probabilistic Hough Transform from [106] is applied to do initial extraction. PHT algorithm is an efficient straight line voting algorithm. It detects and extracts straight line segments from binary image. There are three parameters in PHT algorithm, voting threshold, minimum line length and maximum line gap.

The binary image is created by thresholding the grayscale image of masked intersection. The threshold is chosen to such that road surface is removed and bright stop bars are mostly reserved. After the initial step, 8 connected component labelling is applied to the image, and all connected components that has pixels smaller than 30 are removed. The binary image is shown as Figure 5.5 (d).

The parameters of PHT algorithm are loosely chosen such that multiple line segments could be extracted on the stop bars. The line segments are filtered based on their angle, and clustered based on special proximity, in order to find one line segment on each stop bar. The PHT results before and after clustering are shown as Figure 5.5 (e) and (f).

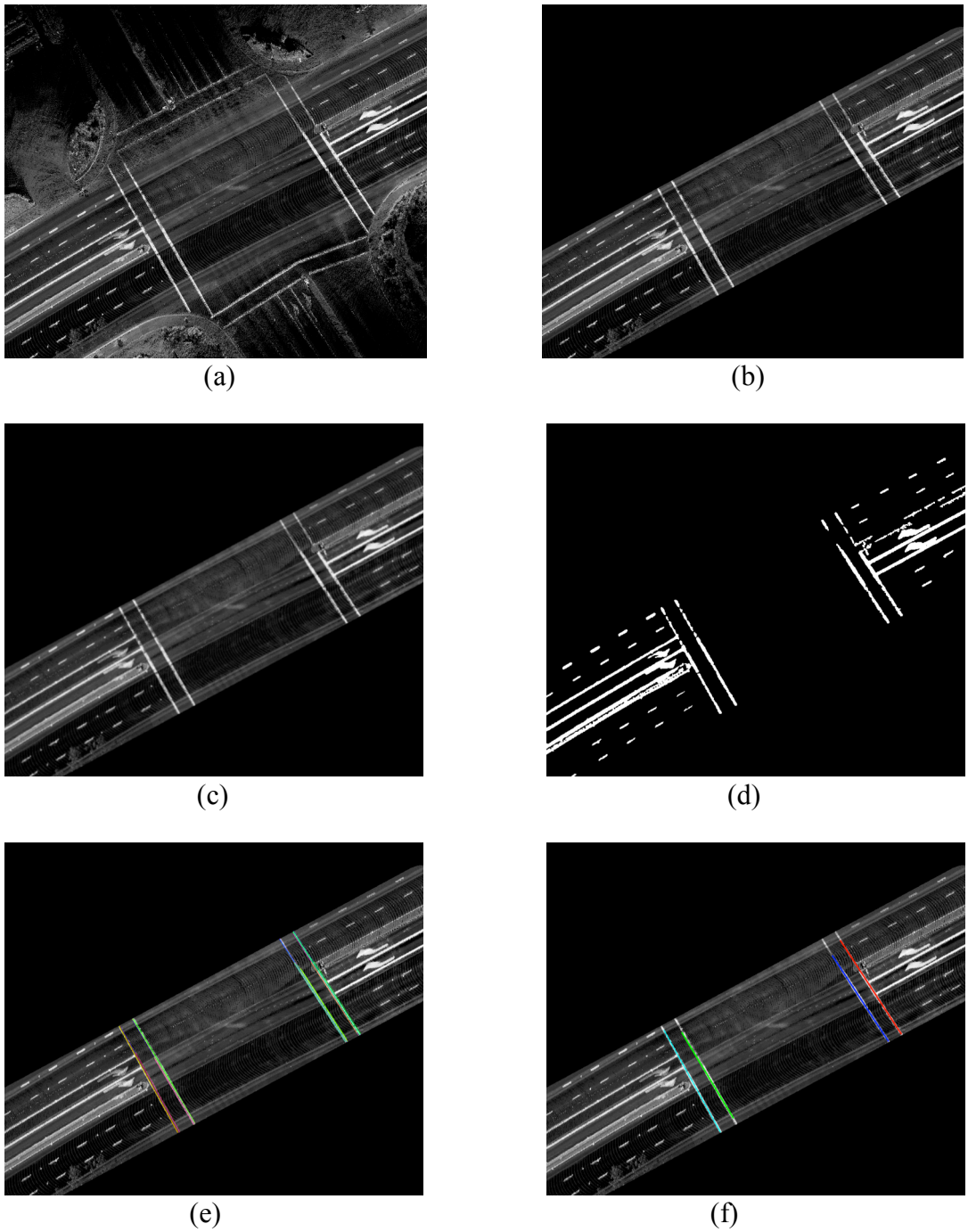

Figure 5.5 (a) is the original image; (b) is the image masked by trajectories; (c) is the smoothed image of (b); (d) is binary image of (c); (e) shows the line segments of PHT algorithm overlaid on the original image; (f) shows the final line segments after clustering.

5.5.1.4 Single Stop Bar Edge Extraction

The line segments detected with PHT does not guarantee accuracy or exact line-ends. In this section, the algorithm to fit straight lines on both edges of each stop bar is described. To generate the edge image, some preprocessing needs to be done. One is image closing, and another is Gaussian smoothing. Image closing is a morphological operation that combines erosion and dilation. Image closing operation closes holes within the image, both on the dark surface area and the bright bar areas. The Gaussian smoothing is used to smooth the jagged edges of stop bars.

After the image preprocessing step, a Canny edge detector is applied to the image. Canny edge detector is a commonly used algorithm to detect edges in a grayscale image. The algorithm can be found in many computer vision textbooks such as [107]. The thresholds are also loosely set to reserve more edges because only edges around the extracted stop bars would be used for line fitting.

The edge image is masked with inflated stop bar line segments using bitwise and operation. A single stop bar extracted from PHT algorithm is inflated to 15 pixels in width. The results covers the whole stop bar region, but removes everything else. The result preserves only edges of the current stop bar with noise. One of the resulting edge images is shown in Figure 5.6 (a). Hough transform is a discrete voting algorithm for straight line extraction. In the edge image around a single stop bar, ideally, the Hough transform line detector would return two peaks in the Hough space. However, sometimes when two edges of one stop bar are close to each other, the Hough peak extractor would

result in false detection. So in our algorithm, the largest peak in the Hough space is selected. The straight line of the other edge is extracted by the following algorithm.

The straight line parameters of the edge that is already extracted is defined as a tuple (ρ, θ), where ρ is the shortest distance from the origin to the line, and θ is the angle of the normal vector of the line. The edge image is correlated with straight lines with parameters $(\rho + \varepsilon, \theta)$ where $\varepsilon \in [-9.9, -9.8, \dots 0, 0.1, \dots, 9.9]$. The correlation calculated as the number of ones on the line. This kind of correlation could generate two peaks on the two edges of the stop bar which represent two parallel straight lines. The two peaks of the correlation curve is detected using continuous wavelet transform (find_peak_cwt function in Scipy library). The correlation curve of Figure 5.6 (a) is shown as Figure 5.6 (b).

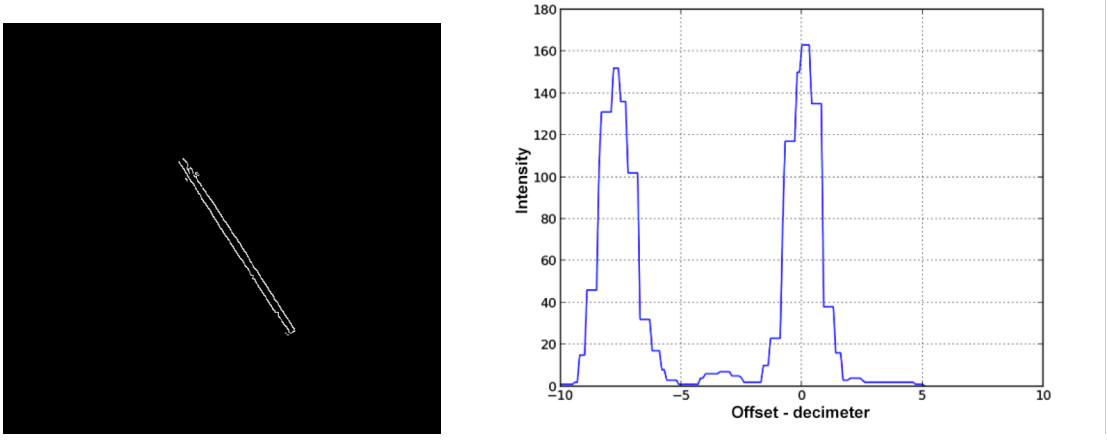

(a) (b)

Figure 5.6 (a) is the edges around one of the stop bars extracted from Section 5.5.1.3; (b) is the correlation plot.

5.5.2 Stop Bar Extraction in Minor Direction

After the stop bars edges of the major directions are extracted, the original intensity image is masked using the extracted edges to remove lane markers in the major direction. Only the area between the stop bars on both sides of the intersection is kept. The result is shown in Figure 5.7. Then the same operations in Section 5.5.1 are applied to the masked intensity image. After all the stop bar edges are extracted, they are plot onto the original intensity image, as shown in Figure 5.8.

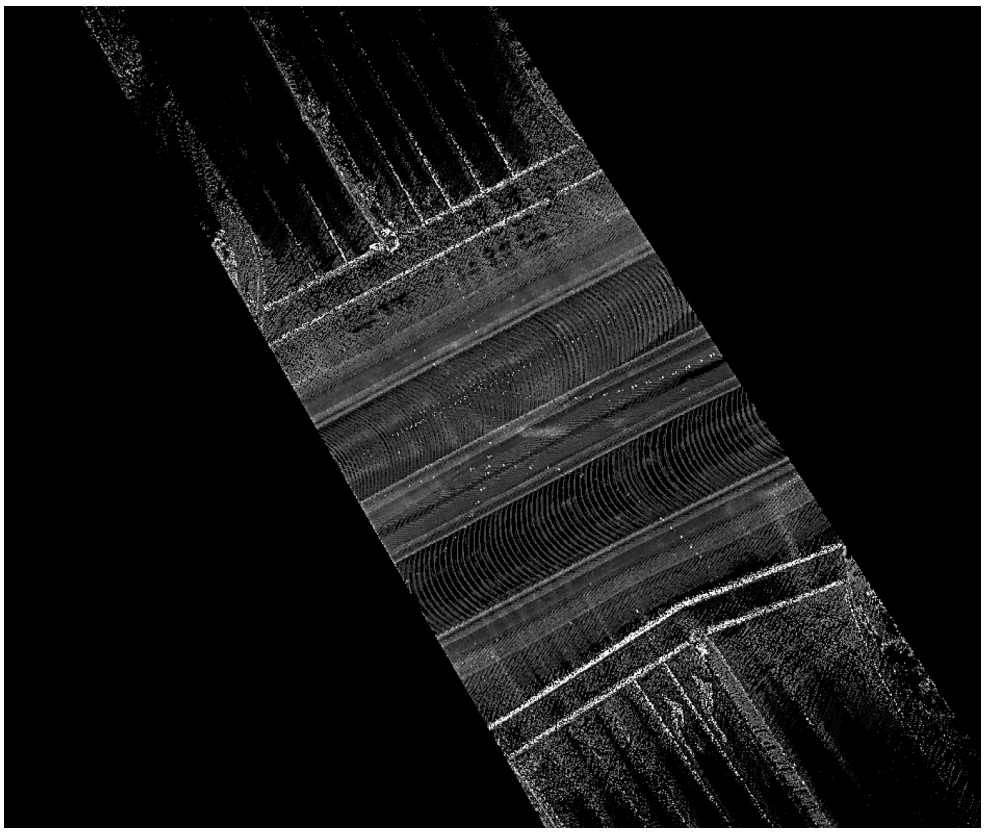

Figure 5.7 The intensity image is cropped with the stop bar in major direction. The area between stop bars on both sides are kept. The lane markers behind the stop bars are removed.

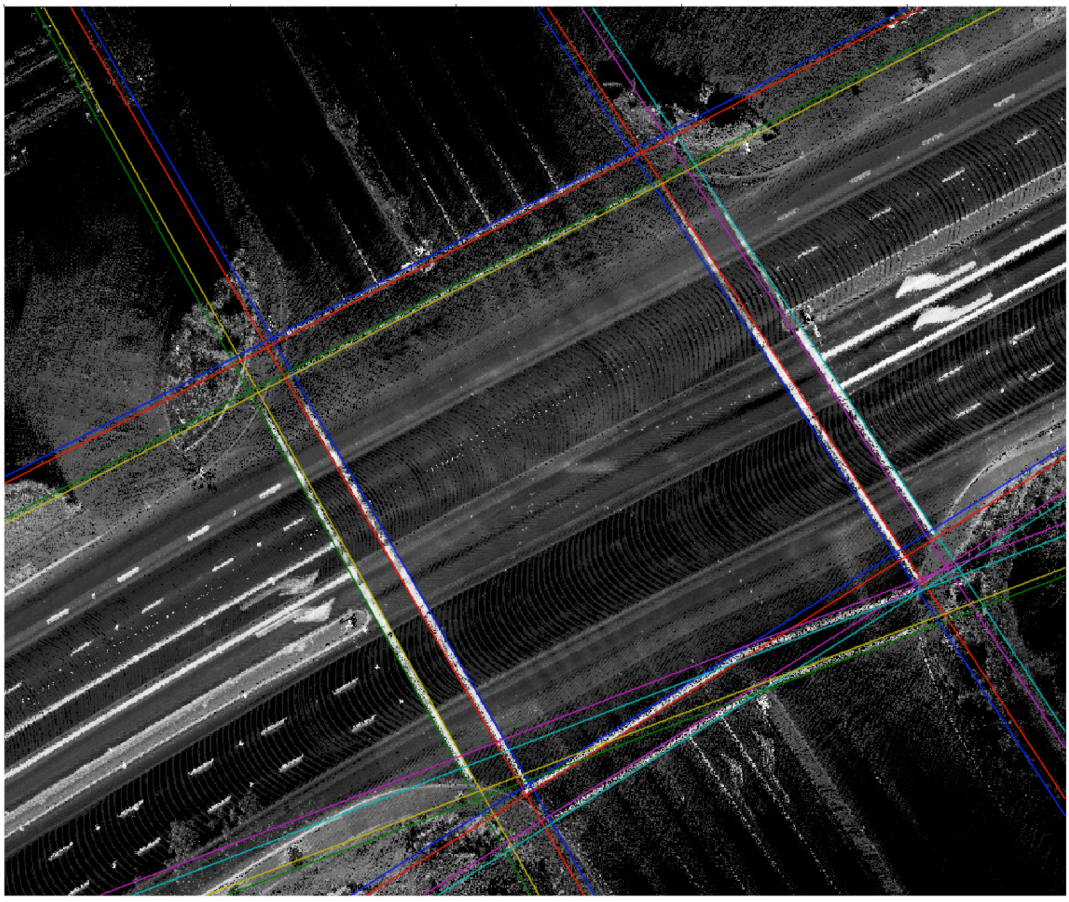

Figure 5.8 The results of the stop bar edge extraction are overlaid on the original intensity image.

5.5.3 Endpoint Determination

The results from Section 5.5.1 and 5.5.2 are straight lines with infinite length. Our target is the accurate representation of the stop bars, so the endpoints from the straight lines need to be determined. This section describes the algorithm that terminates the lines.

The first step is the combination of edges. The extracted edges from the same stop bar are combined and averaged to obtain the straight line estimate of the stop bar itself.

The average straight lines are around the middle line of the stop bars, so most of the pixels along those lines have high intensity. This fact is utilized in the following steps.

The second step calculates the intersections of all pairs of lines from the first step. The intersection points on a single line is sorted by the x or y coordinate. By connecting consecutive intersection points that are already sorted, a set of mutually exclusive line segments are generated. These line segments are guaranteed to be on certain stop bars.

It can be seen from Figure 5.9 that some of the line segments generated from step 2 are not actually on the image. We use the fact that an effective line segment should go through bright strips and both sides of the strip should be dark areas. A similar shift and correlate algorithm is applied. The algorithm is demonstrated in Figure 5.10.

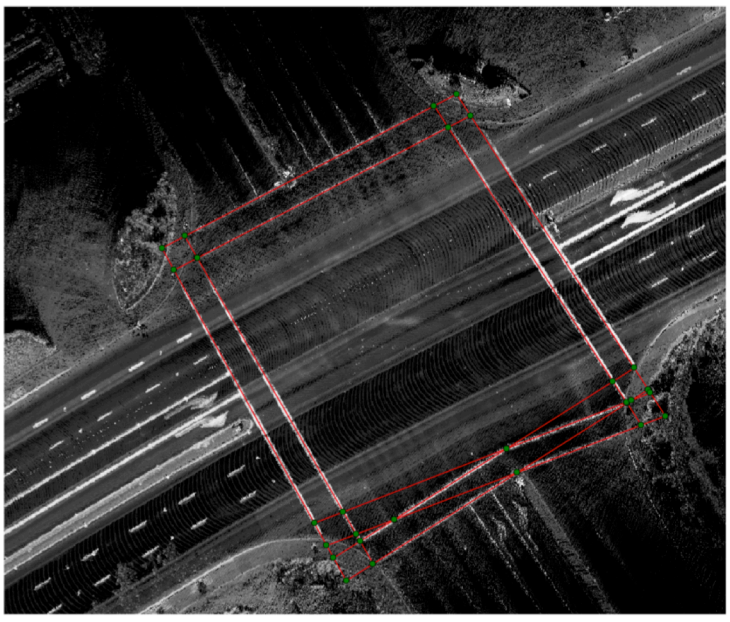

Figure 5.9 The extracted stop bar center lines are shown in red. The intersections are green dots.

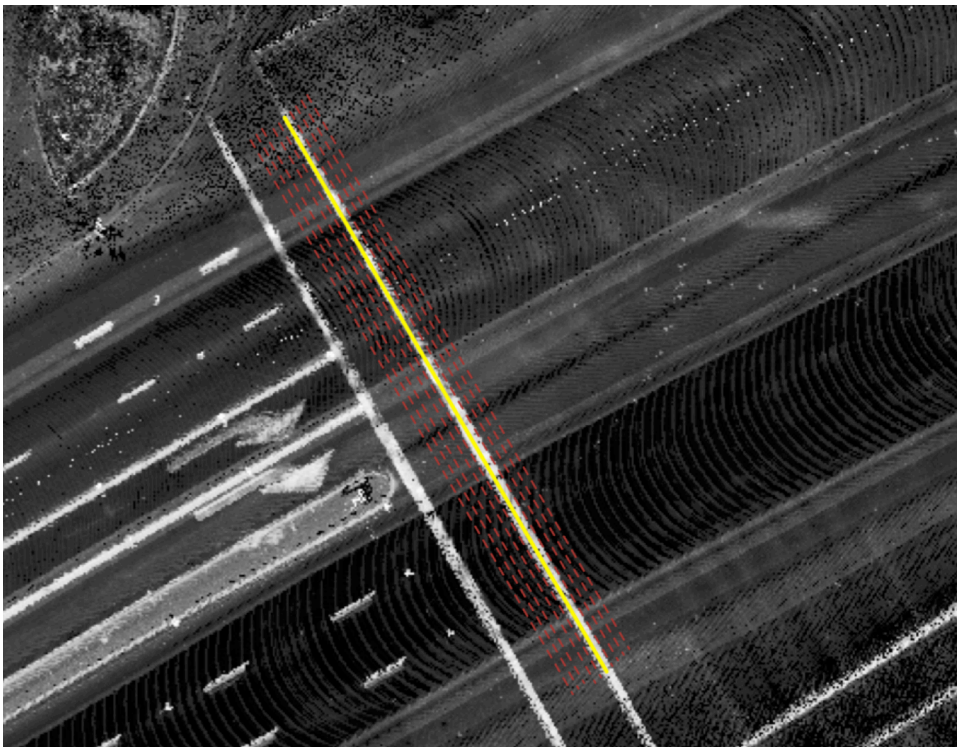

Figure 5.10 Demonstration of shift and correlate algorithm. The yellow line represents the stop bar center line. The dashed red lines represents the lines shifted in the perpendicular direction.

The stop bar center line is shifted in the perpendicular direction for $\varepsilon \in [-5, -4.5, \ldots 0, 0.5, \ldots, 4.5]$. The intensities of the pixels on the shifted line segment is averaged, and recoded as y. The plot of (ε, y) has different shape on and off the stop bar as shown in Figure 5.11. The average intensity on the stop bar would be large, and the average intensity off the stop bar would be small. So the correlation plot of the effective line segments has a hill like shape, while the plot of the invalid line segments have a random shape.

To discriminate between these two conditions, a 2nd order polynomial is fitted to the plot. The polynomial coefficient of the effective stop bar has the following property (if we define the polynomial as $y = ax^2 + bx + c$:

1. The coefficient *a* that defines the curvature is smaller than -1. The coefficient *a* of an invalid line segment is usually on the level of 0.01.

2. The symmetry axis of the fitted parabola -- $-b/2a$ – is close to 0.

If both conditions are satisfied, the line segment to be tested is identified as valid. After all segments are tested, the valid segments on the same straight line which shares common endpoints are merged together. The results are shown in Figure 5.12.

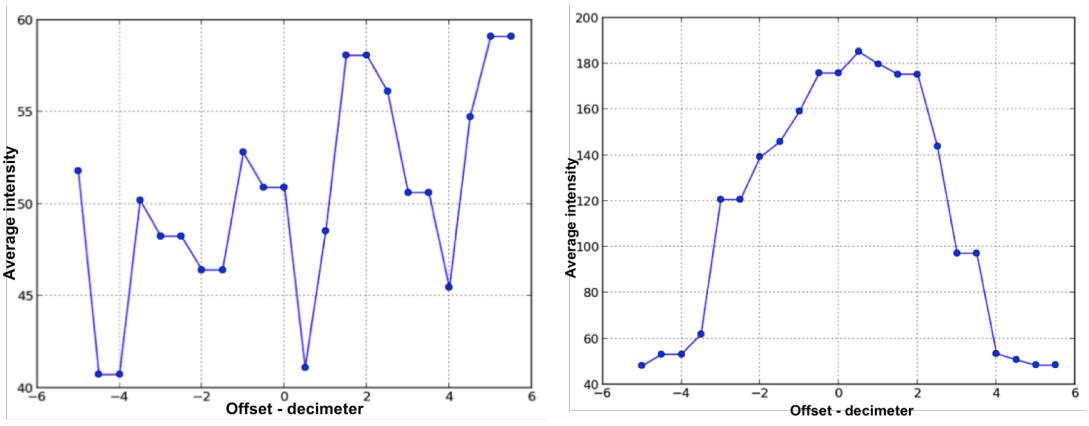

(a) (b)

Figure 5.11 (a) is the correlation plot of the line segments not on the road surface. (b) is the correlation plot of the line segments on the road surface.

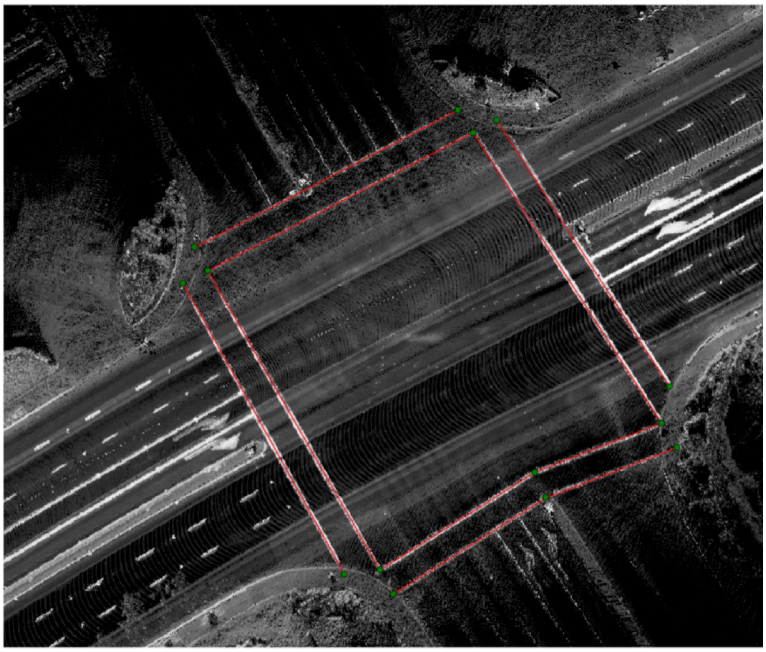

Figure 5.12 The extracted stop bar center lines after verification are shown in red. The intersections are green dots.

The end point of the stop bar center line is used to find the endpoint of stop bar edges. A line perpendicular to the centerline and passes through the endpoint intersects with both edges, and the intersections are considered as the endpoint of the stop bar edges.

5.6 Summary

This section provides a detailed description of our 3D LiDAR based mobile mapping system. The data collection, storage and processing subsystems are illustrated. Our system is unique in the positioning subsystem by estimating mapping platform trajectory using smoothing algorithm for carrier phase DGPS and IMU measurements. The storage of the vast amount of LiDAR point cloud data is challenging and is solved

with a distributed storage system. An image processing based intersection stop bar extraction algorithm is proposed and verified with field test data. On a well-structured intersection, the proposed algorithm provides accurate and reliable extraction of stop bar edges.

Chapter 6 Conclusions and Future Work

6.1 Conclusions

The increasingly advanced and sophisticated driver assistance systems are built on a foundation of reliable and accurate vehicle positioning systems. Aided positioning is going to become an indispensable part of the future vehicle. Range sensors are now receiving increasing attention in the automotive industry.

In this dissertation, we proposed a generic RADAR-aided Differential GPS/INS system. The system requires neither very expensive dual frequency GPS receiver, nor high-end IMUs, and the cost for the RADAR sensor is affordable for vehicles to equip. A simple and reliable EKF filter based sensor integration architecture is implemented. The RADAR measurements are tested, and suitable existing roadway landmarks are verified. The RADAR measurement model on the two types of landmarks we select are created. In the EKF framework, the residue and error states model of the two types of landmarks are derived. We then carried out experiments in a controlled environment to verify the proposed measurement model and the performance of the RADAR aided positioning system. It is shown that with RADAR aiding and a successful data association of measurements with known landmark positions, the absolute vehicle positioning error is bounded to be within 0.3m and the error standard deviation is also significantly reduced. Both landmarks modeled are proved to be working in the current experimental setups. Experimental results showed that our initial goal of building up accurate, reliable and highly available positioning system can be partially realized with the proposed system. The bounded positioning error proved that the accuracy of the system could be

guaranteed. The bounded positioning error standard deviation proved that the reliability is improved. However, the availability still highly depends on the availability of proper landmarks and the data association efficiency.

In the second part of this dissertation, a mobile mapping system using a 3D LiDAR as perceptive sensor is described. The offline smoothing algorithm using dual frequency GPS and IMU measurements is briefly described (proposed by former researcher). This dissertation focuses on the processing of collected LiDAR data. The whole processing flow chart is illustrated. The accurate vehicle trajectory estimation algorithm and 3D LiDAR sensor create the possibility to extract road surface feature position accurately. The intersection stop bar has unique characteristics including shape, orientation, reflectivity and position in comparison with other landmarks. The proposed stop bar extraction algorithm takes into consideration of the unique characteristics, and could reliably extract not only the straight line parameters of such stop bars but also the ending positions. Though it is only one piece of the many roadway features we want to map accurately, it is a starting point, and an inspiration for more sophisticate and more widely applicable algorithms.

6.2 Future Work

In Section 4.2.3.4, we pointed out the difficulty of RADAR feature association due to the lack of landmark property information. Our current solution is to select those landmark features that are isolated from other detectable objects, and use a strict data association criterion to guarantee correctness. So one research topic worthy of effort is the best data association method for RADAR. Other than the simple data association

algorithm described in this dissertation, there are existing algorithms from the robotics field that consider the joint probability distribution of multiple landmarks to improve the successful rate. Another direction to solving this problem is to provide more information about the landmarks so that it could be identified and verified from the environment. It is possible to combine camera image with RADAR measurements to create a more reliable identification of the landmarks. The RADAR measurement could be transformed into camera image frame, and the vicinity of the RADAR detection could be identified via computer vision, such that it could be discriminated from other objects. If a more effective data association algorithm could be designed, then RADAR measurements could be utilized more efficiently.

In this dissertation, two types of landmark features are investigated. However in the actual roadway environment, there are many more features that are detectable by RADAR and potentially used to aid positioning. It is also worthy of effort to investigate the other types of landmarks and build up the mathematical model for them.

A third future work area is the automatic surveying of landmark features. In this dissertation, the landmarks were surveyed manually with a RTK GPS. It is time consuming such that it is impractical to survey the large amount of landmarks if the RADAR aided positioning technology is wide applied. The automatic surveying technology using mobile mapping systems is necessary to create large scale landmark databases. The 3D LiDAR based Mobile Mapping system in Chapter 5 has the potential to solve this problem. The rich spatial coverage of the 3D LiDAR make it possible to

extract those point and pole features as well as many other landmarks. The identification and extraction algorithms need to be developed to utilize the LiDAR point cloud data.

The stop bar extraction algorithm proposed in Chapter 5 has some limitations. One important limitation is that it still requires human interaction. The proposed algorithm does not identify intersection areas automatically. The frame-by-frame LiDAR point cloud may be used to identify intersections. In a local LiDAR point cloud, the intersection are still well structured and distinct area in that it has discontinued lane-markers as well as road edges. We could extract road edges first and identify the intersection using discontinuity of road edges on both sides, and the existence of perpendicular bright marks. In this way, the human intervention could be prevented.

The algorithm relies highly on the high intensity of the LiDAR reflection on the stop bars. However, in practical environment, many stop bars may be worn out, or the paint material does not have significant reflectivity compared to the surrounding road surface. In such cases, the LiDAR point cloud alone could not identify the lane markers. Camera images in comparison could still capture the stop bars, because stop bars undetectable by cameras would neither be visible to human eyes. The integration of camera and LiDAR data would provide abundant information about the road way environment, and create more opportunities for feature mapping.

Bibliography

1. Glennie, C. and D.D. Lichti, *Static calibration and analysis of the Velodyne HDL-64E S2 for high accuracy mobile scanning.* Remote Sensing, 2010. **2**(6): p. 1610-1624.

2. Haala, N., et al. *Mobile lidar mapping for urban data capture*. in *Proceedings of the 14th International Conference on Virtual Systems and Multimedia, Limassol, Cyprus*. 2008.

3. Farrell, J.A., et al., *Innovative Approaches for Next Generation Vehicle Positioning*. 2012.

4. Farrell, J.A., T.D. Givargis, and M.J. Barth, *Real-time differential carrier phase GPS-aided INS.* Control Systems Technology, IEEE Transactions on, 2000. **8**(4): p. 709-721.

5. Kharrazi, S. and T. Ardeshiri, *Data Fusion for Vehicle Positioning in Intersection Active Safety Applications.* 2005.

6. Farrell, J., *Aided navigation: GPS with high rate sensors*. 2008: McGraw-Hill New York, NY, USA:.

7. Puente, I., et al., *Review of mobile mapping and surveying technologies.* Measurement, 2013. **46**(7): p. 2127-2145.

8. Li, R., *Mobile mapping: An emerging technology for spatial data acquisition.* Photogrammetric Engineering and Remote Sensing, 1997. **63**(9): p. 1085-1092.

9. Aono, T., et al. *Positioning of vehicle on undulating ground using GPS and dead reckoning*. in *Robotics and Automation, 1998. Proceedings. 1998 IEEE International Conference on*. 1998. IEEE.

10. Rogers, R.M. *Land vehicle navigation filtering for a GPS/dead-reckoning system*. in *Proceedings of the 1997 National Technical Meeting of The Institute of Navigation*. 1997.

11. Da, R. *Investigation of a low-cost and high-accuracy GPS/IMU system*. in *Proceedings of the 1997 National Technical Meeting of The Institute of Navigation*. 1997.

12. Zhou, J. and H. Bolandhemmat. *Integrated INS/GPS system for an autonomous mobile vehicle*. in *Mechatronics and Automation, 2007. ICMA 2007. International Conference on*. 2007. IEEE.

13. Li, Y., et al. *Low-cost tightly coupled GPS/INS integration based on a nonlinear Kalman filtering design*. in *Proceedings of ION National Technical Meeting*. 2006.

14. Toledo-Moreo, R., et al., *High-integrity IMM-EKF-based road vehicle navigation with low-cost GPS/SBAS/INS.* Intelligent Transportation Systems, IEEE Transactions on, 2007. **8**(3): p. 491-511.

15. Qasem, H. and L. Reindl. *Unscented and extended Kalman estimators for non linear indoor tracking using distance measurements*. 2007. IEEE.

16. Zhang, P., et al. *Navigation with IMU/GPS/digital compass with unscented Kalman filter*. in *Mechatronics and Automation, 2005 IEEE International Conference*. 2005. IEEE.

17. Yi, Y. and D. Grejner-Brzezinska. *Tightly-coupled GPS/INS integration using unscented Kalman filter and particle filter*. in *Proceedings of the 19th International Technical Meeting of the Satellite Division of The Institute of Navigation (ION GNSS 2006)*. 2001.

18. Giremus, A., et al., *A Rao-Blackwellized particle filter for INS/GPS integration.* 2004.

19. Gross, J., et al. *A comparison of extended kalman filter, sigma-point kalman filter, and particle filter in GPS/INS sensor fusion*. in *AIAA Guidance, Navigation, and Control Conference*. 2010.

20. Schmidt, G.T. and R.E. Phillips, *INS/GPS Integration Architecture Performance Comparisons*. Advances in Navigation Sensors and Integration Technology.

21. Farrell, J. and M. Barth, *The global positioning system and inertial navigation*. Vol. 61. 1999: McGraw-Hill New York.

22. Dai, L., et al. *Pseudolite applications in positioning and navigation: Modelling and geometric analysis*. in *Int. Symp. on Kinematic Systems in Geodesy, Geomatics & Navigation (KIS2001)*. 2001.

23. de Lara, E. and S. Saroiu. *CILoS: a CDMA indoor localization system*. in *Proceedings of the 10th international conference on Ubiquitous computing*. 2008. ACM.

24. Otsason, V., et al., *Accurate GSM indoor localization*, in *UbiComp 2005: Ubiquitous Computing*. 2005, Springer. p. 141-158.

25. Wang, X., Y. Wu, and J.-Y. Chouinard, *A new position location system using DTV transmitter identification watermark signals.* EURASIP Journal on Applied Signal Processing, 2006. **2006**: p. 155-155.

26. Rabinowitz, M. and J.J. Spilker Jr, *A new positioning system using television synchronization signals.* Broadcasting, IEEE Transactions on, 2005. **51**(1): p. 51-61.

27. Youssef, A., et al. *Computing location from ambient FM radio signals [commercial radio station signals]*. in *Wireless Communications and Networking Conference, 2005 IEEE*. 2005. IEEE.

28. Popleteev, A., *Indoor positioning using FM radio signals*. 2011, University of Trento.

29. Hall, T.D., C.C. Charles III, and P.N. Misra. *Radiolocation using AM broadcast signals: Positioning performance*. in *Proceedings of the 15th International Technical Meeting of the Satellite Division of The Institute of Navigation (ION GPS 2002)*. 2001.

30. Evennou, F. and F. Marx, *Advanced integration of WiFi and inertial navigation systems for indoor mobile positioning.* Eurasip journal on applied signal processing, 2006. **2006**: p. 164-164.

31. sYe, X., *WiFiPoz--an accurate indoor positioning system.* 2012.

32. Alam, N., A.T. Balaei, and A.G. Dempster, *An Instantaneous Lane-Level Positioning Using DSRC Carrier Frequency Offset.* Intelligent Transportation Systems, IEEE Transactions on, 2012. **PP**(99): p. 1-10.

33. Vu, A.Q., *Robust Vehicle State Estimation for Improved Traffic Sensing and Management.* 2011.

34. Nistér, D., O. Naroditsky, and J. Bergen, *Visual odometry for ground vehicle applications.* Journal of Field Robotics, 2006. **23**(1): p. 3-20.

35. Li, M. and A.I. Mourikis, *High-precision, consistent EKF-based visual–inertial odometry.* The International Journal of Robotics Research, 2013. **32**(6): p. 690-711.

36. Zheng, D., et al. *LED-based initialization and navigation*. in *American Control Conference (ACC), 2013*. 2013. IEEE.

37. Vu, A., et al., *Real-time computer vision/DGPS-aided inertial navigation system for lane-level vehicle navigation.* Intelligent Transportation Systems, IEEE Transactions on, 2012. **13**(2): p. 899-913.

38. *Sick LMS500 Series.* Available from: https://www.mysick.com/partnerPortal/ProductCatalog/DataSheet.aspx?ProductID=45446.

39. Zhao, S. and J.A. Farrell. *2D LIDAR Aided INS for vehicle positioning in urban environments*. in *Control Applications (CCA), 2013 IEEE International Conference on*. 2013. IEEE.

40. Levinson, J. and S. Thrun. *Robust vehicle localization in urban environments using probabilistic maps*. in *Robotics and Automation (ICRA), 2010 IEEE International Conference on*. 2010. IEEE.

41. Bulusu, N., J. Heidemann, and D. Estrin, *GPS-less low-cost outdoor localization for very small devices.* Personal Communications, IEEE, 2000. **7**(5): p. 28-34.

42. Chon, H.D., et al., *Using RFID for accurate positioning.* Positioning, 2004. **1**(08).

43. Trevisani, E. and A. Vitaletti. *Cell-ID location technique, limits and benefits: an experimental study*. in *Mobile Computing Systems and Applications, 2004. WMCSA 2004. Sixth IEEE Workshop on*. 2004. IEEE.

44. Hoene, C. and J. Willmann. *Four-way TOA and software-based trilateration of IEEE 802.11 devices*. in *Personal, Indoor and Mobile Radio Communications, 2008. PIMRC 2008. IEEE 19th International Symposium on*. 2008. IEEE.

45. Priyantha, N.B., A. Chakraborty, and H. Balakrishnan. *The cricket location-support system*. in *Proceedings of the 6th annual international conference on Mobile computing and networking*. 2000. ACM.

46. Harter, A., et al., *The anatomy of a context-aware application.* Wireless Networks, 2002. **8**(2/3): p. 187-197.

47. Barnes, J., et al. *Locata: a new positioning technology for high precision indoor and outdoor positioning*. in *Proceedings 2003 International Symposium on GPS\ GNSS*. 2003.

48. Yamasaki, R., et al. *TDOA location system for IEEE 802.11 b WLAN*. in *Wireless Communications and Networking Conference, 2005 IEEE*. 2005. IEEE.

49. Mensing, C. and S. Plass. *Positioning algorithms for cellular networks using TDOA*. in *Acoustics, Speech and Signal Processing, 2006. ICASSP 2006 Proceedings. 2006 IEEE International Conference on*. 2006. IEEE.

50. Fisher, K.A., *The navigation potential of signals of opportunity-based time difference of arrival measurements*. 2005, DTIC Document.

51. McEllroy, J.A., *Navigation using signals of opportunity in the AM transmission band*. 2006, DTIC Document.

52. Moon, G.B., G.-I. Jee, and J.G. Lee, *Position determination using the DTV segment sync signal.* International Journal of Control, Automation and Systems, 2011. **9**(3): p. 574-580.

53. Deng, P. and P. Fan. *An AOA assisted TOA positioning system*. in *Communication Technology Proceedings, 2000. WCC-ICCT 2000. International Conference on*. 2000. IEEE.

54. Wann, C.-D., Y.-J. Yeh, and C.-S. Hsueh. *Hybrid TDOA/AOA indoor positioning and tracking using extended Kalman filters*. in *Vehicular Technology Conference, 2006. VTC 2006-Spring. IEEE 63rd*. 2006. IEEE.

55. Chien-Sheng, C., S. Szu-Lin, and Y.-F. Huang, *Hybrid TOA/AOA geometrical positioning schemes for mobile location.* IEICE transactions on communications, 2009. **92**(2): p. 396-402.

56. Lin, T.-N. and P.-C. Lin. *Performance comparison of indoor positioning techniques based on location fingerprinting in wireless networks*. in *Wireless Networks, Communications and Mobile Computing, 2005 International Conference on*. 2005. IEEE.

57. Swords, S.S., *Technical history of the beginnings of radar*. 1986: P. Peregrinus.

58. Scheer, J.A. and W.L. Melvin, *Principles of modern radar*. 2013: The Institution of Engineering and Technology.

59. Cho, A., et al. *Altitude integration of radar altimeter and GPS/INS for automatic takeoff and landing of a UAV*. in *Control, Automation and Systems (ICCAS), 2011 11th International Conference on*. 2011. IEEE.

60. Bevington, J.E. and C.A. Marttila. *Precision aided inertial navigation using SAR and digital map data*. in *Position Location and Navigation Symposium, 1990. Record. The 1990's - A Decade of Excellence in the Navigation Sciences. IEEE PLANS '90., IEEE*. 1990.

61. Yongmin, Z., G. Shesheng, and L. Wei, *A Quaternion-Based Method for SINS/SAR Integrated Navigation System.* Aerospace and Electronic Systems, IEEE Transactions on, 2012. **48**(1): p. 514-524.

62. Hargrave, C.O., et al. *Radar target identification of mining infrastructure for automated mine machinery navigation*. in *Antennas and Propagation (EUCAP), Proceedings of the 5th European Conference on*. 2011.

63. Gerlach, K. and C. Rahmig. *Multi-hypothesis based map-matching algorithm for precise train positioning*. in *Information Fusion, 2009. FUSION '09. 12th International Conference on*. 2009.

64. Yokoo, K., S. Beauregard, and M. Schneider. *Indoor Relative Localization with Mobile Short-Range Radar*. in *Vehicular Technology Conference, 2009. VTC Spring 2009. IEEE 69th*. 2009.

65. Langer, D. and C. Thorpe, *Range sensor based outdoor vehicle Navigation, collision avoidance and parallel parking.* Autonomous Robots, 1995. **2**(2): p. 147-161.

66. Tokoro, S., et al. *Electronically scanned millimeter-wave radar for pre-crash safety and adaptive cruise control system*. 2003. IEEE.

67. Wenger, J. *Automotive radar - status and perspectives*. in *Compound Semiconductor Integrated Circuit Symposium, 2005. CSIC '05. IEEE*. 2005.

68. Ryde, J. and N. Hillier, *Performance of laser and radar ranging devices in adverse environmental conditions.* Journal of Field Robotics, 2009. **26**(9): p. 712-727.

69. Ringdahl, O., *Techniques and Algorithms for Autonomous Vehicles in Forest Environment*, in *Department of Computing Science*. 2007, Umea University.

70. Curlander, J.C. and R.N. McDonough, *Synthetic aperture radar*. 1991: John Wiley & Sons.

71. Quist, E.B. and R.W. Beard, *Radar Odometry on Small Unmanned Aircraft.* Submitted GNC, 2013. **2013**: p. 1-18.

72. Vivet, D., P. Checchin, and R. Chapuis. *Radar-only localization and mapping for ground vehicle at high speed and for riverside boat*. in *Robotics and Automation (ICRA), 2012 IEEE International Conference on*. 2012. IEEE.

73. Vivet, D., et al., *Mobile Ground-Based Radar Sensor for Localization and Mapping: An Evaluation of two Approaches.* International Journal of Advanced Robotic Systems, 2013. **10**(307): p. 12.

74. Greco, M., et al. *SAR and InSAR georeferencing algorithms for inertial navigation systems*. in *Photonics Applications in Astronomy, Communications, Industry, and High-Energy Physics Experiments 2011*. 2011. International Society for Optics and Photonics.

75. Gao, S., et al., *Multi-sensor optimal data fusion for INS/GPS/SAR integrated navigation system.* Aerospace science and technology, 2009. **13**(4): p. 232-237.

76. Clark, S. and G. Dissanayake. *Simultaneous localisation and map building using millimetre wave radar to extract natural features*. in *Robotics and Automation, 1999. Proceedings. 1999 IEEE International Conference on*. 1999.

77. Kimoto, K. and C. Thorpe. *Map building with radar and motion sensors for automated highway vehicle navigation*. in *Intelligent Robots and Systems, 1997. IROS '97., Proceedings of the 1997 IEEE/RSJ International Conference on*. 1997.

78. Clark, S. and G. Dissanayake. *Simultaneous localisation and map building using millimetre wave radar to extract natural features*. 1999. IEEE.

79. Durrant-Whyte, H.F., *An Autonomous Guided Vehicle for Cargo Handling Applications.* The International Journal of Robotics Research, 1996. **15**(5): p. 407-440.

80. Novak, K. and J. Bossler, *Development and application of the highway mapping system of Ohio State University.* The Photogrammetric Record, 1995. **15**(85): p. 123-134.

81. *GPSVision*. Available from: http://www.lambdatech.com/GPSVOverview.html.

82. *VISAT*. Available from: http://www.amsvisat.com/.

83. Hock, C., et al. *Architecture and design of the kinematic survey system KiSS*. in *Proceedings of the 3rd International Workshop on High Precision Navigation*. 1995.

84. Brown, A. *High accuracy targeting using a GPS-aided inertial measurement unit*. in *ION 54th Annual Meeting*. 1998.

85. *SITECO RoadScanner*. Available from: http://www.sitecoinf.it/index.php/en/solutions/road-scanner-mms.

86. *TOPCON IP-S2*. Available from: http://www.topconpositioning.com/products/mobile-mapping/ip-s2-compact.

87. *Trimble MX8*. Available from: http://www.trimble.com/imaging/Trimble-MX8.aspx.

88. Mancini, A., E. Frontoni, and P. Zingaretti. *Automatic road object extraction from Mobile Mapping Systems*. in *Mechatronics and Embedded Systems and Applications (MESA), 2012 IEEE/ASME International Conference on*. 2012. IEEE.

89. Yu, Y., et al., *Learning Hierarchical Features for Automated Extraction of Road Markings From 3-D Mobile LiDAR Point Clouds.*

90. Yang, B., et al., *Automated extraction of road markings from mobile LiDAR point clouds.* Photogrammetric Engineering & Remote Sensing, 2012. **78**(4): p. 331-338.

91. Brenner, C., *Extraction of features from mobile laser scanning data for future driver assistance systems*, in *Advances in GIScience*. 2009, Springer. p. 25-42.

92. Smadja, L., J. Ninot, and T. Gavrilovic, *Road extraction and environment interpretation from Lidar sensors.* IAPRS, 2010. **38**: p. 281-286.

93. Zhang, W. *Lidar-based road and road-edge detection*. in *Intelligent Vehicles Symposium (IV), 2010 IEEE*. 2010. IEEE.

94. Miyazaki, R., et al., *A line-based approach for precise extraction of road and curb region from mobile mapping data.* ISPRS Annals of Photogrammetry, Remote Sensing and Spatial Information Sciences, 2014. **1**: p. 243-250.

95. wJaehyun, H., et al., *Enhanced Road Boundary and Obstacle Detection Using a Downward-Looking LIDAR Sensor.* Vehicular Technology, IEEE Transactions on, 2012. **61**(3): p. 971-985.

96. Kang, Y., et al., *A lidar-based decision-making method for road boundary detection using multiple kalman filters.* Industrial Electronics, IEEE Transactions on, 2012. **59**(11): p. 4360-4368.

97. Knott, E.F., J.F. Schaeffer, and M.T. Tuley, *Radar Cross Section*. 2nd ed. 2004, Raleigh, NC: SCITECH Publishing, INC. 611.

98. *Davis Instruments Echomaster*. Available from: http://www.davisnet.com/marine/products/marine_product.asp?pnum=00152.

99. Collins, J. and J. Uhlmann, *Efficient gating in data association with multivariate gaussian distributed states.* Aerospace and Electronic Systems, IEEE Transactions on, 1992. **28**(3): p. 909-916.

100. Anderson, T.W., *An introduction to multivariate statistical analysis*. Vol. 2. 1958: Wiley New York.

101. Neira, J. and J.D. Tardos, *Data association in stochastic mapping using the joint compatibility test.* Robotics and Automation, IEEE Transactions on, 2001. **17**(6): p. 890-897.

102. Vu, A., et al., *Real-Time Computer Vision/DGPS-Aided Inertial Navigation System for Lane-Level Vehicle Navigation.* Intelligent Transportation Systems, IEEE Transactions on, 2012. **PP**(99): p. 1-15.

103. Haitao, X., et al. *Development and evaluation of an enhanced eco-approach traffic signal application for Connected Vehicles*. in *Intelligent Transportation Systems - (ITSC), 2013 16th International IEEE Conference on*. 2013.

104. Vu, A., J. Farrell, and M. Barth, *Centimeter-Accuracy Smoothed Vehicle Trajectory Estimation.* Intelligent Transportation Systems Magazine, IEEE, 2013. **5**(4): p. 121-135.

105. Dellaert, F. and M. Kaess, *Square Root SAM: Simultaneous localization and mapping via square root information smoothing.* The International Journal of Robotics Research, 2006. **25**(12): p. 1181-1203.

106. Matas, J., C. Galambos, and J. Kittler, *Robust detection of lines using the progressive probabilistic hough transform.* Computer Vision and Image Understanding, 2000. **78**(1): p. 119-137.

107. Shapiro, L. and G.C. Stockman, *Computer Vision. 2001.* ed: Prentice Hall, 2001.

Appendix

A. Derivation of Radar Measurement Model

The relationship between the actual and estimated rotation matrix is defined as:

$$
\begin{aligned}
{}^{G}_{B}\hat{\mathbf{R}} &= (\mathbf{I} - \lfloor \boldsymbol{\rho} \times \rfloor)\, {}^{G}_{B}\mathbf{R} \\
{}^{B}_{G}\hat{\mathbf{R}} &= {}^{B}_{G}\mathbf{R}\, (\mathbf{I} + \lfloor \boldsymbol{\rho} \times \rfloor) \\
{}^{B}_{G}\mathbf{R} &= {}^{B}_{G}\hat{\mathbf{R}}\, (\mathbf{I} - \lfloor \boldsymbol{\rho} \times \rfloor) \\
{}^{G}_{B}\mathbf{R} &= (\mathbf{I} + \lfloor \boldsymbol{\rho} \times \rfloor)\, {}^{G}_{B}\hat{\mathbf{R}}
\end{aligned}
$$

A.1 Point feature

The known landmark position is denoted as ${}^{G}\mathbf{p}_{L}^{i}$, which is surveyed and known as a priori. The landmark position can be converted to Radar frame {R} using

$$
{}^{R}\mathbf{p}_{L}^{i} = {}^{R}_{B}\mathbf{R}\ {}^{B}_{G}\mathbf{R}({}^{G}\mathbf{p}_{L}^{i} - {}^{G}\mathbf{p}_{B}) - {}^{R}_{B}\mathbf{R}{}^{B}\mathbf{T}_{BR}
$$

The measurement model is defined in Equation 错误! 未找到引用源。.

The measurement residue is $\delta\mathbf{z} = \mathbf{z} - \tilde{\mathbf{z}}$, so the linearized measurement matrix can be calculated as

$$
\mathbf{H} = \frac{\partial h}{\partial {}^{G}\mathbf{x}} = \frac{\partial h}{\partial {}^{R}\mathbf{p}_{L}^{i}} \frac{\partial {}^{R}\mathbf{p}_{L}^{i}}{\partial {}^{G}\mathbf{x}}
$$

The Radar measurement is denoted as $\tilde{\mathbf{z}} = [\tilde{d} \quad \tilde{\beta}]^{T}$

The relationship between scalar terms ${}^{R}x^{i}$, ${}^{R}y^{i}$ and ${}^{R}\mathbf{p}_{L}^{i}$ is

$$
\begin{aligned}
{}^{R}x^{i} &= {}^{R}e_1 \cdot {}^{R}\mathbf{p}_L^i \\
{}^{R}y^{i} &= {}^{R}e_2 \cdot {}^{R}\mathbf{p}_L^i,
\end{aligned}
$$

where ${}^{R}e_1 = [\ 1\ 0\ 0\ ]^T$ and ${}^{R}e_2 = [\ 0\ 1\ 0\ ]^T$.

The first term in **H** can be calculated separately as

$$
\frac{\partial d}{\partial {}^{R}\mathbf{p}_L^i} = \begin{bmatrix} \frac{\partial d}{\partial {}^{R}x^i} & \frac{\partial d}{\partial {}^{R}y^i} & 0 \end{bmatrix} = \begin{bmatrix} \frac{{}^{R}e_1 \cdot {}^{R}\mathbf{p}_L^i}{\|{}^{R}\mathbf{p}_L^i\|} & \frac{{}^{R}e_2 \cdot {}^{R}\mathbf{p}_L^i}{\|{}^{R}\mathbf{p}_L^i\|} & 0 \end{bmatrix}
$$

$$
\frac{\partial \beta}{\partial {}^{R}\mathbf{p}_L^i} = \begin{bmatrix} \frac{\partial \beta}{\partial {}^{R}x^i} & \frac{\partial \beta}{\partial {}^{R}y^i} & 0 \end{bmatrix} = \begin{bmatrix} \frac{-{}^{R}e_2 \cdot {}^{R}\mathbf{p}_L^i}{\|{}^{R}\mathbf{p}_L^i\|^2} & \frac{{}^{R}e_1 \cdot {}^{R}\mathbf{p}_L^i}{\|{}^{R}\mathbf{p}_L^i\|^2} & 0 \end{bmatrix}
$$

So the combination of the two equations above results in

$$
\frac{\partial h}{\partial {}^{R}\mathbf{p}_L^i} = \begin{bmatrix} \frac{\partial d}{\partial {}^{R}\mathbf{p}_L^i} \\ \\ \frac{\partial \beta}{\partial {}^{R}\mathbf{p}_L^i} \end{bmatrix} = \begin{bmatrix} \frac{{}^{R}e_1 \cdot {}^{R}\mathbf{p}_L^i}{\|{}^{R}\mathbf{p}_L^i\|} & \frac{{}^{R}e_2 \cdot {}^{R}\mathbf{p}_L^i}{\|{}^{R}\mathbf{p}_L^i\|} & 0 \\ \\ \frac{-{}^{R}e_2 \cdot {}^{R}\mathbf{p}_L^i}{\|{}^{R}\mathbf{p}_L^i\|^2} & \frac{{}^{R}e_1 \cdot {}^{R}\mathbf{p}_L^i}{\|{}^{R}\mathbf{p}_L^i\|^2} & 0 \end{bmatrix}
$$

The second partial derivate in **H** equation is derived with the following equations.

$$
\begin{aligned}
{}^{R}\mathbf{p}_L^i &= {}_{B}^{R}\mathbf{R}\ {}_{G}^{B}\mathbf{R}({}^{G}\mathbf{p}_L^i - {}^{G}\mathbf{p}_B) - {}_{B}^{R}\mathbf{R}\,{}^{B}\mathbf{T}_{BR} \\
&= {}_{B}^{R}\mathbf{R}\ {}_{G}^{B}\hat{\mathbf{R}}\,(\mathbf{I} - \lfloor \boldsymbol{\rho} \times \rfloor)\left[\left({}^{G}\mathbf{p}_L^i - {}^{G}\hat{\mathbf{p}}_B\right) - \delta {}^{G}\mathbf{p}_B\right] - {}_{B}^{R}\mathbf{R}\,{}^{B}\mathbf{T}_{BR} \\
&= \left[{}_{B}^{R}\mathbf{R}\ {}_{G}^{B}\hat{\mathbf{R}}\left({}^{G}\mathbf{p}_L^i - {}^{G}\hat{\mathbf{p}}_B\right) - {}_{B}^{R}\mathbf{R}\,{}^{B}\mathbf{T}_{BR}\right] - {}_{B}^{R}\mathbf{R}\ {}_{G}^{B}\hat{\mathbf{R}}\lfloor \boldsymbol{\rho} \times \rfloor\left({}^{G}\mathbf{p}_L^i - {}^{G}\hat{\mathbf{p}}_B\right) \\
&\quad - {}_{B}^{R}\mathbf{R}\ {}_{G}^{B}\hat{\mathbf{R}}\ \delta {}^{G}\mathbf{p}_B + {}_{B}^{R}\mathbf{R}\ {}_{G}^{B}\hat{\mathbf{R}}\lfloor \boldsymbol{\rho} \times \rfloor\,\delta {}^{G}\mathbf{p}_B
\end{aligned}
$$

The first term is the same as ${}^{R}\hat{\mathbf{p}}_L^i$, the last term is the product of two error states, and are considered as 2nd order term, and is ignored in this derivation.

Using the properties of cross products, the second term can be converted to

$$
{}_{B}^{R}\mathbf{R}\ {}_{G}^{B}\hat{\mathbf{R}}\lfloor \boldsymbol{\rho} \times \rfloor\left({}^{G}\mathbf{p}_L^i - {}^{G}\hat{\mathbf{p}}_B\right) = -{}_{B}^{R}\mathbf{R}\ {}_{G}^{B}\hat{\mathbf{R}}\left\lfloor \left({}^{G}\mathbf{p}_L^i - {}^{G}\hat{\mathbf{p}}_B\right) \times \right\rfloor \boldsymbol{\rho}
$$

So the error state equation is then converted to

$$\delta^R\mathbf{p}_L^i = {}_B^R\mathbf{R}\ {}_G^B\hat{\mathbf{R}}\left\lfloor {}^G\hat{\mathbf{T}}_{Bi}\times\right\rfloor \boldsymbol{\rho} - {}_B^R\mathbf{R}\ {}_G^B\hat{\mathbf{R}}\ \delta^G\mathbf{p}_B$$

$$= {}_B^R\mathbf{R}\ {}_G^B\hat{\mathbf{R}}\begin{bmatrix} -\mathbf{I} & \mathbf{0} & \left\lfloor {}^G\hat{\mathbf{T}}_{Bi}\times\right\rfloor & \mathbf{0} & \mathbf{0}\end{bmatrix}\begin{bmatrix}\delta\mathbf{p}\\ \delta\mathbf{v}\\ \boldsymbol{\rho}\\ \delta\mathbf{b}_a\\ \delta\mathbf{b}_g\end{bmatrix}$$

where ${}^G\hat{\mathbf{T}}_{Bi} = {}^G\mathbf{p}_L^i - {}^G\hat{\mathbf{p}}_B$.

Combining all the equations above, the H matrix is

$$\mathbf{H} = \mathbf{A}\ {}_B^R\mathbf{R}\ {}_G^B\hat{\mathbf{R}}\begin{bmatrix} -\mathbf{I} & \mathbf{0} & \left\lfloor {}^G\hat{\mathbf{T}}_{Bi}\times\right\rfloor & \mathbf{0} & \mathbf{0}\end{bmatrix}$$

where

$$\mathbf{A} = \frac{\partial h}{\partial {}^R\mathbf{p}_L^i} = \begin{bmatrix}\dfrac{\partial d}{\partial {}^R\mathbf{p}_L^i}\\ \\ \dfrac{\partial \beta}{\partial {}^R\mathbf{p}_L^i}\end{bmatrix} = \begin{bmatrix}\dfrac{{}^Re_1\cdot{}^R\hat{\mathbf{p}}_L^i}{\|{}^R\hat{\mathbf{p}}_L^i\|} & \dfrac{{}^Re_2\cdot{}^R\hat{\mathbf{p}}_L^i}{\|{}^R\hat{\mathbf{p}}_L^i\|} & 0\\ \\ \dfrac{-{}^Re_2\cdot{}^R\hat{\mathbf{p}}_L^i}{\|{}^R\hat{\mathbf{p}}_L^i\|^2} & \dfrac{{}^Re_1\cdot{}^R\hat{\mathbf{p}}_L^i}{\|{}^R\hat{\mathbf{p}}_L^i\|^2} & 0\end{bmatrix}.$$

A.2 Pole feature

For pole features, the first step to derive the measurement model is to solve the intersection point of the line and the Radar FOV plane.

A plane is described as $({}^G\boldsymbol{\pi}, {}^G d)$ in {G}, which represents a unit normal vector and the shortest distance to the origin of {G}.

All points ${}^G\mathbf{x}$ on the plane forms the set:

$$\{{}^G\mathbf{x} \in \Re^3 | {}^G\boldsymbol{\pi}\cdot{}^G\mathbf{x} = {}^G d\}.$$

If described in {R}, the set is:

$$\{{}^R\mathbf{x} \in \Re^3 | {}^R\boldsymbol{\pi}\cdot{}^R\mathbf{x} = {}^R d\}.$$

A line in the 3D space is described as $({}^{G}\mathbf{p}_L^i, {}^{G}\mathbf{v}_L^i)$, which is a point on the line and a unit vector along the line representing the direction. So any point ${}^{G}\mathbf{p}_d$ on the line could be expressed as:

$$ {}^{G}\mathbf{p}_d = {}^{G}\mathbf{p}_L^i + s{}^{G}\mathbf{v}_L^i, $$

where scalar *s* is the distance from ${}^{G}\mathbf{p}_L^i$ to ${}^{G}\mathbf{p}_d$.

In our situation, the parameters of the Radar plane within {R} are

$$ {}^{R}\boldsymbol{\pi} = [\ 0\ 0\ 1\ ]^T, {}^{R}d = 0 $$

In {R}, the vector from radar origin to the intersection should be on the plane and also on the line, so the intersection ${}^{R}\mathbf{p}_d$ is subject to two constraints:

$$ {}^{R}\mathbf{p}_d = {}^{R}\mathbf{p}_L^i + s\ {}^{R}\mathbf{v}_L^i $$

$$ {}^{R}\boldsymbol{\pi} \cdot {}^{R}\mathbf{p}_d = 0. $$

By substituting ${}^{R}\mathbf{p}_d$ into the second equation, we can solve for *s*, and by putting *s* back to the first equation, ${}^{R}\mathbf{p}_d$ is:

$$ {}^{R}\mathbf{p}_d = {}^{R}\mathbf{p}_L^i - {}^{R}\mathbf{v}_L^i \frac{{}^{R}\boldsymbol{\pi} \cdot {}^{R}\mathbf{p}_L^i}{{}^{R}\boldsymbol{\pi} \cdot {}^{R}\mathbf{v}_L^i}. $$

To convert $({}^{G}\mathbf{p}_L^i, {}^{G}\mathbf{v}_L^i)$ from {G} to {R}, we need the following equations:

$$ \begin{aligned} {}^{R}\mathbf{p}_L^i &= {}^{R}_{B}\mathbf{R}\,{}^{B}_{G}\mathbf{R}({}^{G}\mathbf{p}_L^i - {}^{G}\mathbf{p}_B) - {}^{R}_{B}\mathbf{R}\,{}^{B}\mathbf{T}_{BR} \\ {}^{R}\mathbf{v}_L^i &= {}^{R}_{B}\mathbf{R}\,{}^{B}_{G}\mathbf{R}\,{}^{G}\mathbf{v}_L^i \end{aligned}. $$

Then if we have an estimate of the vehicle states, extrinsic calibration parameters of the Radar sensor, and the landmark (line feature) parameters described in global frame, we can estimate the position of intersection as:

$$ {}^{R}\hat{\mathbf{p}}_d = {}^{R}\hat{\mathbf{p}}_L^i - {}^{R}\hat{\mathbf{v}}_L^i \frac{{}^{R}\boldsymbol{\pi} \cdot {}^{R}\hat{\mathbf{p}}_L^i}{{}^{R}\boldsymbol{\pi} \cdot {}^{R}\hat{\mathbf{v}}_L^i}, $$

where the line parameters are estimated as:

$$\begin{aligned} {}^{R}\hat{\mathbf{p}}_L^i &= {}_B^R\mathbf{R}\,{}_G^B\hat{\mathbf{R}}({}^{G}\mathbf{p}_L^i - {}^{G}\hat{\mathbf{p}}_B) - {}_B^R\mathbf{R}\,{}^{B}\mathbf{T}_{BR} \\ {}^{R}\hat{\mathbf{v}}_L^i &= {}_B^R\mathbf{R}\,{}_G^B\hat{\mathbf{R}}\,{}^{G}\mathbf{v}_L^i \end{aligned}.$$

The linearization can be described as a series of partial derivatives

$$\mathbf{H} = \frac{\partial \mathbf{z}}{\partial {}^{R}\mathbf{p}_d}\,\frac{\partial {}^{R}\mathbf{p}_d}{\partial {}^{R}\mathbf{L}_L^i}\,\frac{\partial {}^{R}\mathbf{L}_L^i}{\partial {}^{G}\mathbf{x}_B},$$

where vector ${}^{R}\mathbf{L}_L^i = [{}^{R}\mathbf{p}_L^{i\,T} \quad {}^{R}\mathbf{v}_L^{i\,T}]^T$ represents the straight line parameters.

The relationship between the raw measurement vector **z** and the intersection point ${}^{R}\mathbf{p}_d$ is the same as that in the point feature model, so the first partial derivative has the same format

$$\mathbf{F}_{2\times 3} = \frac{\partial h}{\partial {}^{R}\mathbf{p}_d} = \begin{bmatrix} \dfrac{\partial d}{\partial {}^{R}\mathbf{p}_d} \\ \dfrac{\partial \beta}{\partial {}^{R}\mathbf{p}_d} \end{bmatrix} = \begin{bmatrix} \dfrac{{}^{R}e_1 \cdot {}^{R}\hat{\mathbf{p}}_d}{\|{}^{R}\hat{\mathbf{p}}_d\|} & \dfrac{{}^{R}e_2 \cdot {}^{R}\hat{\mathbf{p}}_d}{\|{}^{R}\hat{\mathbf{p}}_d\|} & 0 \\ \dfrac{-{}^{R}e_2 \cdot {}^{R}\hat{\mathbf{p}}_d}{\|{}^{R}\hat{\mathbf{p}}_d\|^2} & \dfrac{{}^{R}e_1 \cdot {}^{R}\hat{\mathbf{p}}_d}{\|{}^{R}\hat{\mathbf{p}}_d\|^2} & 0 \end{bmatrix}.$$

The second partial derivative in the **H** matrix is

$$\mathbf{D}_{3\times 6} = \begin{bmatrix} \dfrac{\partial {}^{R}\mathbf{p}_d}{\partial {}^{R}\mathbf{p}_L^i} & \dfrac{\partial {}^{R}\mathbf{p}_d}{\partial {}^{R}\mathbf{v}_L^i} \end{bmatrix}.$$

where

$$\frac{\partial {}^{R}\mathbf{p}_d}{\partial {}^{R}\mathbf{p}_L^i} = \mathbf{I} - \frac{{}^{R}\hat{\mathbf{v}}_L^i\,{}^{R}\boldsymbol{\pi}^T}{{}^{R}\boldsymbol{\pi} \cdot {}^{R}\hat{\mathbf{v}}_L^i},$$

$$\begin{aligned} \frac{\partial {}^{R}\mathbf{p}_d}{\partial {}^{R}\mathbf{v}_L^i} &= -\frac{{}^{R}\boldsymbol{\pi} \cdot {}^{R}\hat{\mathbf{p}}_L^i}{{}^{R}\boldsymbol{\pi} \cdot {}^{R}\hat{\mathbf{v}}_L^i}\mathbf{I} + {}^{R}\hat{\mathbf{v}}_L^i\,{}^{R}\boldsymbol{\pi}^T\frac{{}^{R}\boldsymbol{\pi} \cdot {}^{R}\hat{\mathbf{p}}_L^i}{({}^{R}\boldsymbol{\pi} \cdot {}^{R}\hat{\mathbf{v}}_L^i)^2} \\ &= \frac{{}^{R}\boldsymbol{\pi} \cdot {}^{R}\hat{\mathbf{p}}_L^i}{{}^{R}\boldsymbol{\pi} \cdot {}^{R}\hat{\mathbf{v}}_L^i}\left(-\mathbf{I} + \frac{{}^{R}\hat{\mathbf{v}}_L^i\,{}^{R}\boldsymbol{\pi}^T}{{}^{R}\boldsymbol{\pi} \cdot {}^{R}\hat{\mathbf{v}}_L^i}\right) \end{aligned}.$$

The common terms can be extracted out of the square brackets, resulting in

$$\mathbf{D}_{3\times 6} = \begin{bmatrix} \dfrac{\partial^R \mathbf{p}_d}{\partial^R \mathbf{p}_L^i} & \dfrac{\partial^R \mathbf{p}_d}{\partial^R \mathbf{v}_L^i} \end{bmatrix}$$
$$= \left(\mathbf{I} - \frac{{}^R\hat{\mathbf{v}}_L^i \, {}^R\boldsymbol{\pi}^T}{{}^R\boldsymbol{\pi} \cdot {}^R\hat{\mathbf{v}}_L^i} \right) \begin{bmatrix} \mathbf{I} & -\mathbf{I}\dfrac{{}^R\boldsymbol{\pi} \cdot {}^R\hat{\mathbf{p}}_L^i}{{}^R\boldsymbol{\pi} \cdot {}^R\hat{\mathbf{v}}_L^i} \end{bmatrix}$$

The third partial derivative of the **H** matrix is

$$\mathbf{C}_{6\times 15} = \begin{bmatrix} \dfrac{\partial^R \mathbf{p}_L^i}{\partial^G \mathbf{x}_B} \\ \\ \dfrac{\partial^R \mathbf{v}_L^i}{\partial^G \mathbf{x}_B} \end{bmatrix},$$

where $\dfrac{\partial^R \mathbf{p}_L^i}{\partial^G \mathbf{x}_B}$ could be calculated using the same equation as that in the point feature model.

$$\frac{\partial^R \mathbf{p}_L^i}{\partial^G \mathbf{x}_B} = {}_B^R\mathbf{R} \, {}_G^B\hat{\mathbf{R}} \begin{bmatrix} -\mathbf{I} & \mathbf{0} & \left\lfloor {}^G\hat{\mathbf{T}}_{Bi} \times \right\rfloor & \mathbf{0} & \mathbf{0} \end{bmatrix}.$$

The derivation of $\dfrac{\partial^R \mathbf{v}_L^i}{\partial^G \mathbf{x}_B}$ is

$$\begin{aligned} {}^R\mathbf{v}_L^i &= {}_B^R\mathbf{R} \, {}_G^B\mathbf{R} \, {}^G\mathbf{v}_L^i \\ &= {}_B^R\mathbf{R} \, {}_G^B\hat{\mathbf{R}} \left(\mathbf{I} - \lfloor \boldsymbol{\rho} \times \rfloor \right) {}^G\mathbf{v}_L^i \\ &= {}_B^R\mathbf{R} \, {}_G^B\hat{\mathbf{R}} \, {}^G\mathbf{v}_L^i - {}_B^R\mathbf{R} \, {}_G^B\hat{\mathbf{R}} \lfloor \boldsymbol{\rho} \times \rfloor \, {}^G\mathbf{v}_L^i \\ &= {}^R\hat{\mathbf{v}}_L^i + {}_B^R\mathbf{R} \, {}_G^B\hat{\mathbf{R}} \left\lfloor {}^G\mathbf{v}_L^i \times \right\rfloor \boldsymbol{\rho} \end{aligned}$$

By moving ${}^R\hat{\mathbf{v}}_L^i$ to the left of the equality sign, the equation becomes

$$\begin{aligned} \delta {}^R\mathbf{v}_L^i &= {}_B^R\mathbf{R} \, {}_G^B\hat{\mathbf{R}} \left\lfloor {}^G\mathbf{v}_L^i \times \right\rfloor \boldsymbol{\rho} \\ &= {}_B^R\mathbf{R} \, {}_G^B\hat{\mathbf{R}} \begin{bmatrix} -\mathbf{I} & \mathbf{0} & \left\lfloor {}^G\mathbf{v}_L^i \times \right\rfloor & \mathbf{0} & \mathbf{0} \end{bmatrix} \begin{bmatrix} \delta\mathbf{p} \\ \delta\mathbf{v} \\ \boldsymbol{\rho} \\ \delta\mathbf{b}_a \\ \delta\mathbf{b}_g \end{bmatrix} \end{aligned}$$

By combining the equations above, we can reach the final form of $\mathbf{C}_{6\times 15}$ as

$$\mathbf{C}_{6\times 15} = \begin{bmatrix} \dfrac{\partial^R \mathbf{p}_L^i}{\partial^G \mathbf{x}_B} \\ \\ \dfrac{\partial^R \mathbf{v}_L^i}{\partial^G \mathbf{x}_B} \end{bmatrix} = \begin{bmatrix} {}^R_B\mathbf{R}\ {}^B_G\hat{\mathbf{R}} & \mathbf{0} \\ \mathbf{0} & {}^R_B\mathbf{R}\ {}^B_G\hat{\mathbf{R}} \end{bmatrix} \begin{bmatrix} -\mathbf{I} & \mathbf{0} & \lfloor {}^G\hat{\mathbf{T}}_{Bi}\times \rfloor & \mathbf{0} & \mathbf{0} \\ \mathbf{0} & \mathbf{0} & \lfloor {}^G\mathbf{v}_L^i\times \rfloor & \mathbf{0} & \mathbf{0} \end{bmatrix}.$$

So finally, the linearized measurement matrix is

$$\mathbf{H} = \mathbf{F}_{2\times 3}\mathbf{D}_{3\times 6}\mathbf{C}_{6\times 15}$$